

**MASARYKOVA UNIVERZITA**  
**PŘÍRODOVĚDECKÁ FAKULTA**  
ÚSTAV TEORETICKÉ FYZIKY A ASTROFYZIKY

# **Diplomová práce**

**BRNO 2025**

**BC. EMA ŠÍPKOVÁ**



**MASARYKOVA  
UNIVERZITA**  
PŘÍRODOVĚDECKÁ FAKULTA  
ÚSTAV TEORETICKÉ FYZIKY A ASTROFYZIKY

---

# **Sinusoidal variables among F to O spectral type stars**

Diplomová práce

**Bc. Ema Šipková**

Vedoucí práce: Mgr. Marek Skarka, Ph.D.      Brno 2025



# Bibliografický záznam

**Autor:** Bc. Ema Šipková  
Přírodovědecká fakulta, Masarykova univerzita  
Ústav teoretické fyziky a astrofyziky

**Název práce:** Sinusoidální proměnné mezi hvězdami spektrálních typů F až O

**Studijní program:** PrF N-FY ASTRO

**Studijní obor:** PrF ASTRO Astrofyzika

**Vedoucí práce:** Mgr. Marek Skarka, Ph.D.

**Akademický rok:** 2024/2025

**Počet stran:** xvi + 88

**Klíčová slova:** Proměnné hvězdy, dvojhvězdy, pulzující hvězdy, rotující hvězdy, TESS, fotometrie, spektroskopie



# Bibliographic entry

**Author:** Bc. Ema Šípková  
Faculty of Science, Masaryk University  
Department of theoretical physics and astrophysics

**Title of Thesis:** Sinusoidal variables among F to O spectral type stars

**Degree Programme:** PrF N-FY ASTRO

**Field of Study:** PrF ASTRO Astrophysics

**Supervisor:** Mgr. Marek Skarka, Ph.D.

**Academic Year:** 2024/2025

**Number of Pages:** xvi + 88

**Keywords:** Variable stars, binary stars, pulsating stars, rotating stars, TESS, photometry, spectroscopy



# Abstrakt

Značná část hvězd horní části hlavní posloupnosti – spektrálních typů O, B, A a F – vykazuje periodické změny jasnosti. Tyto změny lze vysvětlit různými mechanismy, například dvojhvězdností, pulzacemi nebo nehomogenitami na povrchu hvězdy či v jejím okolí. Cílem této práce bylo identifikovat hvězdy vykazující jednoduchou sinusoidální fotometrickou proměnnost a určit povahu jejich změn pomocí fotometrických dat z družice *TESS*, spektroskopických pozorování z ešeletových spektrografů a údajů z databází. Zvláštní pozornost byla věnována identifikaci kandidátů vykazujících skvrny v radiativních atmosférách.

Z počátečního vzorku více než 45 000 objektů z *TESS* Input Catalogue bylo vybráno 34 cílů, které se podařilo napozorovat spektroskopicky a které byly analyzovány. Kombinace fotometrických a spektroskopických dat umožnila spolehlivou klasifikaci sledovaných objektů. Z celkového počtu 34 hvězd bylo 50.0 % identifikováno jako dvojhvězdy, 2.9 % jako pulzující hvězdy, 26.5 % jako kandidáti na hvězdy se skvrnami a u 20.6 % zůstala klasifikace nejasná kvůli nejednoznačnosti dat. Analýza vedla k objevu 7 nových dvojhvězd, 1 pulzující hvězdy a 9 kandidátů na hvězdy se skvrnami. Tato práce zdůrazňuje význam individuálního přístupu při určování příčin variability, zejména v případech, kdy samotná fotometrická data nejsou dostatečná k určení mechanismu změn.

# Abstract

A significant fraction of upper main-sequence stars - those of spectral types O, B, A, and F - show periodic brightness variations. These changes can be explained by different mechanisms, including binarity, pulsations or inhomogeneities on the stellar surface or the object's surroundings. The aim of this work was to identify stars with simple sinusoidal flux variations and determine the nature of their variability using photometric data from *TESS*, spectroscopic observations from echelle spectrographs and data from the databases. Special attention was given to identifying candidates exhibiting surface spots in radiative atmospheres.

From the initial sample of over 45 000 objects in the *TESS* Input Catalogue, 34 targets from both hemispheres were selected for follow-up analysis. The combined photometric and spectroscopic datasets enabled robust classification of the targets. Among the 34 objects, 50.0 % were identified as binary systems, 2.9 % as pulsators, 26.5 % as candidates for spotted stars and 20.6 % remained unclassified due to the ambiguity of the data. The analysis led to the discovery of 7 new binary systems, 1 pulsating star and 9 potential spotted stars. This work underscores the importance of an individual approach to variability identification, particularly in cases where photometric data alone are insufficient to determine the underlying mechanisms.



ZADÁNÍ  
DIPLOMOVÉ PRÁCE

Akademický rok: 2024/2025

---

**Ústav:** Ústav teoretické fyziky a astrofyziky

---

**Studentka:** Bc. Ema Šipková

---

**Program:** Fyzika

---

**Specializace:** Astrofyzika

Ředitel ústavu PřF MU Vám ve smyslu Studijního a zkušebního řádu MU určuje diplomovou práci s názvem:

---

**Název práce:** Sinusoidální proměnné mezi hvězdami spektrálních typů F až O

---

**Název práce anglicky:** Sinusoidal variables among F to O spectral type stars

---

**Jazyk práce:** angličtina**Oficiální zadání:**

Značná část hvězd horní části hlavní posloupnosti vykazuje periodickou fotometrickou proměnnost, která je obvykle spojována s rotací a nehomogenitami na povrchu či v okolí hvězd. Stejně změny jasnosti mohou být způsobeny i dvojhvězdností nebo pulzacemi. Speciálním případem jsou potom hvězdy vykazující jednoduchou sinusoidální fotometrickou proměnnost. Cílem práce bude identifikovat takovéto objekty v datech z družice TESS a odhadnout podstatu jejich proměnnosti s pomocí vlastních spektroskopických měření a údajů v databázích.

---

**Vedoucí práce:** Mgr. Marek Skarka, Ph.D.

---

**Konzultant:** prof. RNDr. Zdeněk Mikulášek, CSc.

---

**Datum zadání práce:** 22. 11. 2023

---

**V Brně dne:** 3. 5. 2025

Zadání bylo schváleno prostřednictvím IS MU.

Bc. Ema Šipková, 11. 11. 2024

Mgr. Marek Skarka, Ph.D., 11. 11. 2024

Mgr. Dušan Hemzal, Ph.D., 27. 11. 2024



# Poděkování

Podobně jako správná detektivní práce, psaní této diplomové práce bylo cestou plnou vyšetřování, analyzování stop a odhalování tajemství ukrytých v hvězdných datech. Během tohoto procesu jsem měla to štěstí, že jsem měla kolem sebe brilantní mysl, které byly mými společníky na této intelektuální detektivní misi.

Nejprve bych ráda vyjádřila své nejhlubší poděkování svému vedoucímu Mgr. Marekovi Skarkovi, PhD. Jeho vedení, pochopení a trpělivost byly během tohoto procesu neocenitelné. Byl Watson pro mého Holmese, vždy po mém boku, aby položil ty správné otázky a pomohl mi poskládat záhadu této hvězdné klasifikace. Bez jeho odbornosti a podpory by závěry, které jsem vyvodila, zůstaly nepolapitelné, podobně jako nevyřešený případ.

Všem, kteří se na tomto výzkumu přímo či nepřímo podíleli, patří můj upřímný dík. Prof. RNDr. Zdeněk Mikulášek, CSc. byl vynikajícím konzultantem, který pomáhal sestavit metodologii detrendování a zabezpečil, že falešné stopy ve světelných křivkách nebudou bránit redukci dat. Proces redukce spekter by nebyl možný bez odborných znalostí a pomoci lektorů a mých kolegů během workshopu Observational Techniques a kurzu Echelletové spektroskopie a měření radiálních rychlostí v Ondřejově, kde jsme strávili dlouhé noci analyzováním spekter, jež jsou otisky prstů hvězd, každé jedinečné. Za poskytnutí spekter bych chtěla hlavně poděkovat pozorovatelům ze Stelárního oddělení AsÚ., hlavně Pavolu Gajdošovi za redukci těchto spekter a dále také pozorovatelům na MUSIKOS, jmenovitě Martinu Vaňkovi, který tato pozorování umožnil. Nakonec taky můj tichý asistent ChatGPT zajistil, aby se tato práce četla stejně jasně a souvisle jako ten nejlepší detektivní román, a pomohl mi se stylizací textu a gramatikou.

V neposlední řadě patří mé poděkování mé rodině a přátelům, kteří byli svědky mých občasných zoufalých výlevů a chvíl frustrace. Děkuji, že jste mě trpělivě podporovali a pomohli mi udržet se soustředěnou na případ.

Diplomová práce vznikla za podpory projektu MŠMT Inter transfer LTT20015 a projektu MPP SAV-25-10. Práce částečně vznikla na základě dat z Perkova dalekohledu na Astronomickém ústavu AVČR v Ondřejově.

# Prohlášení

Prohlašuji, že jsem svoji diplomovou práci vypracovala samostatně pod vedením vedoucího práce s využitím informačních zdrojů, které jsou v práci citovány.

Brno 5. května 2025

.....  
Bc. Ema Šipková



*When you have eliminated the impossible,  
whatever remains, however improbable,  
must be the truth.*

— Arthur Conan Doyle (1890)

*There is nothing more deceptive than an  
obvious fact.*

— Arthur Conan Doyle (1892)



# Contents

<b>Introduction</b> .....	<b>1</b>
<b>1. Stellar variability</b> .....	<b>3</b>
1.1 Pulsating variables .....	5
1.2 Rotating variables .....	10
1.3 Eclipsing binaries .....	11
<b>2. Uncovering sinusoidal variability from photometry</b> .....	<b>13</b>
2.1 Data sources and initial sample .....	13
2.2 Variability identification .....	17
2.3 Finalization of sample .....	19
2.4 Other objects .....	24
<b>3. Spectroscopic observations of selected targets</b> .....	<b>27</b>
3.1 Data sources and target selection .....	27
3.2 Data reduction .....	28
3.3 Radial velocity analysis .....	32
<b>4. Classification of stars</b> .....	<b>35</b>
4.1 Binary stars .....	42
4.2 Pulsating variables .....	45
4.3 Uncertain objects .....	46
4.4 Candidates for spotted stars .....	50
<b>Conclusion</b> .....	<b>53</b>
<b>Bibliography</b> .....	<b>55</b>
<b>Appendix</b> .....	<b>63</b>



# Introduction

Variable stars are classified based on their light curve morphology and other observational characteristics to distinguish different variability mechanisms. However, determining the exact cause of these variations can be complex, as some stars exhibit features of multiple categories. A significant number of upper main sequence stars show photometric variability, often attributed to rotational modulation, pulsations, or interactions within binary systems. Understanding the origin of these variations is crucial for constraining stellar structure, rotation, and evolutionary processes.

Upper main sequence stars, including O, B, A, and early F-type stars, are particularly significant in astrophysics. As massive, luminous objects, they influence their surroundings through strong stellar winds, ionizing radiation, and eventual supernova explosions, which enrich the interstellar medium with heavy elements. Their short lifespans and rapid evolution make them valuable tracers of star formation history and galactic structure. Studying their variability provides insight into internal processes such as convection, differential rotation, and magnetic fields, which are fundamental to understanding stellar physics.

This study focuses on upper main sequence stars that exhibit simple sinusoidal photometric variability. The advent of high-precision space-based photometry, particularly from the Transiting Exoplanet Survey Satellite (*TESS*) (Ricker et al. 2015), has enabled a systematic investigation of such stars. However, photometric data alone are often insufficient to determine the underlying mechanism of variability, making spectroscopic observations essential. To address this, *TESS* light curves were complemented by spectroscopic data obtained from the Ondřejov Echelle Spectrograph (OES) at the Astronomical Institute of the Czech Academy of Sciences, MUSIKOS spectrograph at Skalnaté Pleso, Slovakia and the PUCHEROS+ Spectrograph in La Silla, Chile. By combining these datasets, this work aims to clarify the nature of sinusoidal variability in upper main sequence stars and contribute to a broader understanding of their physical properties.

Chapter 1 provides an overview of the various types of variable stars, with a focus on those exhibiting sinusoidal photometric variability. It explores the mechanisms behind pulsations, binary systems, and the influence of surface inhomogeneities in stellar atmospheres. In Chapter 2, the photometric data sources are introduced and the methodology used to compile a final sample of stars is discussed, based on the sinusoidal nature of their light curves. Chapter 3 details the spectroscopic data sources and outlines the procedures for processing and collecting the necessary data. The classification of the studied stars, along with the interpretation of the results, is presented in Chapter 4. Finally, the results are compared with previous studies and parameters from existing databases, emphasizing the importance of a comprehensive analysis and addressing the challenges in the investigation of stellar variability.



# Chapter 1

## Stellar variability

Variations in the flux of an observed object over time, also known as photometric variations, can be attributed to different astrophysical processes. This variability can be random, non-periodic, such as sudden brightening due to flares, mass ejections, or explosive outbursts, or it can exhibit periodic or semiperiodic patterns. Periodic variations are associated with pulsations, rotation, eclipses or other conditions or processes (Fetherolf et al. 2023). Detailed analysis of these events provides important information about the object’s dynamics, internal structure, composition and fundamental properties, including mass, radius and age (Kurtz 2022).

There have been many attempts to group objects with similar properties and create distinct classes of variable sources (see, for example, the classification scheme in the General Catalogue of Variable Stars (GCVS) (Samus’ et al. 2017), which has been evolving since 1946). This division is very useful, but it has its limitations. The transition between classes can be continuous, making it challenging to assign an object to a specific class, especially when the objects’ properties overlap with those of adjacent categories (Eyer & Mowlavi 2008). Furthermore, observed photometric properties of different classes may overlap, making it hard to identify the source of variations without additional information, such as spectroscopic follow-up or observations in different wavebands (Skarka et al. 2022).

The classification used in this work is based on the classification diagram proposed by Gaia Collaboration et al. (2019) shown in Figure 1.1 and has been widely used in the analysis of large-scale surveys (see, for example, Gaia DR2 (Gaia Collaboration et al. 2019), WISE (Petrosky et al. 2021)).

This classification groups variable sources according to the source of their variation. The tree establishes four levels of division, starting with the classical distinction between extrinsic and intrinsic variables. Extrinsic variables are associated with photometric variability caused by external factors or interactions, such as the relative position of the object to the observer’s line of sight or rotation, while the object itself causes intrinsic variability due to internal processes or structural changes. The second level groups object into categories according to their type, such as an asteroid, star, or active galactic nucleus (AGN), which are further classified according to the mechanism at the origin of their variability. The last level gathers the variables based on the similarities in their observed photometric properties, such as periodicity, amplitude, timescale and the shape of their light curve (Eyer & Mowlavi 2008).

The variability tree describes classes of variable stars according to their photometric behaviour. The appearance of spectra can also characterize stars based on the surface temperature and the presence of specific absorption lines. Table 1.1 provides an overview of spectral classes with their associated temperature ranges and spectral features typical for each class. In the table, neutral chemical elements are denoted following the convention with “I” following the element symbol.



the classes. Cold stars exhibit a variety of dynamic phenomena, such as the presence of active regions, chromospheres and coronae, as well as surface features, including starspots, flares and prominences. Their rotation is generally slower. Large convective zones under the photospheric layer of the atmosphere transport energy from the core, setting the star's outer layers in motion and generating strong local magnetic fields. Over time, these magnetic fields break and give rise to the diverse manifestations of stellar activity observed on cold stars. In contrast, hot stars exhibit stable atmospheres characterized by the absence of dynamic activity, relatively stable global magnetic fields and faster rotation than their colder counterparts. Energy transport is realized by radiative diffusion, where energy is carried by photons rather than convective motion. The slow processes of radiative diffusion lead to chemical peculiarities in the atmospheres of these stars (see Section 1.1, subsection about CP stars) and radiation-driven stellar winds (Mikulášek 2021).

Looking at the different behaviour of cold and hot stars, the dividing line between them can be defined as the transition between convective and radiative envelopes, which causes the dominance of various dynamic processes. According to Anders & Pedersen (2023) and Brun & Miesch (2008), this boundary can be found in stars of spectral type A and F, where convection becomes inefficient, and radiation in the envelope starts to dominate. This transition is closely related to the Kraft break, a sharp drop in stellar rotation rates observed around spectral type F5. Stars with convective envelopes (cooler than the Kraft break) experience strong magnetic braking due to stellar winds, leading to significant rotational deceleration over time. In contrast, hotter stars with radiative envelopes lack this mechanism, allowing them to maintain much higher rotational velocities. The Kraft break, therefore, serves as an important marker of the shift in angular momentum loss processes across the hot-cold star boundary (Kraft 1967). Mikulášek (2021) states that the dividing spectral class between hot and cold stars is F2, corresponding to an effective temperature of 7000 K; however, no strictly defined boundary exists between hot and cold stars in the literature. The general consensus places the dividing line around the early F-type stars.

Figure 1.2 shows various classes of pulsating stars across the Hertzsprung-Russell (HR) diagram based on the *Gaia* data (Gaia Collaboration et al. 2019). Colour index  $BP - RP$  indirectly indicates the effective temperature of the studied objects. The approximate lower temperature limit for F-type stars (6000 K) roughly equals  $BP - RP \sim 0.5$  (Andrae 2021) and serves as the approximate boundary between hot and cold stars.

The HR diagrams in Figure 1.2 show that hot stars include many classes, be they pulsating stars, rotating variables or binaries. The main classes of pulsating stars will be further discussed in Section 1.1, including  $\delta$ -Scuti (DSCT),  $\beta$  Cephei (BCEP),  $\gamma$  Doradus (GDOR), rapidly oscillating Ap stars (roAp) and slowly pulsating B stars (SPB). In Section 1.2, different classes of rotationally variable stars will be discussed with emphasis on chemically peculiar (CP) stars and in Section 1.3, eclipsing binaries will be characterized, especially contact systems.

## 1.1 Pulsating variables

Pulsating stars are a class of variable stars with brightness variations caused by changes in the area and effective temperature of the observed stellar surface. The observations show that stellar pulsations are stable phenomena resulting from complex interactions between a star's internal structure and outer layers. Stars are gravitationally bound objects in stable hydrostatic equilibrium, where gravitational and pressure forces balance each other out. Any deviation from the equilibrium state amplifies the restoring force component, which returns the system to its equilibrium position. However, upon reaching equilibrium, the star does not cease its motion but continues to oscillate in the opposite direction due to inertia, thereby resulting in oscillatory behaviour (Mikulášek & Zejda 2013).

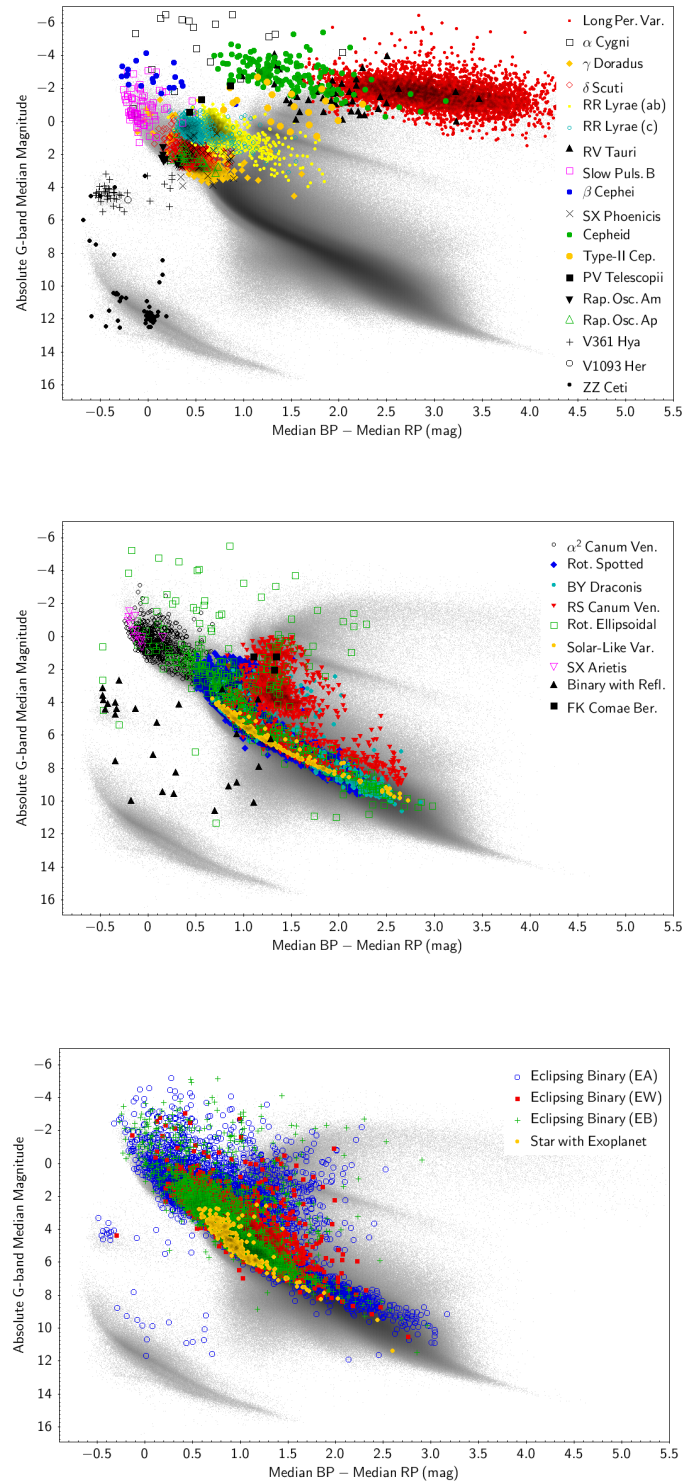


Figure 1.2: Position of different classes of pulsating stars (top), rotationally variable stars (middle), and eclipsing binaries (bottom) on observational HR diagram taken from [Gaia Collaboration et al. \(2019\)](#).

The pulsation of stars is mainly caused by the propagation of sound waves through stellar interiors. Because sound waves are pressure waves, their speed is given by the equation of state and depends on the density and temperature of the material through which they propagate. Speed of sound  $v_s$  in the adiabatic case (equation of state  $p = \text{const} \cdot \rho^\Gamma$ ) can be derived using the following equations:

$$v_s = \sqrt{\frac{\partial p}{\partial \rho}} = \sqrt{\Gamma \frac{p}{\rho}}, \quad (1.1)$$

where  $p$  is the pressure,  $\rho$  is material density and  $\Gamma$  is the adiabatic exponent. In the case of an ideal gas, the equation of state becomes  $p\mu = \rho kT$ , where  $\mu$  is the mean molecular weight, and the speed of sound satisfies the equation:

$$v_s = \sqrt{\Gamma \frac{kT}{\mu}} \quad (1.2)$$

Measuring the speed of sound in gas provides information about the temperature and chemical composition of stellar interiors and, in combination with the equation of state, can, in turn, reveal something about the pressure and density of the material.

These acoustic waves are called “pressure” modes, or p-modes, where the pressure gradient is the main restoring force for perturbed objects. Gas motions inside a star are mainly radial, and the sound waves probe the outer layers and the conditions within. When the restoring force is buoyancy instead of pressure, the excited pulsations are called “gravity” modes, or g-modes. Motions of gas are primarily horizontal, and they behave as internal gravity waves probing the interiors of stars (Kurtz 2006). The transition between p-modes and g-modes is sometimes called f-modes, representing surface gravity waves (Christensen-Dalsgaard 2002).

Because the stars are three-dimensional objects, their oscillation can be described using modes in three orthogonal directions: concentric radial shells (radial modes), lines of latitude and longitude (non-radial modes). The equations of motion in the spherically symmetric star have solutions similar to the quantum harmonic oscillator (see, for example, Kurtz (2006), or Christensen-Dalsgaard (2002)). Therefore, the star’s modes can be described by three quantum numbers:  $n$ , called an overtone, represents the number of radial nodes;  $l$ , called the degree of mode, describes the number of surface nodes; and  $m$ , called the azimuthal order, describes how many of the surface nodes are aligned along the lines of longitude. Nodes are places where the stellar matter remains motionless, whereas an antinode is a place with the largest displacement amplitude (Kurtz 2006).

Radial modes are oscillation modes with  $l, m = 0$ , only described by an overtone. The simplest radial mode  $n = 0$  describes a star expanding and contracting with the node in the centre and antinode on the surface. The first overtone ( $n = 1$ ) has one radial node inside the star. The material enclosed in the node moves in antiphase to the material above it. Additional overtones add more radial nodes inside the star (Mikulášek & Zejda 2013).

Non-radial modes are oscillation modes with  $l, m \neq 0$  that occur only for  $n \geq 1$  for a compressible object. The simplest non-radial dipole mode  $l = 1, m = 0$  has an equator of the star as a node with material above and below it contracting and expanding in antiphase. For the observer, the star has an apparent up-and-down motion, but Christensen-Dalsgaard (1976) showed the centre of the mass remains fixed. A higher number of dipole modes adds  $l - |m|$  lines of latitude. Waves travelling across the stellar surface are described by the  $m$ -modes and are caused by the Coriolis force induced by the object’s rotation. The rotating body displaces up-and-down pulsations into circular pulsations travelling in the direction of rotation (prograde motion,  $m$  is negative) or against the direction of rotation (retrograde motion, positive  $m$ ). The number of dipole modes restricts possible values of  $m$ ;  $m \in (-l, l)$  (Kurtz 2006).

As a star pulsates, it undergoes cycles of expansion and contraction that lose energy with each pulsation cycle, meaning that most of the star's volume damps its oscillations. For them to be stable, there must be a region in the star where energy is retained and actively fed into the oscillations. Stellar pulsations must be supported by a supply of energy generated by various driving mechanisms. There are four known mechanisms:  $\kappa$ -mechanism, stochastic mechanism,  $\gamma$ -mechanism and  $\varepsilon$ -mechanism.

The driving mechanism supported by opacity, known as the  $\kappa$ -mechanism, operates in stars with ionised hydrogen and helium layers at a suitable depth to generate pulsations. In these regions, the opacity of hydrogen and helium increases, trapping radiation and causing a rise in temperature and pressure that drives the star to expand. As the temperature rises further, the gas becomes more ionized and transparent to radiation, allowing heat to escape and the gas to cool. This cooling reduces the pressure support, causing the star to contract. During contraction, the recombined hydrogen and helium absorb radiation again, restarting the cycle and sustaining the pulsations. If the  $\kappa$ -mechanism is supported by heat supply from the adjacent partially ionised regions that have higher temperatures, thermal capacities  $c_V$  and  $c_P$  of the material increase and the layer absorbs more heat. This effect is referred to as the  $\gamma$ -mechanism due to a ratio  $\gamma = c_P/c_V$  (Mikulášek & Zejda 2013).

The stochastic mechanism transfers energy from resonances of the star's natural frequencies into global oscillations. This mechanism occurs for solar-like oscillators and red giants with enough acoustic energy in the convection zones. The last mechanism is the  $\varepsilon$ -mechanism caused by the variations in the energy generation inside the star (Kurtz 2006).

There are many classes of pulsating stars, which are distinguished by their periods, amplitudes and the shape of their light curves. Figure 1.3 shows classes of pulsating stars and their location on the HR diagram. The main sequence is denoted with a dashed line, and the so-called instability strip's blue and red edge is marked with lines of corresponding colours. These edges define the temperature boundaries, where the ionised layer is at an ideal depth to support pulsations. This work only considers O, B, A and F-type stars near the main sequence; therefore, only the pulsation classes associated with these types will be described.

### $\delta$ -Scuti

$\delta$ -Scuti (DSCT) stars are the main-sequence pulsators located at the intersection of the main sequence and the instability strip on the HR diagram. Their location is at the border between convective envelopes of cold stars and radiative envelopes of hot stars, making them good candidates for studying stellar evolution (Bowman 2017). Light curves are characterized by fast (ir)regular variations, beating, bumps and interference, while their frequency spectra contain two or more independent peaks above 5 c/d (Skarka et al. 2022).

### $\gamma$ Doradus

$\gamma$  Doradus (GDOR) is a homogenous group of slowly pulsating stars near the red edge of the instability strip. They pulsate in the g-modes characterized by groups of frequencies below 5 c/d. Positions of these frequencies are close to the harmonics of the single peak, but they are not harmonics. Their lightcurves show sharp (ir)regular variations, beating and interference (Skarka et al. 2022).

They can exist in a hybrid mode together with DSCT variables, creating so-called hybrid pulsators where there are observed many independent peaks above and below 5 c/d. This limit represents an accepted dividing value between DSCT and GDOR pulsators (Grigahcène et al. 2010).

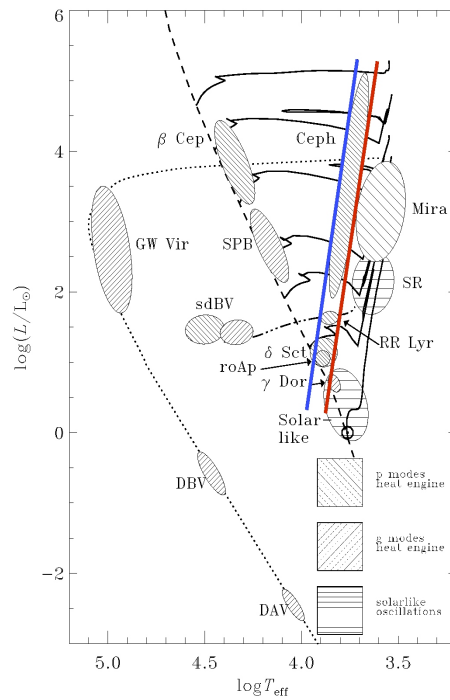


Figure 1.3: Pulsating stars across the HR diagram taken from Mikulášek & Zejda (2013). The red and blue lines represent the red and blue edges of the instability strip, respectively, and the markings inside individual types show the driving mechanism responsible for the pulsations.

### $\beta$ Cephei

$\beta$  Cephei variables (BCEP) belong to a narrow group of stars in the upper part of the main sequence between spectral classes B0 and B2. Lightcurve variations and radial velocity curves are shifted by a quarter of the period; the star is brightest when its temperature is the highest at a minimal radius during contraction (Aizenman & Lesh 1980). Frequencies of these variations are between 1.6 c/d and 10 c/d (Mikulášek & Zejda 2013). Pulsations are driven by the  $\kappa$  mechanism due to the photoionisation of the iron layer inside the star (Kurtz 2006).

### Slowly pulsating B stars

The group of slowly pulsating B stars (SPB) is defined by their small variation amplitudes (approximately 0.1 mag), which result from non-radial high-order g-modes. These stars span spectral types B2 to B9 and exhibit pulsation periods ranging from a few hours to several days.

### Rapidly oscillating Ap stars

Rapid oscillations of chemically peculiar A stars, also known as roAp stars, define a group of stars that cover the range of spectral types B8 - F2 on the main sequence of the HR diagram. These stars belong to a subtype of  $\alpha^2$  CVn (ACV) stars; more about them is in Section 1.2. The resulting light curve is an interplay between the rotation of these stars and the nonradial pulsations along their magnetic axis. Amplitudes of light variations are in the order of millimagnitudes with frequencies above 90 c/d (Kurtz 2022).

## 1.2 Rotating variables

Some rotating stars do not exhibit brightness variations because their photospheres are uniform and their radiation is isotropic. However, rotational variables represent a class of geometrically variable objects whose brightness changes due to deviations from the spherical symmetry of the stellar surface. These changes can occur for two main reasons: either the star's rotation causes irregularities, induced by spots or surface distortions, or the star's shape is deformed by the gravitational influence of a nearby companion. In the latter case, the companion does not transit the stellar disk as seen from the observer's point of view, but its gravitational pull still alters the star's geometry, leading to periodic brightness variations caused by different temperatures in different parts of the star, due to limb darkening.

Another way to achieve deformations of the star's shape is from the gravitational pull of its companion star. These systems, known as elliptical variables (ELL), are usually non-eclipsing close binary stars, where one or both components take on an ellipsoidal or teardrop shape. The observed brightness variations occur due to changes in the projected cross-section of the star as seen from Earth (Soszyński n.d.). Each orbital cycle produces two maxima and two minima in the light curve because the components usually rotate synchronously, thanks to tides (Phillips et al. 2024). However, the minima may differ in depth due to gravity darkening. Light curves of ellipsoidal variables with approximately circular orbits have symmetrical variations, while the eccentric ellipsoidal variables display significantly different shapes with highly asymmetric light curves (for example, see Wrona et al. (2022) about heartbeat stars) (Soszyński n.d.).

Stars are generally not perfectly spherical and can become deformed due to rapid rotation. This rotation causes the equatorial regions of the star to bulge outward while the poles are compressed. As a result, the poles experience an increase in temperature. The observer would only detect variations due to the deformed shape of the star if the rotational axis underwent precession (Mikulášek & Zejda 2013).

Photometric starspots of cold stars are created by local magnetic fields that suppress convective motion and block the flow of hot material from the star's centre. These fields create regions with lower temperatures, which can be observed as dark spots against the surrounding photosphere. These photometric spots serve as tracers of stellar rotation and reflect the dynamo process's characteristics that create the magnetic field of these objects (Strassmeier 2009). The longevity of these objects depends on the stellar type and the size of the spot.

Stable photometric spots form on stars with slow rotation and a stable magnetic field - a feature commonly found in hot stars. Photometric spots also appear in magnetic chemically peculiar (mCP) stars, but differ in chemical composition rather than temperature. These spots contain an overabundance of certain elements, which alters the spectral distribution of the radiation emitted from the star's surface. (Mikulášek & Zejda 2013).

Most of the rotationally variable classes belong to cold stars, which do not belong to the subject of interest for this thesis. The two main classes associated with hot stars are elliptical variables, discussed in the paragraphs above, and CP stars, which will be discussed below.

### CP stars

Chemically peculiar (CP) stars, such as Ap and Bp stars, are distinguished from other stars by the letter "p" in their spectral classification. Their spectra show an overabundance of certain heavy elements and a deficiency of others, accompanied by slower rotation. This slow rotation results in relatively stable photospheric layers maintained by large-scale magnetic fields of fossil origin. The magnetic dipole axis of these stars typically does not align with their rotational axis. CP stars with strong magnetic fields are classified as magnetic CP (mCP) stars. In addition to spectroscopic

peculiarities, they may exhibit stable photometric spots that cause brightness variations (Mikulášek & Zejda 2013). This variability arises from radiative diffusion, which lifts elements with high cross-sections.

The appearance and chemical composition of CP stars vary significantly between individual stars. Modified Preston-Maitzer classification shown in Table 1.2 is used to classify these objects.

Table 1.2: Characteristics of CP stars taken from (Preston 1974) and revised with (Mikulášek & Zejda 2013).

Type	Classical Name	Temperatures [K]	Characteristics
CP1	metallic (Am)	7000 – 10000	weak Ca II, Sc II, enhanced heavy metals
CP2	magnetic (Ap, Bp)	7200 – 15000	enhanced Si, Cr, Sr, Eu, etc.
CP3	HgMn	10000 – 15000	enhanced Hg II ( $\lambda$ 3984), Mn II
CP4	He-weak	13000 – 20000	enhanced Si, weak He
CP6	He-strong	–	enhanced He

### 1.3 Eclipsing binaries

Eclipsing variable stars are a class of extrinsic variables consisting of at least two bodies orbiting a common centre of mass. The system's orientation must be such that one star partially or fully blocks the other's light from the observer's viewpoint, causing periodic brightness variations. The shape of the light curve depends on factors such as the size, temperature, and luminosity of both stars, as well as their separation. The gravitational interaction between the components defines their Roche lobes, which influence mass transfer and system evolution. Based on how the Roche lobes are filled, eclipsing binaries can be categorized into detached, semi-detached, over-contact, and double-contact systems (Wilson 1979).

Eclipsing binaries are further classified by their light curve morphology into EA (Algol type), EB ( $\beta$  Lyrae type), and EW (W Ursae Majoris type). EA systems consist of detached components with flat light curves between eclipses. EB binaries are semi-detached systems with continuous light variations due to the gravitational distortion of the stars. EW binaries, or W UMa systems, are contact binaries with continuously varying brightness and nearly equal eclipse depths (Mikulášek & Zejda 2013). Some close binary systems also exhibit sinusoidal variability due to the ellipsoidal shape of the components, where tidal distortions cause periodic changes in brightness even outside eclipses. However, obtaining purely sinusoidal variations is challenging and occurs only in specific cases where the stars' shapes, orientations, and orbital properties create near-perfect periodic modulations.



## Chapter 2

# Uncovering sinusoidal variability from photometry

Photometric variability can reveal important information about stellar properties and evolution. This chapter focuses on the identification of sinusoidal variables in the photometric data from (*TESS*). It describes the systematic selection process that was applied to isolate objects with well-defined periodic variations from a large initial sample of stars. The following section introduces the *TESS* mission and its observational capabilities, providing context for the data used in this study.

### 2.1 Data sources and initial sample

*TESS* is a space-based observatory designed to monitor the brightness of stars across nearly the entire sky. Its primary goal involves the detection of exoplanets around bright nearby stars using the transit method, where a planet passing in front of its host star causes a periodic decrease in brightness. These stars are the most suitable targets for follow-up characterization with ground-based telescopes, as well as the *Hubble telescope* and *James Webb Space Telescope*. Beyond exoplanet detection, *TESS* is also a valuable tool for stellar astrophysics, enabling studies of stellar variability, asteroseismology, and binary systems. Its high-precision photometry provides insight into a wide range of astrophysical phenomena.

The *TESS* instrument consists of four identical wide-field cameras designed for continuous sky monitoring. Each camera has a 100 mm effective pupil diameter and a CCD detector, covering a  $24^\circ \times 24^\circ$  field of view. Together, they create a combined field of view of  $96^\circ \times 24^\circ$ , aligned along the ecliptic longitude, with one camera centred on an ecliptic pole (Vanderspek et al. 2018). The detectors operate in the red wavelength range of 600 to 1040 nm, corresponding to peak emissions of G and K-type stars - hosts to Earth-like exoplanets. *TESS* is thermally controlled and mounted on a stable platform to ensure precise photometry, with data processed onboard before being downlinked to Earth for further analysis at NASA Ames Research Center.

To cover both hemispheres, *TESS* occupies a highly stable, inclined, highly eccentric 13.7-day orbit in 2:1 resonance with the Moon (Gangestad et al. 2013). This configuration stabilizes observations and minimizes correctional manoeuvres while avoiding Earth's and Moon's eclipses. The satellite remains above Earth's radiation belts, ensuring a low-radiation, thermally stable environment.

*TESS* follows a systematic observation strategy, dividing the sky into sectors, each observed for two orbits (27.4 days). The field of view shifts by  $26^\circ$  after each period, with adjustments to avoid scattered light contamination from Earth and Moon (Vanderspek et al. 2018). Figure 2.1 illustrates sector locations during the primary mission, spanning the first and second year of

observations. Currently, *TESS* observes sectors within year 7 of observations, which belong to the second extension of the mission.

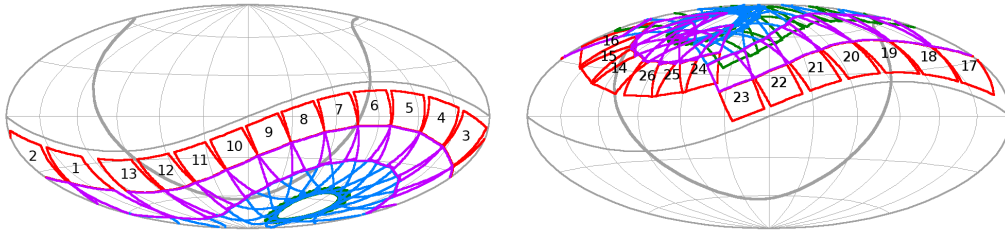


Figure 2.1: *TESS* sky coverage maps in the ecliptic coordinate system. The figures represent sectors observed during the primary mission (MIT n.d.).

Data products include Target Pixel Files (TPFs), Light Curve Files (LCFs), and Full-Frame Images (FFIs), processed at various cadences (2 minutes, 20 seconds, and 10 minutes). All data undergo processing through the Science Processing Operations Center (SPOC), where instrumental effects are corrected, and systematic trends are removed, including pixel-level calibration, background subtraction, aperture photometry, identification and removal of systematic errors and search for transits (Ricker et al. 2015). The SPOC pipeline generates high-quality light curves aboard the spacecraft from TPFs using Simple Aperture Photometry (SAP) and Pre-search Data Conditioning SAP (PDCSAP) flux (Twicken et al. 2010). Additionally, the SPOC pipeline extends its processing to Full Frame Images (FFIs), producing light curves at cadences of 30 minutes, 10 minutes, and 200 seconds. These FFI-derived LCFs are labelled under the provenance name "TESS-SPOC", distinguishing them from those extracted directly from TPFs. The MIT Quick-Look Pipeline (QLP; Huang et al. (2020a) and Huang et al. (2020b)) extracts light curves from FFIs for stars brighter than  $T = 13.5$  mag, offering broader coverage but with more systematic noise.

The *TESS* Input Catalog (TIC) helps identify target contributions, with TIC-8 incorporating over 1.5 billion stars from *Gaia* DR2. All calibrated data are publicly available through the Mikulski Archive for Space Telescopes (MAST) [E3]. In this thesis, I use the `Lightkurve` Python package to download, visualize, and process *TESS* light curves, leveraging its integration with `Astropy` and `Matplotlib` for efficient analysis.

The initial sample of stars for selecting sinusoidal variables was drawn from the TIC catalogue and limited to spectral types O, B, A, and F, ensuring atmospheres stable enough to host star spots. To ensure we get only the stars of desired spectral type and to reflect the division between hot and cold stars—a key criterion for constraining the sample—we applied a lower limit on the effective temperature ( $T_{\text{eff}}$ ). Since the exact boundary between hot and cold stars is not well-defined, we considered multiple definitions:

- 6000 K - the minimum effective temperature for F-type stars
- 6700 K - the effective temperature of F5 spectral class [E4] that defines the transition between cold and hot stars related to the Kraft break
- 7000 K - the effective temperature of the F2 spectral class, identified as a dividing line between hot and cold stars by (Mikulášek 2021)

To account for stars near this transition region, we adopted 6500 K as the temperature threshold. This value represents an average between the lower limit for F-type stars and the value proposed by Mikulášek (2021), set to include the objects undergoing rotation breaking (see Chapter 1 for

more details). This choice balances the need to include stars affected by rotational braking while minimizing contamination from cooler stars, which may exhibit variability due to convective processes rather than the mechanisms of interest.

The second criterion for the star selection was introduced for practical reasons - ensuring the stars were bright enough for high-quality spectroscopic follow-up. Since high-resolution echelle spectra with good signal-to-noise (S/N) ratios were required, we restricted the sample to stars with Johnson *V*-band magnitudes lower than nine, making them suitable for observation with 1-meter-class telescopes. More details about the instruments used for spectroscopic observations are provided in Chapter 3.

The initial sample comprised 45 780 stars. Table 2.1 presents the distribution of effective temperatures and spectral types within this sample, and Table 2.2 the distribution of magnitudes. In the TIC catalogue, effective temperatures for hot stars are sourced either from spectroscopic surveys or *Gaia* DR2. These temperatures are derived using the distance-independent  $G_{BP} - G_{RP}$  colours from the Apsis processing pipeline (Andrae et al. 2018). The accuracy of these temperature estimates declines for stars cooler than 4000 K due to the presence of molecular bands and for stars hotter than 12 000 K due to the reduced sensitivity of *Gaia* passbands at higher temperatures. As a result, temperature estimates beyond this upper limit are only approximate, which may lead to some uncertainty in the distribution of O and B stars within the initial sample. It is perhaps not surprising that there is a significantly larger percentage of A and F-type stars - lower-mass stars dominate the population of nearby stars, probed by the *Gaia* satellite, and they also live a lot longer.

Table 2.1: Distribution of spectral types in the initial sample of stars

Type	Temperatures [K]	Number of Stars	Percentage [%]
O	> 25000	6	0.013
B	11000 – 25000	5290	11.555
A	7500 – 11000	23261	50.810
F	6000 – 7500	17223	37.621

Table 2.2: Distribution of magnitudes in the initial sample of stars

Magnitude Range	Number of Stars	Percentage [%]
0–1 mag	4	0.009
1–2 mag	2	0.004
2–3 mag	28	0.061
3–4 mag	110	0.240
4–5 mag	435	0.950
5–6 mag	1425	3.113
6–7 mag	4232	9.244
7–8 mag	11031	24.096
8–9 mag	28513	62.283

These objects were processed using an automated Python script that generated visual representations of key stellar characteristics inspired by images generated in the work [Skarka et al. \(2022\)](#), which can be seen in Figure 2.2.

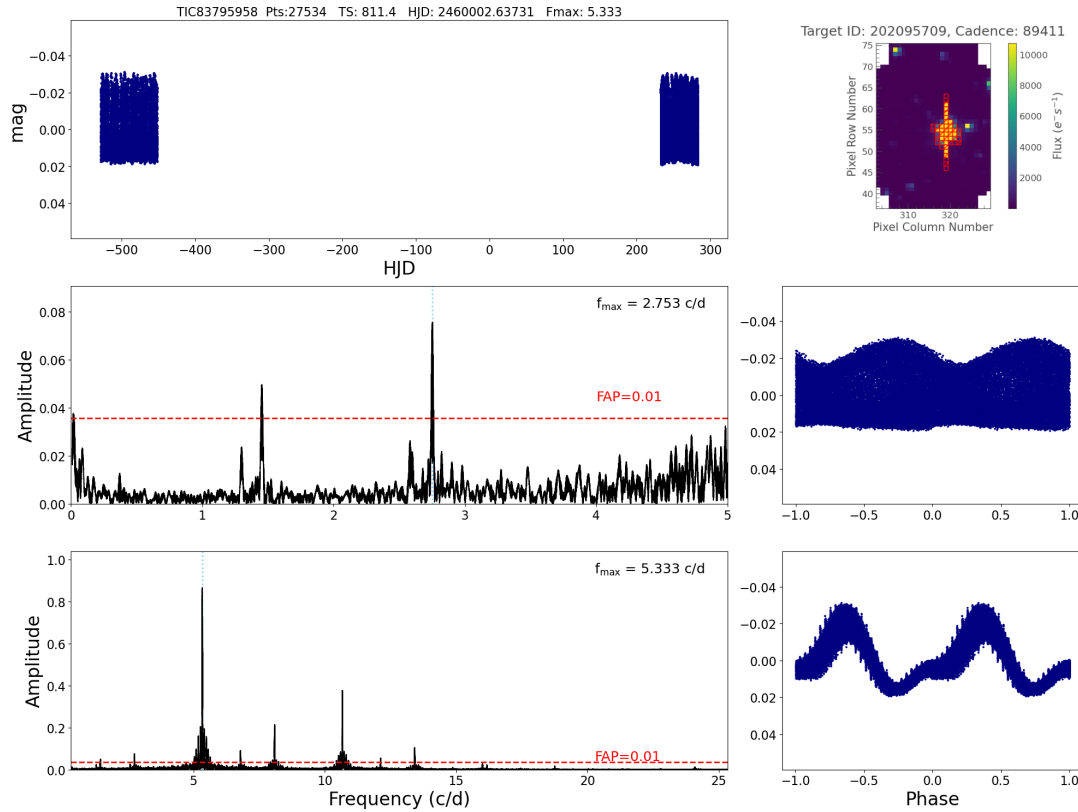


Figure 2.2: Quick look images visualizing key stellar characteristics.

The visual representations for the initial sample of stars were generated in December 2023, using data available up to Sector 72, which corresponds to Cycle 6 of *TESS* observations. The analysis pipeline downloaded all available sectors for the selected targets from the MAST archive using the `Lightkurve` library. The primary source of data for the analysis was the LCF files with the provenance name `TESS-SPOC`, as most stars did not have available `SPOC` data for the observed sectors. The QLP routine removes large-amplitude variations by applying a high-pass filter, effectively cleaning the data. However, a more reserved approach was decided in order to avoid losing information about the targets. The light curves from different sectors for each target were stitched together, and their flux  $F_i$  was recalculated to relative magnitudes  $\Delta m_i$  using Pogson's equation:

$$\Delta m_i = -2.5 \log \left( \frac{F_i}{F_{\text{mean}}} \right), \quad (2.1)$$

where  $F_{\text{mean}}$  was the mean observed flux. Similar to [Skarka et al. \(2022\)](#), no additional detrending was applied at this stage of processing since the `PDCSAP` light curves were generally free of significant outliers. The light curves of individual objects are drawn at the topmost plot in Figure 2.2. Any remaining instrumental noise was addressed through careful manual inspection and further cleaning, but this was only done for stars in the final sample (see Chapter 4 for more details on the process).

Stellar variability in photometric data can be identified through the time domain in the form of light curves or in the frequency domain using frequency diagrams (also called periodograms). Lombscargle periodograms (Lomb 1976, Scargle 1982) were used to analyse the signal periodicity of unevenly distributed data. To assess the significance of detected signals, we relied on the false alarm probability (FAP), which quantifies the likelihood that a peak arises from random noise rather than a true periodic signal. A peak is considered significant if its FAP falls below a chosen threshold, depending on the confidence level required. Lower FAP values indicate stronger detections, ensuring that only statistically robust periodicities are interpreted as real signals (VanderPlas 2018).

In Figure 2.2, the amplitudes of variations identified from the frequency analysis of TESS-SPOC light curves are shown in two frequency regimes. The low-frequency regime, up to 5 c/d, is presented in the second row, while the high-frequency regime, ranging from 5 c/d to 100 c/d, is shown in the third row. The red dashed lines indicate the 1 % FAP of the identified peaks. For each frequency, the light curves were phased to align periodic signals and highlight their behaviour over time, as seen next to the frequency spectra in the figure. This phasing process allows for clearer visualization of periodicity, especially for stars with complex or overlapping signals.

The final component used for the basic classification of stars in the initial sample is the TPF, shown in the upper right corner of Figure 2.2 for the first available sector. It shows how the star was seen by the *TESS* cameras and which pixels were used for the derivation of flux. This aperture is highlighted in red. The TPF allows for an examination of the star’s background and helps identify potential blends in the data.

The figures produced by the Python script enabled rapid identification of sinusoidal variations in the low-frequency regime. The following section outlines the variability identification process and explains the additional steps taken to refine the initial sample.

## 2.2 Variability identification

The initial sample consisted of a large number of stars exhibiting a variety of variability mechanisms (an overview of these mechanisms in hot stars is provided in Chapter 1). To obtain a more focused and manageable dataset, the sample was reduced to include only those targets that are potential candidates for sinusoidal variability induced by rotational modulation. This selection process was carried out through careful visual inspection of diagnostic plots, such as those presented in Figure 2.2.

The first step was to eliminate all objects that didn’t exhibit sinusoidal variability in the low-frequency regime. Because we primarily looked for candidates of rotational variability, we assumed the changes wouldn’t have frequencies larger than 5 c/d. According to Nielsen et al. (2013), rotational periods of hot stars, derived from observations obtained by the *Kepler* satellite, decrease with increasing effective temperature. For B- and A-type stars, typical rotational periods range from approximately one to two days, as illustrated in Figure 2.3. Furthermore, the rotational periods of main-sequence stars are constrained by the critical break-up limit, where the centrifugal force at the stellar equator balances gravitational attraction. The equation for the derivation of a critical rotational period can be written in the following form:

$$P_{\text{crit}} = \sqrt{\frac{3\pi}{G\bar{\rho}}}, \quad (2.2)$$

where  $\bar{\rho} = M/(\frac{4}{3}\pi R^3)$  is the mean density of the star and  $G$  is the gravitational constant. If the body rotated faster, the material from the star would be launched off into space, making the object unstable. The mean density for individual spectral classes can be derived from the average mass

and radius of stars of said spectral types. Table 2.3 shows the mean values of mass  $M$  and radius  $R$  taken from [Carroll & Ostlie \(1996\)](#), and calculated mean density  $\bar{\rho}$  used for the determination of critical rotational period  $P_{\text{crit}}$  and frequency  $f_{\text{crit}}$ .

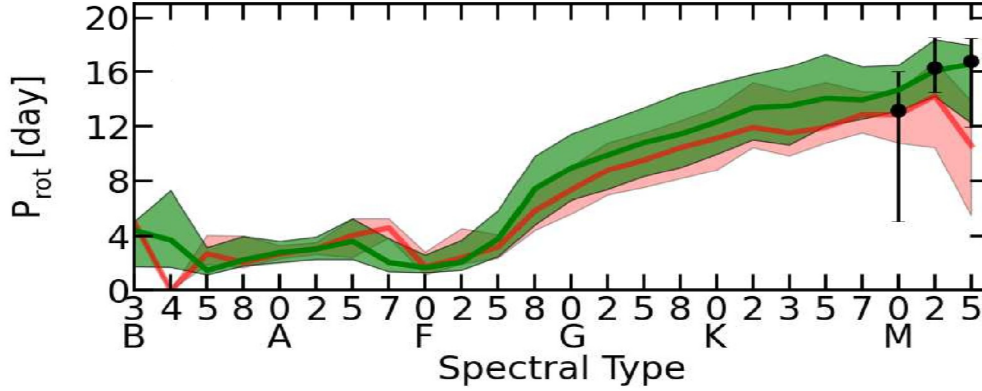


Figure 2.3: Rotational periods of main sequence stars observed by *Kepler* (green line; taken from [Nielsen et al. \(2013\)](#)). The distribution is compared to data taken from [McQuillan et al. \(2013\)](#) - black points with error bars; and with [Debosscher et al. \(2011\)](#) - red line. Shaded lines represent areas of the 34th percentile from the median.

Table 2.3: Critical rotational period for stars of various spectral classes. Masses  $M$  and radii  $R$  were taken from [Carroll & Ostlie \(1996\)](#). Density  $\bar{\rho}$ , critical period  $P_{\text{crit}}$  and frequency  $f_{\text{crit}}$  were calculated using Equation 2.2 and classic formulas.

Type	$M [M_{\odot}]$	$R [R_{\odot}]$	$\bar{\rho} [\text{kgm}^{-3}]$	$P_{\text{crit}} [\text{d}]$	$f_{\text{crit}} [\text{c/d}]$
O	60.00	13.40	35.08	0.73	1.36
B	5.90	3.20	253.29	0.27	3.66
A	2.00	1.80	482.43	0.20	5.05
F	1.40	1.20	1139.74	0.13	7.76

As shown in Table 2.3, hot stars — particularly F-type stars — can reach rotational frequencies of up to 8 c/d. However, this represents an extreme upper limit, and most stars rotate at significantly lower rates. Therefore, focusing on the low-frequency regime remains a suitable and reliable approach for identifying sinusoidal variables within the initial sample.

When examining the phased light curves in the low-frequency regime, we focused on the shape of the minima and maxima, their symmetry, and the amplitude of the variations. Objects with amplitudes of their light curves below 0.1 mmag were excluded from the sample. An extremely weak photometric signal may be caused by noise or instrumental effects, or likely corresponds to very low radial velocity amplitudes. This threshold was set to ensure that the signal would be strong enough for follow-up spectroscopic observations using the available telescopes.

In the second step of the visual inspection, we looked at the high-frequency regime of the frequency spectra. Since identifying and classifying high-frequency pulsations was beyond the scope of this thesis, all stars showing such variations were excluded from the sample.

Additionally, variations observed in the high-frequency regime can sometimes result from reflections of lower-frequency signals rather than genuine high-frequency pulsations. This phe-

nomenon arises due to the Nyquist frequency, which represents the highest frequency that can be accurately detected in regularly sampled data and is defined as half the sampling rate. For TESS-SPOC long-cadence 30-minute data, the Nyquist frequency was approximately 24 c/d. Frequencies higher than this limit are "folded back" into the observable frequency range, appearing as aliases at lower frequencies. Aliases occur at frequencies that are reflected into the lower-frequency range, with the Nyquist frequency acting as a boundary. Signals do not simply reflect once; rather, they fold repeatedly at each multiple of the Nyquist limit, creating higher-order aliases that appear as mirrored signals in the observable frequency range. For example, with a Nyquist frequency of 24 c/d, signals will fold into the observable range at frequencies such as 48, 72, or even 96 c/d, creating aliases at these locations. TESS-SPOC also has various cadences during the extended missions—30-minute, 10-minute, and 200-second data. Therefore, particular attention was given to identifying and discarding such aliases during the candidate selection process, ensuring that the final sample contained only stars with genuine low-frequency sinusoidal variability.

The last step of the visual inspection included identifying the origin of the incoming photometric signal and the elimination of blends. For this purpose, we looked at the TPF of the object and inspected the star background. If there was no other bright object in the defined aperture and the position of the bright star corresponded with the position of an object from which the flux was taken, the signal was considered to be real. A detailed examination of star backgrounds was done for objects from the final sample.

During the examination, non-phased light curves of objects were checked for any deformations or peculiarities - for example, minima of various depths that are indicative of binarity or pulsation envelopes. Stars whose light curves did not exhibit sinusoidal variations in their signals - barring instrumental deformations - were excluded from the sample. Many objects had data from different sectors that were visible as only clusters of points. In these cases, the light curves themselves were not examined at this step of sample reduction.

The reduced sample of stars consisted of 472 objects. While visual inspection was a crucial part of the selection process, it came with certain limitations. Some stars remained in the sample even when their low-frequency phase curves deviated slightly from a perfect sinusoidal shape. In these cases, it was often difficult to determine whether the irregularities were caused by intrinsic stellar variability or simply the result of noise and scatter in the data points. Additionally, for several candidates, the Target Pixel Files (TPFs) were not available. However, given the large size of the sample, it was not feasible to investigate every case in detail at this stage. Instead, these objects were carried forward, with the understanding that a more thorough examination — including checks for contamination and verification of variability sources — would be performed during the final vetting of the selected candidates.

Another challenge was the inability to reliably identify certain types of variability within the sample — in particular, binary stars and stars with light curve modulation. The combined effect of data scatter, instrumental artefacts, and the subtlety of these signatures made them difficult to distinguish at this stage. However, these objects were not of interest for the purpose of this study, which focused on rotational variability; therefore, the next stage of data examination aimed to eliminate these objects from the data sample.

## 2.3 Finalization of sample

The finalization of the sample required a careful preliminary analysis. For each of the 472 objects in the reduced set, the moment of the first minimum ( $M_0$ ) and the frequencies of variations were determined. With these parameters established, the presence of strictly sinusoidal variability could be assessed, allowing the selection of objects suitable for further detailed study.

The frequencies of variations were derived from the low-frequency frequency spectra during the creation of figures that showed important characteristics for each target. The moment of the first minimum was fitted from the photometric data using a high-order polynomial. The minima were fitted in the middle of the light curves to ensure robust phase alignment, where the time coverage was most balanced and less affected by edge effects or potential long-term trends.

Deviations from the sinusoidal shape of the light curves were detected by fitting the data with two functions. First, the data was fitted by a simple sine function shown in the Equation 2.3, and afterwards also with a function containing two sine functions, one of which was twice the frequency of the other one, shown in the Equation 2.4. In these equations,  $a_1$  and  $a_2$  were the amplitudes of variations,  $f$  was the frequency derived from initial data analysis, and  $\phi_1$  and  $\phi_2$  were the phases. The fits obtained from both functions are shown in Figure 2.4.

$$y = a_1 \sin(2\pi ft + \phi_1) \quad (2.3)$$

$$y = a_1 \sin(2\pi ft + \phi_1) + a_2 \sin(\pi ft + \phi_2) \quad (2.4)$$

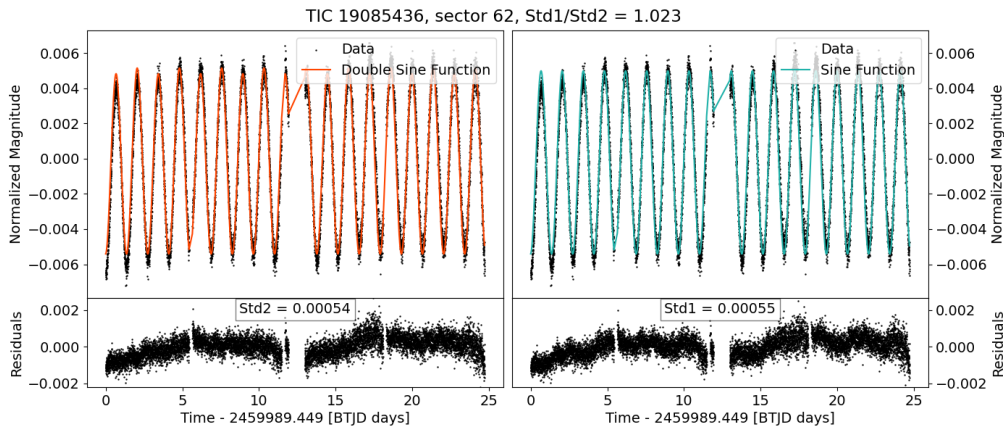


Figure 2.4: Residual figures after fitting the data with a simple sine function (blue data) and a function containing two sines (orange data). The figure contains standard deviations of residua and their ratio used for sinusoidal variability identification.

The orange curve represents the model light curve fitted using Equation 2.4, while the blue curve shows the model based on Equation 2.3. After fitting the data from a chosen sector, the residual values were calculated as a difference between observed data and the model, and the standard deviations of these residuas (Std1 for single sine function and Std2 for double sine function; see values in the plot in Figure 2.4) were calculated. By comparing these two values, it could be determined how well the individual functions fit the data. The ratio of standard deviations, Std1/Std2, served as an indicator of the relative goodness of fit and was provided at the top of each figure, alongside the star's name and the number of sector used for fitting.

Four criteria were applied for the selection of sinusoidal variables based on the residual figures. First, the ratio of standard deviations Std1/Std2 could not be above 1.1. Ideally, the single-sine function and the double-sine function would fit the data in the same manner, meaning the residual ratio would be equal to one; however, due to data scattering, the double-sine function fitted the data slightly better in almost all cases. The threshold of 1.1 was set empirically through manual examination and testing, as the point beyond which differences between the fits could no longer be explained by scatter alone. Ratios exceeding this limit indicated that the double-sine function captured intrinsic variations in the light curves rather than random noise. Such variations, often

reflected in alternating depths of consecutive minima and suggestive of binarity, led to the exclusion of these objects from the final sample. An example of a star with a residua ratio above the threshold value can be seen in the top plot in Figure 2.5.

The second criterion rejected stars with light curve modulation due to beating (Zhabinskaya n.d.). Beating appears whenever two close frequencies are present in the data. However, in the case of stars, this phenomenon cannot be explained by rotation, as a hot star with stable spots without differential rotation cannot rotate at two different frequencies simultaneously. Instead, beating is a signature of a variable star with multiple period variations. These frequencies interfere with each other, producing a characteristic modulation in the amplitude of the observed light curve. Instead of showing a simple, steady sinusoidal variation, the brightness of the star fluctuates with cycles of increasing and decreasing amplitude. This pattern, known as a beat pattern, arises from the constructive and destructive interference between the pulsation frequencies. In light curves, beating can manifest as long-term variations superimposed on shorter, regular oscillations. In the middle plot in Figure 2.5 is a star with visible light curve modulation due to beating in the observed data. The residua ratio nor scatter of the data in the residuas themselves do not indicate any deviations from the sinusoidal shape. However, the modulation is visible in the light curve beyond the fitted models.

The third criterion for selecting sinusoidal variables was related to changes in the period or shape of the photometric data. Stars that showed a gradual increase in residuals from the middle of the fitted region, as seen in the bottom plot of Figure 2.5, exhibited a slow change in the period of their light variations. This caused a significant deviation between the fitted model and the observed data. Such stars likely experienced long-term variations or trends not accounted for by the sinusoidal model, leading to significant discrepancies between the fitted and actual light curves. A similar effect was observed in stars with imprecise frequency values. However, in these cases, the trend in the residuals disappeared when the frequency was treated as a free parameter, allowing them to be evaluated using the first and second criteria.

In the final criterion, each star was individually examined to see if its light curve showed significant deviations from a purely sinusoidal shape. The residua of these stars contained visible periodical trends that could not be associated with instrumental noise or the scatter of the data. An example of a star rejected due to this criterion is shown in the bottom-most plot in Figure 2.5.

After applying these criteria, many stars were excluded, leaving a final sample of 108 candidates for further spectroscopic follow-up. Table 2.4 presents the number of stars rejected by each of the four criteria, along with their percentage representation. Among the 472 objects, nearly forty percent were binaries with alternating minima depths that could not be resolved visually from the phase diagrams due to the scatter of data and instrumental deformation of the light curve. This shows the importance of careful examination of available datasets.

Table 2.4: Distribution of stars rejected due to criteria imposed by the study of their residua

	Number of stars	Percentage [%]
Residua ratio above 1.1	171	36.2
Light curve modulation	47	10.0
Period change	14	3.0
Non-sinusoidal shape	132	27.9
Final sample	108	22.9

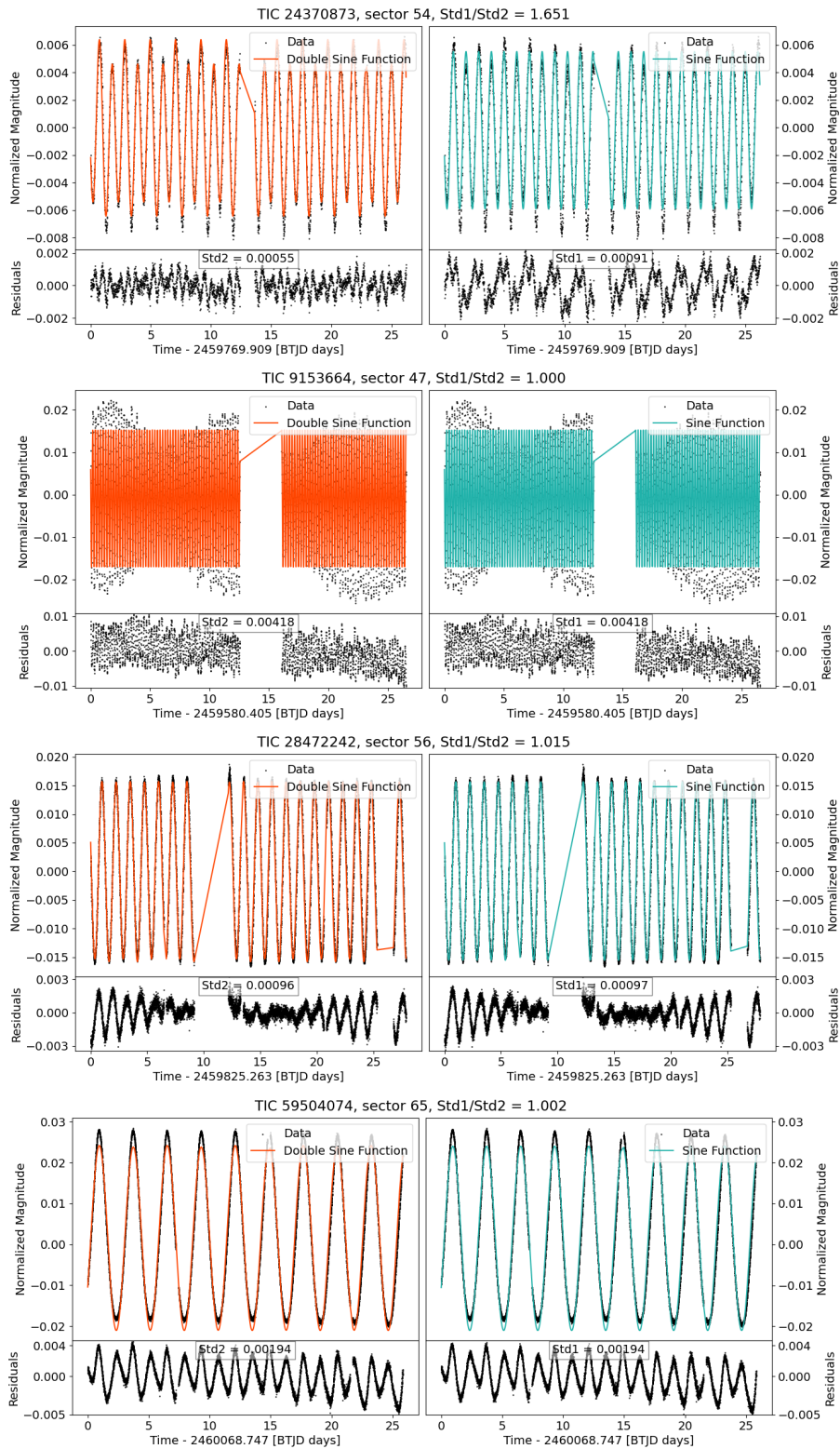


Figure 2.5: Stars that did not satisfy the criteria imposed on residual figures. The first star has minima of different depths, the second shows light curve modulation, and the third and fourth show changes in the period and non-sinusoidal shape of the curve, respectively.

To visualize the selection process, each group of stars in the Hertzsprung-Russell diagram in Figure 2.6 represents different stages of filtering based on the applied criteria. The HR diagram was constructed by plotting the initial sample of stars, which are represented as small grey dots, followed by the reduced sample (orange dots) and the final sample (teal dots). Stars marked with an "x" in the diagram indicate those that have also undergone spectroscopic measurements (see Chapter 3 for more details). The diagram is based on effective temperature  $T_{\text{eff}}$  plotted against the absolute visual magnitude  $M_V$  calculated using the following formula:

$$M_V = V + 5 \log(\pi) + 5, \quad (2.5)$$

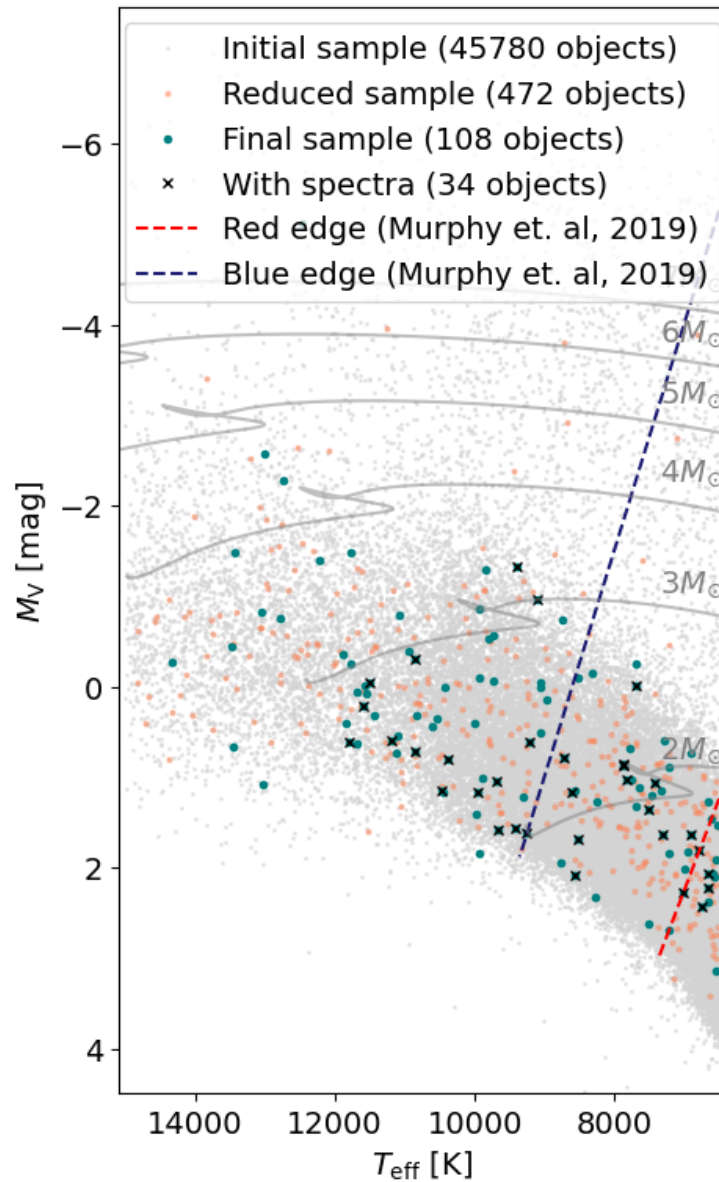


Figure 2.6: HR diagram representing the selection process of sinusoidal variables. The blue and red edge of the instability strip is taken from [Murphy et al. \(2019\)](#) and the evolutionary tracks are taken from [Choi et al. \(2016\)](#).

where  $V$  is the visual magnitude of the object and  $\pi$  is the parallax in arcseconds taken for individual objects from the TIC catalogue. The blue dashed line represents the blue edge of the instability strip, while the red dashed line represents the red edge of the instability strip, taken from [Murphy et al. \(2019\)](#). In addition to the star samples, the HR diagram also includes evolutionary tracks, spaced out by  $1 M_{\odot}$ , which represent the predicted evolution of stars of different masses ([Choi et al. 2016](#)). These tracks help illustrate how stars evolve from the main sequence to the later stages of their life cycle, providing context for the positions of the stars in the diagram.

The final sample of stars was divided into stars observable in the southern sky and stars observable in the northern sky, based on their declinations. The distribution of spectral types in the individual hemispheres can be seen in [Table 2.5](#). Overall, 45 targets could be observed in the north and 63 targets in the south.

Table 2.5: Distribution of spectral types in the final sample of stars

Type	Temperatures [K]	Position	Number of stars	Percentage [%]
O	>25000	north	0	0
		south	0	0
B	11000 - 25000	north	9	8.33
		south	18	16.67
A	7500 - 11000	north	25	23.15
		south	31	28.70
F	6500 - 7500	north	11	10.19
		south	14	12.96

## 2.4 Other objects

During the visual inspection of the photometric data from the *TESS* satellite, several intriguing objects were identified that, although not included in the final sample of sinusoidal variables, are worth mentioning due to their unique characteristics.

Among these were heartbeat stars — a fascinating class of eccentric binary systems named for the distinctive shape of their light curves, which resemble the pattern of a heartbeat on an electrocardiogram. These variations are caused by tidal distortions during close approaches of the two stars in their highly elliptical orbits. At periastron, the gravitational interaction between the stars leads to a brief but pronounced brightening or dip, often followed by smaller oscillations ([Fuller 2017](#)). While these stars did not meet the selection criteria for the final sample due to their complex, non-sinusoidal light curves, their presence in the data highlights the diversity of stellar variability captured by *TESS*. Noting these discoveries emphasizes the importance of careful visual inspection, as it can reveal dynamic stellar phenomena that might otherwise go unnoticed in purely statistical filtering. In the top left corner of [Figure 2.7](#) there is a candidate for heartbeat star; TIC 209558524 was only observed in large sky surveys and has not been studied independently.

Another interesting category of stars found in the sample were various systems with multiple components with reflections or other phenomena that created unique light curves. The description of all the possibilities of how these objects could have been created is not within the scope of this work. Therefore, they will be only crudely presented in this section without detailed analysis. One such object is TIC 238460373 seen in the top right plot in [Figure 2.7](#) - there are no works detailing

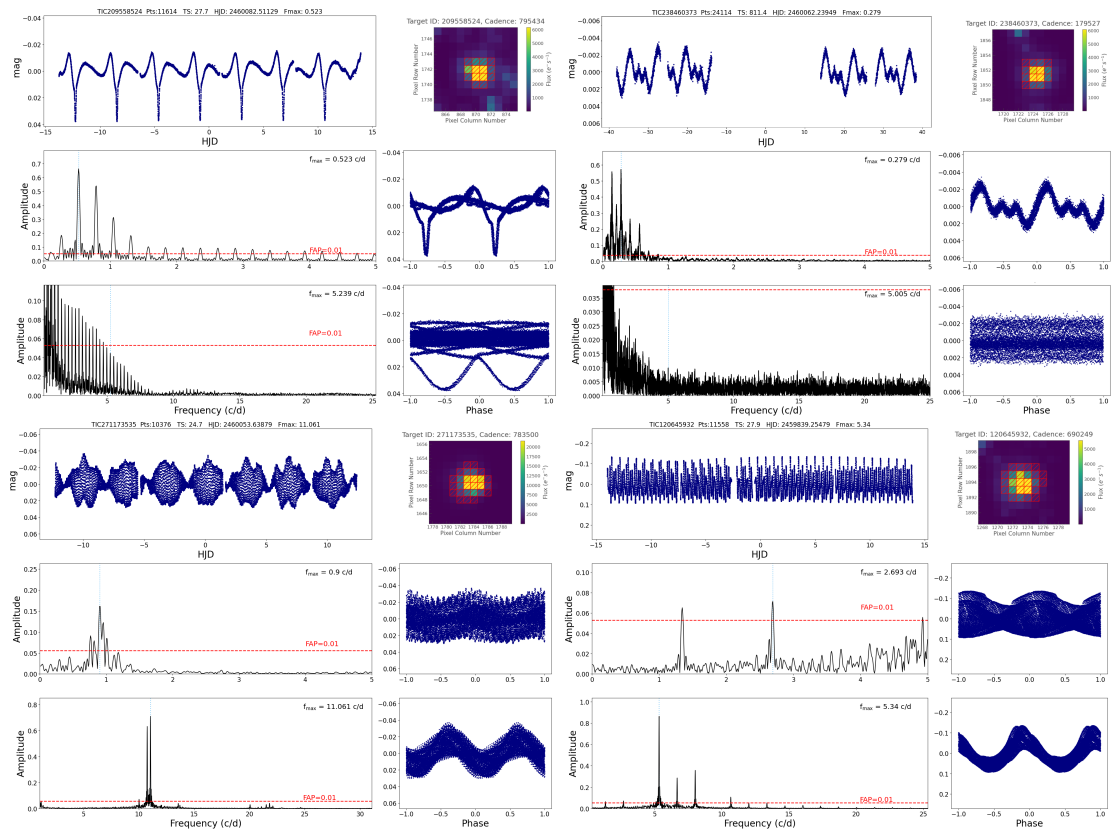


Figure 2.7: Interesting objects

the peculiar shape of its light curve, and it could prove to be an interesting candidate for further study.

The object shown in the bottom left corner of Figure 2.7 belongs to TIC 271173535 and shows strong irregular beating caused by two frequency peaks in the high-frequency regime. The irregularities of this light curve modulation would have to be analysed further using pre-whitening methods on the frequency spectrum of the star. This object is identified in the Simbad database (Wenger et al. 2000) as a multiple-star system; however, there are no references to the beating nor pulsations of this object.

In addition to the heartbeat stars, multiple systems and pulsators, the visual inspection also revealed several high-amplitude DCST (HADS) stars exhibiting signs of beating. HADS stars are a subclass of pulsating variables characterized by large-amplitude, short-period oscillations driven by radial pulsation modes (Xue et al. 2023). TIC 120645932, shown in the bottom right corner of Figure 2.7 is one such star. It has not yet been studied in detail and could prove to be another interesting object.



## Chapter 3

# Spectroscopic observations of selected targets

Photometric data provide valuable insights into the variability of stellar objects, but they are often insufficient to fully determine the underlying mechanisms driving these variations. Therefore, spectroscopic observations are essential for gaining additional information, such as radial velocity measurements and spectral line variations, which help distinguish between different physical processes. To complement the high-precision light curves from *TESS*, spectroscopic data were obtained using the Ondřejov Echelle Spectrograph (OES) (Koubsky et al. (2004), Kabáth et al. (2020)) in the Czech Republic, MUSIKOS spectrograph (Pribulla et al. 2024) [E5] at Skalnaté Pleso, Slovakia, and the PUCHEROS+ spectrograph [E6] in La Silla, Chile.

The following section describes the instruments available for spectroscopic follow-up and the targets selected for further investigation. These observations provided crucial radial velocity measurements to help with the identification of the underlying mechanism of the observed stellar variability.

### 3.1 Data sources and target selection

The sinusoidal variables identified in the *TESS* data were distributed across both the northern and southern hemispheres. From the final sample of 108 objects, 45 targets were accessible for follow-up observations in the northern sky. To obtain spectroscopic data for these targets, two telescopes equipped with echelle spectrographs were available: the OES at Ondřejov Observatory and the MUSIKOS spectrograph at Skalnaté Pleso. The rest of the targets in the final sample (63 in total) were objects observable in the southern hemisphere. Spectroscopic data for these objects were obtained using the PUCHEROS+ spectrograph at La Silla. A description of echelle spectra is provided in the section 3.2.

Observations in the northern hemisphere lasted from April 2024 to the end of February 2025 and in the southern hemisphere from May to September 2024. Despite the initial goal of obtaining spectroscopic observations for all 108 objects in our sample, practical constraints such as telescope availability, weather conditions, and competing observation programs limited the number of targets that could have been observed. Given these restrictions, the most promising candidates were prioritized based on factors such as their brightness, variability characteristics, and observational feasibility within the allocated telescope time.

## OES

The Ondřejov Echelle Spectrograph (OES) is mounted on the 2-meter Perek telescope at Ondřejov Observatory, located approximately 30 km southeast of Prague. Operated by the Astronomical Institute of the Czech Academy of Sciences, this instrument has been in use since 2007 and is primarily dedicated to ground-based exoplanet follow-up observations and stellar astrophysics. The spectrograph is situated in a thermally isolated room at the Coudé focus of the telescope, minimizing environmental influences on spectral stability. The limiting magnitude for observations with the spectrograph is around 13 mag in the  $V$  filter. However, a more reasonable limit with sensible exposure times would be lower. Additionally, the instrument offers the option of using an iodine absorption cell, which enhances radial velocity precision by providing a stable wavelength reference (Kabáth et al. 2020).

## MUSIKOS

The MUSIKOS spectrograph is a high-dispersion echelle spectrograph mounted at the focus of the Nasmyth-Cassegrain telescope at Skalnaté Pleso Observatory in Slovakia. The telescope has a primary mirror diameter of 1.3 meters and is operated by the Astronomical Institute of the Slovak Academy of Sciences. Located at an altitude of 1,786 m above sea level in the High Tatras, the observatory benefits from reduced atmospheric turbulence and lower water vapour content compared to lower-altitude sites [E5]. These conditions improve the quality of spectroscopic observations by reducing absorption and scattering effects in the Earth's atmosphere, leading to more stable and precise measurements of stellar spectra.

## PUCHEROS+

The PUCHEROS+ spectrograph was a high-dispersion spectrograph based on PUCHEROS design (Vanzi et al. 2012) mounted on the ESO 1.52-meter telescope [E7] at La Silla. Located at an altitude of 2,400 m above sea level, La Silla provides excellent observing conditions with minimal atmospheric interference, making it one of the leading sites for high-precision spectroscopy. PUCHEROS+ achieved a radial velocity precision of 20 m/s, enabling the detection of stellar oscillations, exoplanetary companions, and other astrophysical phenomena requiring precise velocity measurements [E6]. The spectrograph was installed on the telescope under Czech leadership as part of the *PLATO* spectroscopic follow-up program (Kabath et al. 2022), which aimed to provide radial velocity confirmation of planetary candidates discovered by the *PLATO* space mission. In November 2024, PUCHEROS+ was decommissioned and replaced by PLATOSpec, a next-generation spectrograph designed to further enhance the capabilities of the observatory.

The data products obtained in each observatory slightly differed in the reduction process. The next section details the process of radial velocity extraction for the data from the available spectrographs and the reduction of said spectra. Although there were slight variations, the image processing followed a similar strategy.

## 3.2 Data reduction

High-resolution spectroscopy provides important information about the wavelength-dependent flux from the observed objects. A commonly used technique for achieving high spectral resolution is echelle spectroscopy (Chaffee & Schroeder 1976), which utilizes a diffraction grating with a high groove density to disperse light into multiple overlapping spectral orders. These orders are then

separated using a cross-disperser, forming a characteristic echellogram, where each order appears as a curved, parallel stripe of spectral data. The resulting two-dimensional echelle spectrum contains a wealth of information but requires careful data reduction to extract scientifically meaningful results.

During observations with an echelle spectrograph, several types of calibration and science frames were produced. The bias frames are taken with zero exposure time and no light entering the detector, correcting the electronic noise and instrument readout noise associated with the used CCD camera. The flat-field frames are images of a uniformly illuminated source used to correct sensitivity variations of individual pixels and the blaze function of the echelle grating. The blaze function can be seen on the science frames, where it reduced the intensity of the spectrum toward the edges of the orders (Škoda et al. 2008). Object frames contain the spectrum of the target star, recorded in two-dimensional echelle orders. The last type of calibration frame is the comparison frame taken using a gas-filled tube with known emission lines, providing a reference for determining the precise wavelength solution across the orders.

Data reduction is a crucial step in astrophysical image processing, as raw observational data are affected by instrumental and environmental factors such as detector noise, cosmic rays, and atmospheric absorption. To correct for these effects and produce calibrated spectra, a standardized data reduction pipeline is applied. In this work, we utilize the Image Reduction and Analysis Facility (IRAF) (Tody 1986), a widely used software package designed for astronomical image and spectral analysis. The reduction process is typically done in several steps:

- Preprocessing - cosmic removal, bias subtraction and flat-field correction
- Order tracing and extraction
- Wavelength calibration
- Continuum normalization - extraction of 1D spectra
- Radial velocity extraction

The first step of data reduction involved the detection and removal of cosmic rays using `dcr` software developed by Pych (2012). The algorithm analyzes the histogram of the image data and iteratively identifies multiple-pixel cosmic rays that are replaced by the average of the counts in the neighbouring pixels (Pych 2004). While this method is generally effective, in some cases, the number of iterations performed by the algorithm was insufficient to fully remove larger multi-pixel cosmic ray events, leaving behind residual contamination in the affected regions. Additionally, the interpolation process used to replace cosmic ray-affected pixels occasionally introduced artificial brightening in the continuum of the spectra. This effect likely arose due to systematic differences between the flux levels of cosmic-ray-impacted pixels and their surrounding values, causing a noticeable increase in the reconstructed continuum (see Figure 3.1). The parameters for the cosmic ray removal were, therefore, fine-tuned by manual inspection to minimize the impact on the continuum while still removing the majority of cosmic rays.

In the next step of the data reduction pipeline, a master bias frame was created as a combination of bias frames for the observation night. Individual bias frames may contain unexpected fluctuations; therefore, the median combination was applied to create a single master bias frame that was subtracted from all other calibration and scientific images. In the pipeline reducing the data from PUCHEROS+, the mean frame was not extracted from the frames directly due to a defect in the frames, where one part of the image was darkening toward the edge, which led to unexpected deformations of the flat-fields and object frames. Instead, the mean intensity of the master bias was extracted and subtracted from the other observations, simulating a frame with constant intensity. A master flat frame was then extracted as a combination of flat-field frames, corrected by master bias

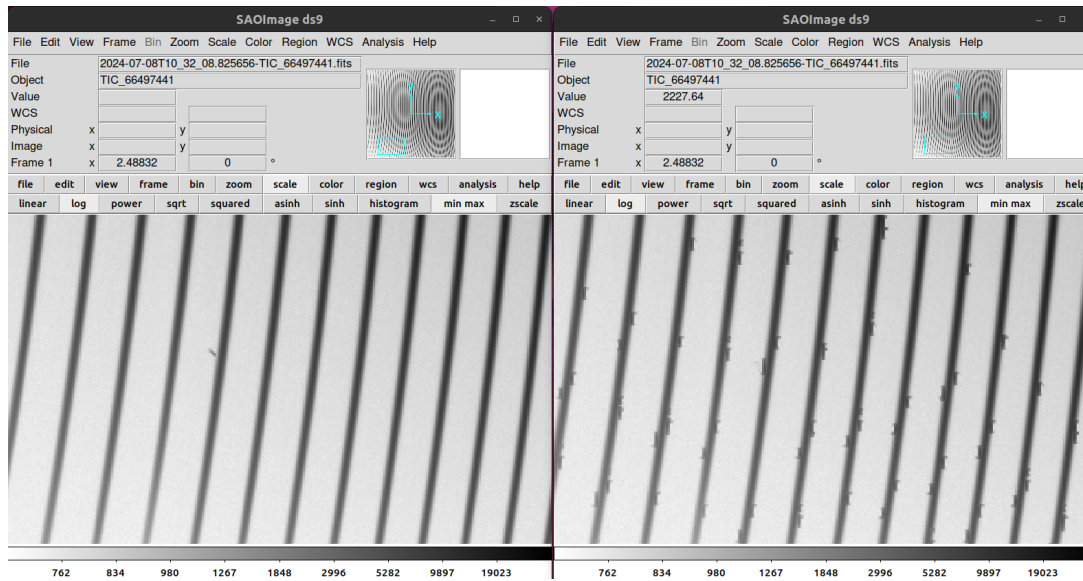


Figure 3.1: Comparison of raw spectra (left side) and spectra reduced with dcr (right side). The image is zoomed to a part of the frame where spectral orders (represented by the dark lines) are deformed by the incorrect configuration of the parameters used for cosmic removal.

mean value. Extreme values within the master flat were replaced so they would not cause problems during processing. The object and comparison frames were then divided by the master flat.

An IRAF task `apa11` was used to trace the apertures and do the extraction of the individual orders, converting the two-dimensional spectra into one-dimensional data. This task was applied to both the object frames and the comparison frames. A reference ThAr spectrum was used to compare the correct wavelengths to each pixel. The lines in individual apertures were identified using a list of ThAr spectral lines and their positions in each aperture, created and provided by Dr. Eike W. Guenther. This wavelength solution was later applied to the science frames. Each science frame for the PUCHEROS+ was accompanied by two comparison frames, one taken before and one after the object image. The wavelength solution was created by interpolating between the wavelength solutions of both comparison files.

Finally, the individual apertures were combined to produce a one-dimensional spectrum. The first aperture was excluded as it was not fully captured within the frames. The resulting spectra covered the following wavelength ranges: 421.0 – 744.6 nm for PUCHEROS+, 396.4 – 919.5 nm for OES and 421.0 – 726.0 nm for MUSIKOS.

Radial velocities were determined from one-dimensional spectra by measuring the displacement of spectral lines due to the Doppler effect, which results from the source’s motion along the line of sight. A shift toward shorter wavelengths (blueshift) indicates motion toward the observer, while a shift to longer wavelengths (redshift) signifies motion away. These shifts can arise from various astrophysical processes, such as surface features moving across a rotating disk, stellar pulsations, or the orbital motion of a star in a multiple system. In binary systems, one star moves toward the observer while the other moves away, often producing a characteristic line combination of these two components in the spectrum.

The radial velocity extraction process began by collecting high-resolution spectroscopic data of the target stars. Spectral lines in the spectral interval 500-580 nm along with other prominent features, were used to track the motion of the star. These lines are particularly useful because their

wavelengths are well known, and their profiles are sensitive to the Doppler shifts induced by the radial motion of the star.

Figure 3.2 illustrates the variation in the  $H\alpha$  line in the spectra of TIC 14400891 over time. The plot shows the wavelength on the x-axis and the phase of observation on the y-axis, providing a clear view of how the  $H\alpha$  line evolves. As the phase progresses, the  $H\alpha$  line splits into two distinct components that move in antiphase to each other, reflecting the dynamic motion of the stars in the stellar system.

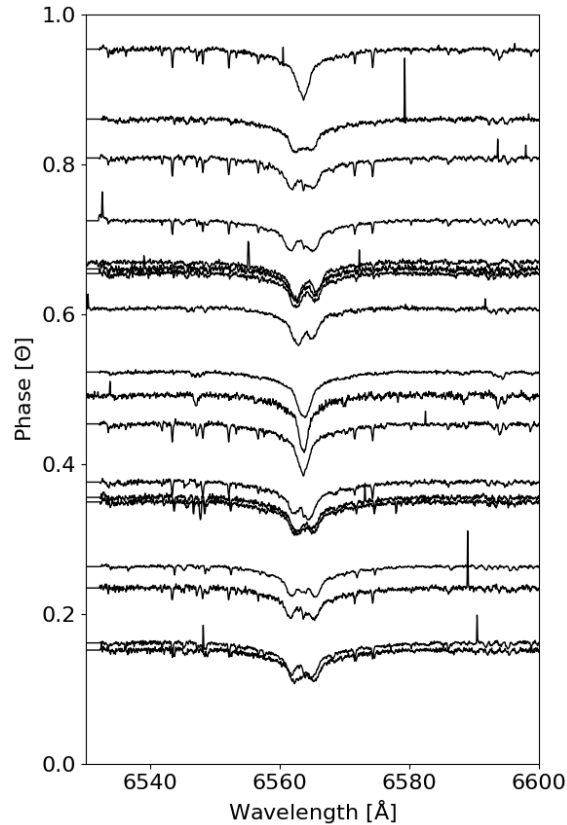


Figure 3.2: Line splitting in the observations of TIC 14400891. The phase  $\Theta$  refers to a specific point in the periodic cycle of the variable system.

Before the calculation of radial velocities, telluric and heliocentric correction was applied to account for Earth's motion around the Sun. In IRAF, radial velocity extraction was performed using the cross-correlation technique, which determines relative velocity shifts between an observed spectrum and a reference template using the task `fxcor`. The reference spectrum was chosen as the best spectrum out of the observations, but for targets with split lines, the spectra were compared to a template single star with a similar spectral type from OES (Štegrner 2020). The task cross-correlated the object's spectrum with a template - either a high-resolution standard spectrum or another spectrum of the same object taken at a different time - by comparing their spectral features. The resulting cross-correlation function (CCF) produced a peak whose position relative to the template determined the velocity shift. This shift was then converted to a radial velocity using the Doppler formula.

### 3.3 Radial velocity analysis

Spectroscopic data were successfully obtained for 22 objects in the southern hemisphere (see Table 3.1) and 12 objects in the northern hemisphere (see Table 3.2). These tables provide fundamental information about the selected targets, including their TIC catalogue identification, sky coordinates (right ascension (RA) and declination (DEC)), effective temperature ( $T_{\text{eff}}$ ), Johnson  $V$ -band magnitude, photometric variability period ( $P$ ) determined from the dominant frequency in the low-frequency regime, and the number of spectra collected for each target ( $N$ ). Additionally, they list the dates of the first and last spectroscopic observations, defining the time span over which each object was monitored.

Table 3.1: Spectroscopic targets in the southern hemisphere

<b>TIC</b>	<b>RA</b> [°]	<b>DEC</b> [°]	$T_{\text{eff}}$ [K]	$V$ [mag]	$P$ [d]	$N$	<b>First</b> <b>spectrum</b>	<b>Last</b> <b>spectrum</b>
31623275	289.08	-34.45	10850	9.0	0.80	8	04/07/2024	21/09/2024
61449214	228.48	-26.05	7700	8.2	0.64	10	25/07/2024	23/09/2024
66497441	356.05	-18.28	11500	5.2	0.38	13	04/07/2024	22/09/2024
84756974	249.99	-39.79	9270	7.8	0.28	7	23/07/2024	14/09/2024
113150902	277.02	-38.36	11200	7.8	1.01	9	04/07/2024	20/09/2024
135081803	184.89	-40.84	7860	8.6	1.34	2	24/07/2024	27/07/2024
137800207	344.07	-23.85	7020	9.0	0.60	11	03/07/2024	15/09/2024
160644410	223.73	-36.43	9430	7.2	1.49	4	25/07/2024	16/09/2024
174214184	234.74	-41.10	6910	8.9	1.07	8	26/07/2024	14/09/2024
205913291	250.40	-28.59	10850	9.0	1.28	7	23/07/2024	03/09/2024
212031970	248.42	-31.29	9690	8.0	0.53	6	29/07/2024	13/09/2024
218160121	261.99	-44.72	7510	8.6	0.22	7	09/05/2024	20/09/2024
220485766	343.50	-54.73	8720	8.9	0.80	11	04/07/2024	22/09/2024
226037840	247.37	-46.26	10390	8.9	0.50	5	26/07/2024	16/09/2024
279821618	239.88	-40.87	8570	8.2	0.46	8	26/07/2024	16/09/2024
292207311	230.93	-27.95	7320	8.9	0.79	6	25/07/2024	24/09/2024
293069615	254.14	-66.11	8610	7.9	1.26	8	23/07/2024	21/09/2024
342829903	205.36	-67.88	6670	8.0	1.58	4	24/07/2024	07/08/2024
351532879	309.16	-63.12	6660	6.3	2.06	9	08/07/2024	15/09/2024
419610625	320.37	-66.67	7830	7.9	1.39	10	08/07/2024	15/09/2024
444577764	267.78	-35.34	11610	8.6	0.62	5	08/07/2024	11/09/2024
448876509	214.29	-68.41	11800	8.4	2.89	7	25/07/2024	17/09/2024

For each spectrum, relative radial velocities were extracted using a custom pipeline described in the section above. Along with the values of relative radial velocities, heliocentric Julian dates (HJD) and errors of the observations were computed. The `fxcor` task computes the relative velocity errors based on the width of the cross-correlation peak and methods used in [Tonry & Davis \(1979\)](#). The

Table 3.2: Spectroscopic targets in the northern hemisphere

<b>TIC</b>	<b>RA</b> [°]	<b>DEC</b> [°]	$T_{\text{eff}}$ [K]	$V$ [mag]	$P$ [d]	$N$	<b>First</b> <b>spectrum</b>	<b>Last</b> <b>spectrum</b>
5638336	32.33	28.39	9210	7.92	2.13	6	06/09/2024	29/12/2024
12321432	32.83	64.15	13490	8.83	2.70	6	06/09/2024	07/01/2025
14400891	127.77	54.08	6790	8.20	2.30	18	27/04/2024	25/02/2025
16878120	232.69	34.47	9680	6.81	0.31	12	27/04/2024	17/02/2025
21673730	255.72	31.69	7880	7.93	1.60	12	27/04/2024	05/09/2024
88815918	27.05	16.96	10470	5.86	1.19	2	06/09/2024	23/09/2024
184607315	31.60	38.90	9390	7.90	1.23	8	05/09/2024	07/01/2025
257456854	257.82	24.25	6750	6.94	1.13	10	28/04/2024	05/09/2024
302581695	133.48	35.54	9100	6.14	1.01	11	27/04/2024	21/02/2025
302666414	163.00	55.36	7420	8.11	1.61	7	30/04/2024	22/02/2025
310932102	262.10	29.84	9960	8.57	1.30	4	19/07/2024	31/07/2024
347699402	263.05	21.26	8520	8.30	3.31	6	19/07/2024	03/08/2024

broader the peak, the greater the uncertainties in determining the velocity shift. The error in velocity is typically proportional to the uncertainty in the wavelength shift, which depends on the resolution of the spectrometer and the signal-to-noise ratio (SNR) of the spectrum. Some of the spectra had a very low SNR, with only a few visible lines. For some of them, estimation of the relative velocities was not possible, as the cross-correlation fit did not converge. Such measurements were excluded from the dataset.

For the observed targets, the number of spectra taken for each of them ranged from 2 to 18, with an average of 8 spectra per object. Sometimes, the changes in the radial velocity curves were not visible when they were phased with the period determined from the photometric variability but became visible for multiples of the dominant period. Figure 3.3 shows the radial velocities for one of the targets, phased with the most dominant period from photometric measurements at the top and twice the period at the bottom of the figure.

The spectral measurements complement photometric data taken from *TESS* and aid in investigating the origin of the variations. The next chapter brings together both photometric and spectroscopic data and reveals the methods used for the identification of the mechanisms responsible for these changes.

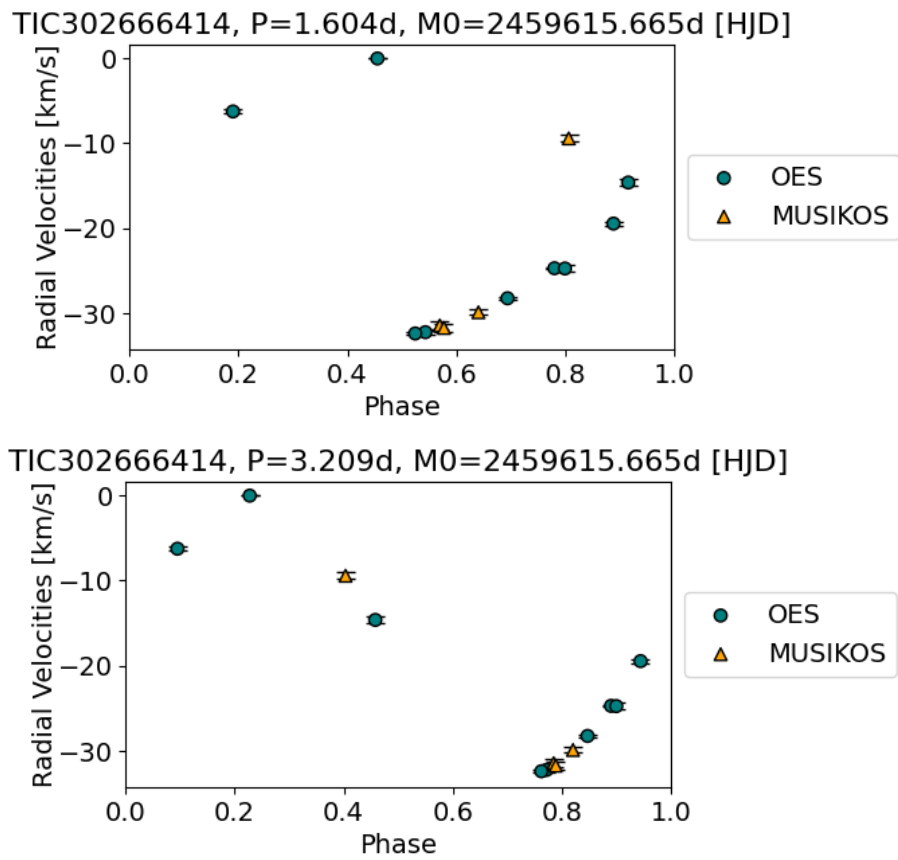


Figure 3.3: Radial velocity curves phased with the dominant period (top figure) and twice the dominant period (bottom figure).

## Chapter 4

# Classification of stars

From the initial sample of stars, we selected 34 targets that exhibited sinusoidal photometric variability and complemented them with spectroscopic observations. This chapter presents a detailed examination of these stars, beginning with a frequency analysis that includes iterative pre-whitening techniques to isolate significant periodic signals and identify dominant modes of variability, followed by the detrending of their light curves to remove instrumental effects. The subsequent sections classify each object based on its variability characteristics. We divide the targets into four categories: binary stars, pulsating stars, spotted star candidates, and objects with uncertain classification due to ambiguous or limited data. The sections below describe the classification criteria and discuss each target individually within its assigned group.

The photometric data for the initial sample of targets were downloaded from the MAST Archive in December 2023. Since then, the *TESS* mission has continued its observations, completing Cycle 6 and beginning Cycle 7 in October 2024 [E8]. During this period, the satellite observed fields in both the northern and southern hemispheres, resulting in new data becoming available for several of the targets. The extended time baseline provided by these additional sectors allows for a more precise determination of variability periods.

To refine the frequency estimates, a software package `Period04` (Lenz & Breger 2004) was used, which is well-suited for analyzing time series with sinusoidal variability and identification of multiple frequencies from the dataset. `Period04` uses a discrete Fourier transform to calculate the frequency spectrum for time series data containing unevenly spaced gaps. In addition to Fourier analysis, the software applies a least-squares fitting routine to model the light curve as a sum of sinusoidal components. This fitting process helps refine the extracted frequencies, amplitudes, and phases by minimising the residuals between the observed data and the fitted model (Lenz & Breger 2005)

For the frequency analysis, photometric time-series data were extracted from the MAST archive [E3], specifically using the long-cadence light curves with the provenance name `TESS-SPOC`. For the analysis, we used the pre-processed `PDCSAP` flux, with removed instrumental trends and well-known systematics. Tables 4.1 and 4.2 summarise the frequency analysis results. For each target, the dominant frequencies were initially estimated using Lomb-Scargle periodograms ( $f_{LS}$ ), used during the construction of preliminary visual representations (see Chapter 2) and were compared with the frequencies extracted through `Period04` ( $f_{P04}$ ). The frequency spectrum of each target was computed up to 100 c/d, and the real frequencies were carefully identified while accounting for possible Nyquist reflections. Special care was taken to distinguish genuine astrophysical signals from their mirrored aliases introduced by the finite sampling rate of the *TESS* observations.

Column  $\Delta P$  in Tables 4.1 and 4.2 shows the difference between the periods corresponding to the initial frequency estimates and the refined values obtained through `Period04`, expressed in

Table 4.1: Comparison of previous ( $f_{LS}$ ) and updated ( $f_{P04}$ ) variability frequencies for stars in the southern hemisphere.  $\Delta P$  is the difference in period using these frequencies,  $f_R$  is the value of Rayleigh criterion and  $f_2$  and  $f_3$  are highest frequencies after removing the dominant frequency.

TIC	$f_{LS}$ [c/d]	$f_{P04}$ [c/d]	$\Delta P$ [min]	$f_R$	$f_2$	$f_3$
31623275	1.25006	1.25015	0.085	0.00134	-	-
61449214	1.55063	1.54926	0.824	0.00134	2.19715	5.27974
66497441	2.61474	2.61200	0.577	0.00108	5.20308	1.63943
84756974	3.56606	3.56744	0.156	0.00134	-	-
113150902	0.98640	0.98957	4.670	0.00136	-	-
135081803	0.74840	0.74979	3.558	0.00134	-	-
137800207	1.66210	1.66070	0.729	0.00108	18.28538	9.82547
160644410	0.67124	0.67056	2.164	0.00134	-	-
174214184	0.93530	0.93672	2.334	0.00136	-	-
205913291	0.78349	0.78349	0.011	0.00263	-	-
212031970	1.88885	1.88747	0.556	0.00263	2.83110	3.77492*
218160121	4.56786	4.56787	0.001	0.00134	-	-
220485766	1.25492	1.25353	1.274	0.00263	1.88030	2.50844*
226037840	2.01243	2.01256	0.047	0.00263	-	-
279821618	2.18143	2.18141	0.006	0.00136	4.36144*	6.54216*
292207311	1.26267	1.26403	1.229	0.00134	-	-
293069615	0.79249	0.79523	6.261	0.00263	-	-
342829903	0.63265	0.63267	0.059	0.00134	-	-
351532879	0.48625	0.48629	0.241	0.00498	-	-
419610625	0.72033	0.71758	7.668	0.00134	-	-
444577764	1.61238	1.61160	0.431	0.00263	-	-
448876509	0.34588	0.34727	16.608	0.00134	-	-

minutes. For 17 of the targets, this difference was less than one minute, indicating good agreement between the initial and refined values. However, the remaining objects showed more significant discrepancies, with some period differences exceeding several minutes.

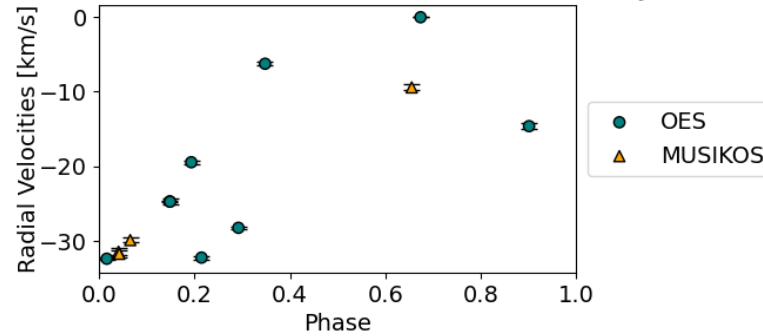
Such deviations may seem small in absolute terms, but they can have a substantial impact when interpreting the photometric and spectroscopic variability, particularly in constructing phase-folded light curves. Accurate period determination is crucial for aligning observations from different sectors and for identifying the true morphology of the variability signal. Even small errors in the period can lead to phase smearing over long baselines, causing features such as eclipses, pulsation peaks, or spot-induced modulations to appear blurred, shifted, or entirely distorted in the folded light curve and folded radial velocity curve. Figure 4.1 represents such a case, where the incorrect period estimation completely obscured the target's radial velocity curve variability.

The  $f_R$  in the Tables 4.1 and 4.2 shows the Rayleigh criterion calculated as  $2/\text{timespan}$  of the data for each object. This value defines the minimum frequency separation at which two frequency

Table 4.2: Comparison of previous ( $f_{LS}$ ) and updated ( $f_{P04}$ ) variability frequencies for stars in the northern hemisphere.  $\Delta P$  is the difference in period using these frequencies,  $f_R$  is the value of Rayleigh criterion and  $f_2$  and  $f_3$  are highest frequencies after removing the dominant frequency.

TIC	$f_{LS}$ [c/d]	$f_{P04}$ [c/d]	$\Delta P$ [min]	$f_R$	$f_2$	$f_3$
5638336	0.46870	0.46873	0.164	0.00179	-	-
12321432	0.37080	0.36983	10.193	0.07216	-	-
14400891	0.43509	0.43511	0.184	0.00179	-	-
16878120	3.18698	3.18705	0.010	0.00263	3.18775	6.37812*
21673730	0.62470	0.62331	5.156	0.00263	-	-
88815918	0.83851	0.83615	4.848	0.00246	0.83948	1.69521
184607315	0.81632	0.81365	5.783	0.07330	28.84190	12.40026
257456854	0.88783	0.88645	2.520	0.00263	-	-
302581695	0.98712	0.98566	2.156	0.07328	-	-
302666414	0.62195	0.62331	5.041	0.00261	-	-
310932102	0.76723	0.76724	0.016	0.00256	-	-
347699402	0.30223	0.30359	21.296	0.00255	-	-

TIC302666414, P=3.216d, M0=2459615.665d [HJD]



TIC302666414, P=3.209d, M0=2459615.665d [HJD]

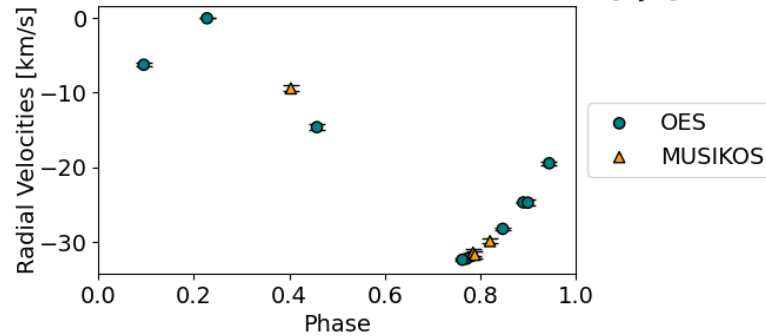


Figure 4.1: Radial velocity curves phased with twice the dominant period determined from the Lombscargle periodogram  $f_{LS}$  (top figure) and twice the period from Period04 frequencies  $f_{P04}$  (bottom figure). The periodicity of the signal disappears due to the wrong estimation of the period.

components can be distinguished in the spectrum. The last two columns of Tables 4.1 and 4.2 show the highest frequency peaks after the removal of the dominant frequency of the data. This iterative pre-whitening was carried out individually for each target. After identifying and subtracting the dominant frequency component, the residual data were re-analysed to reveal any remaining periodic signals.

The majority of the targets did not exhibit any high-frequency variations or harmonics of the dominant frequency, suggesting that the variability was dominated by a single periodic component. However, for 9 targets, additional peaks emerged in the frequency spectrum following pre-whitening. These secondary frequencies generally had much lower amplitudes than the primary signal, with the mean ratio between the dominant frequency and the highest remaining frequencies being 18.7. In some cases, these secondary peaks were identified as harmonics or linear combinations of the dominant frequency and are marked with an asterisk in Tables 4.1 and 4.2. To determine whether a frequency was a harmonic, the dominant frequency was multiplied by an integer (e.g., 2, 3), and the result was compared with the frequency obtained from the pre-whitening process. If the difference between the two values was smaller than the Rayleigh resolution limit  $f_R$  for the object, the frequency was considered a harmonic. In other cases, the peaks corresponded most likely to instrumental artefacts.

For two objects - TIC 16878120 and TIC 88815918 - the highest remaining frequency after pre-whitening was a value close to the dominant frequency  $f_{P04}$ . The difference between these two values was smaller than the Rayleigh resolution limit for each target, rendering them indistinguishable within the frequency resolution of the data. This residual signal, which remained after subtracting the dominant frequency, suggests that the primary variability was not fully removed. A likely explanation is the presence of secular changes in the period of variation—that is, gradual, long-term changes in the timing or structure of the signal. These secular variations can arise from a variety of mechanisms. In pulsating stars, they may be caused by stellar evolution processes, where changes in internal structure slowly alter the pulsation period. In binary systems, they could result from dynamic effects such as mass transfer or tidal interactions. The inability to completely eliminate the dominant frequency through pre-whitening may thus point to a non-static period, subtly shifting over time in a way that is not fully captured by a single sinusoidal model.

While the presence of these secondary peaks does not significantly affect the overall classification of variability, their identification is important for a complete characterisation of each target. Distinguishing between genuine astrophysical signals and spurious instrumental effects ensures the robustness of the frequency analysis and helps avoid misinterpretation. The rest of the data analysis uses the improved frequencies from `Period04`.

Photometric data from *TESS* combine the intrinsic flux from the target star with contributions from scattered light and other instrumental effects. These additional sources of light, often referred to as instrumental flux, can introduce artificial trends or periodicities, deforming the light curve of the observations and contributing to scatter in the phased light curves and uncertainties of frequency analysis. An incorrect data reduction process can also introduce deformities into the data and induce false signals in the frequency analysis. Therefore, a careful and consistent approach is necessary to mitigate these instrumental deformations.

In this work, we applied the detrending process partially described in Mikulášek & Zejda (2013) and adapted it to the available data using the insights and advice provided by Prof. RNDr. Zdeněk Mikulášek, CSc. The key idea behind the method is to fit a combined model that accounts for both the astrophysical signal and the instrumental distortions. The dataset was first divided into segments

based on gaps in time<sup>1</sup>; this segmentation aimed to ensure that within each group, the light curve would be relatively smooth and continuous without large observational discontinuities. Within each segment, uniform noise properties were assumed. A single weight was assigned to all data points in a given segment based on the scatter of its residuals. These weights were used to account for variations in observational noise across different portions of the dataset while maintaining internal consistency within each group.

The fitted model consisted of two main components - a harmonic component modelling the periodic signal and a polynomial (instrumental) component modelling the instrumental deformations of the data. The polynomial component was fit independently for each segment, while the harmonic signal was shared globally across the entire dataset. This ensured that the characteristics of the model harmonic (amplitude and shape) remained consistent across all segments, as physically expected.

For each segment, a polynomial model of the seventh degree was constructed using time values centred on the segment's median time. These segment-specific matrices were padded with zeros to ensure that each polynomial only affected its respective segment and were then concatenated to form a global design matrix. This allowed the instrumental trends to be fitted locally while solving a single system across the full dataset.

To determine the appropriate weighting, each segment was first fitted individually, and the scatter of the residuals was used to assign weights inversely proportional to the variance. These weights were then applied uniformly to all points within the corresponding segment. Finally, a global weighted least squares fit was performed, combining both harmonic and instrumental components into a single solution. The instrumental model was then subtracted from the observed data, yielding corrected fluxes that served as the basis for subsequent analysis. Figure 4.2 compares the original data taken from the *TESS* and detrended data obtained through the described process.

A series of figures was created to visually highlight the key characteristics of each target, providing an overview of both the photometric and spectroscopic data. These images combined data from photometric light curves from *TESS*, radial velocities, frequency spectra and information about the stars in the background of the object, as well as an approximate location of the target and its background stars on the HR diagram. Figure 4.3 shows the layout of these images.

The top-left panel of Figure 4.3 shows a cutout of the *TESS* TPF, illustrating the photometric aperture used for light curve extraction. The target star is marked with a cross, and nearby sources from the Gaia catalogue are indicated in red. The displayed `crowdsap` value quantifies the degree of contamination from neighbouring stars within the aperture. It ranges from zero to one, where a value close to one means the aperture is mostly uncontaminated, i.e., nearly all the light comes from the target star. In the bottom-left panel, a colour-magnitude diagram (CMD) displays the position of the target star—again marked with a cross—alongside the distribution of nearby Gaia sources<sup>2</sup>. This provides context for the evolutionary status of the target with respect to the local stellar population. The code used to generate these panels was adapted from [E9].

The top-middle panel shows the frequency spectrum generated by `Period04`, highlighting the dominant frequency. Continuing to the top-right, a summary box provides basic stellar parameters for the target, including the TIC identifier, the dominant photometric period, effective temperature, and apparent visual magnitude. These values were adopted from the *iTESS* Input Catalogue and supplemented by results from frequency analysis. The central panels show the phase-folded light curves at the dominant period and double the period. The grey scatter points represent phase-

<sup>1</sup>The gaps were determined in the timeseries data based on the difference between two consecutive points. The minimum value of gap size was set to 0.2 d. There were two types of data gaps: short gaps within a sector caused by the downlink of data to Earth lasting between 0.5 and 1.5 days and longer gaps between sectors.

<sup>2</sup>Gaia sources brighter than magnitude 18 were searched within a 500-arcsecond radius around the target's position.

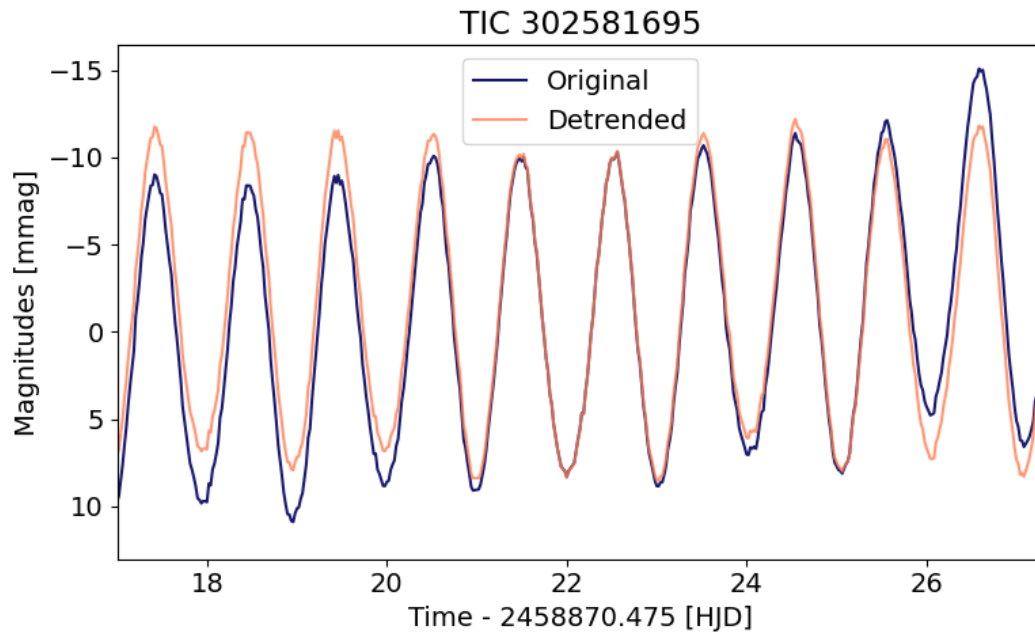


Figure 4.2: Comparison of original data and the detrended data for TIC 302581695.

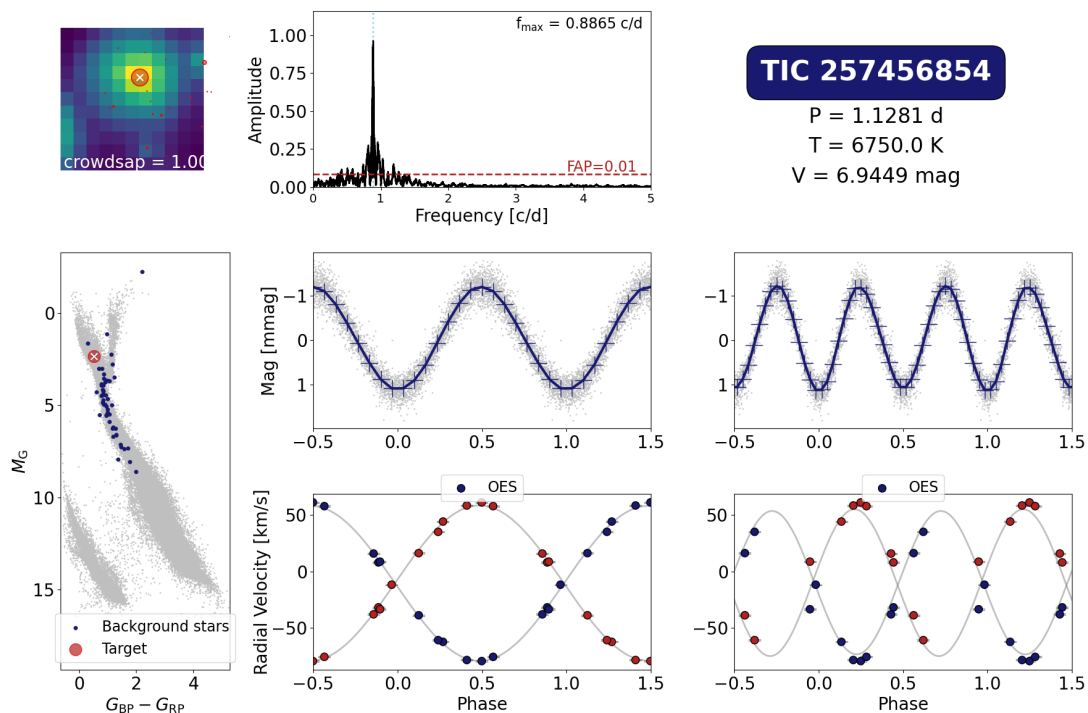


Figure 4.3: An example of the visual representation of the data for TIC 257456854.

folded photometric measurements, while the dark blue binned points highlight the shape of the phase-folded signal.

Finally, the bottom panels display radial velocity measurements folded on the same period as the photometric plots above them. The name of the spectrograph used to extract the radial velocity

measurements is indicated at the top of these plots. In Figure 4.3, two velocity curves—one for each stellar component—indicate a double-lined spectroscopic binary. Points corresponding to each component are coloured separately, while the sinusoidal curve fitted through these data only serves as the guide curve for better visualisation and is not based on stellar parameter fitting. No guide curve is plotted in the data for stars with only one component. This integrated layout enables a rapid visual assessment of each target’s variability, binarity, and photometric environment, allowing for efficient classification and identification of the mechanism responsible for the observed variations. The visualisation plots for each star are in the Appendix, shown in Figures A.1 to A.34.

The visual representations for each selected target highlighted the key features of both photometric and spectroscopic data. However, in some cases, this was insufficient to confidently determine the target’s classification. For certain objects, the radial velocity fit failed to converge due to the low signal-to-noise ratio (SNR) of the spectra. Despite this, classification was sometimes still possible based on identifiable features within the spectra themselves. To aid in this process—and as a means of cross-checking the data—additional plots were generated. These plots display all spectral observations of a given target around the  $H\alpha$  line, the most prominent spectral feature. Figure 4.4 zooms in on the region of the spectrum containing this line, showing the spectral profiles at various observation phases, phased with both the dominant period and twice the dominant period. In Figure 4.4, the spectral lines of two components move in antiphase in agreement with the radial velocity curves presented in Figure 4.3. Additional spectral plots are in the Appendix, shown in Figures A.35 to A.43.

### Classification scheme

The following sections outline the classification criteria used in this work based on data obtained from photometric and spectroscopic measurements displayed in the visual representation images. These classifications are then compared with those reported in previous publications. To determine the classification of the selected targets, each object was cross-referenced with the Simbad database (Wenger et al. 2000), which contains information on over 13 million astronomical objects [E10], including basic parameters and bibliographic references. The adopted classification scheme follows the hierarchical system proposed by Ochsenbein & Dubois (1992). Throughout the upcoming sections, we use abbreviations to indicate previously known variability types reported in the Simbad database and classes identified in this work, which are summarized in Table 4.3.

Table 4.3: Stellar classification abbreviations

Abbreviation	Class
Ell	Ellipsoidal variable
gD	$\gamma$ -Doradus pulsator
Pu	Pulsating star
SB	Spectroscopic binary
SB1	Spectroscopic binary (one component visible)
SB2	Spectroscopic binary (two components visible)
SPB	Slowly pulsating B star
V	Variable star

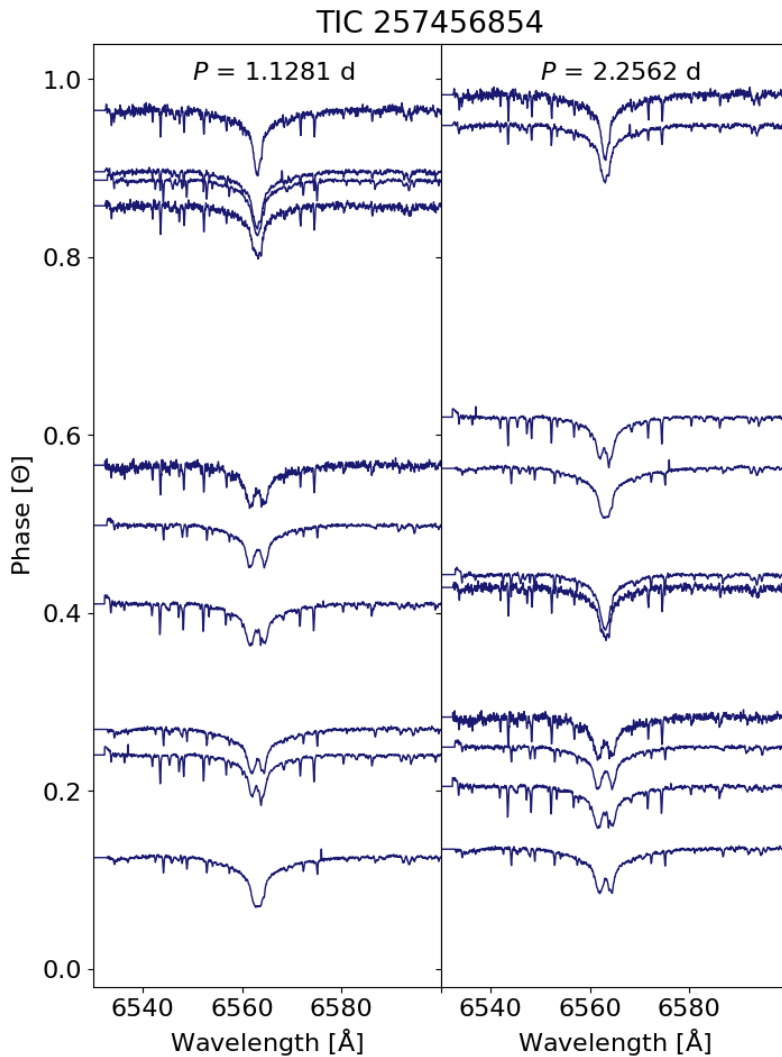


Figure 4.4: An example of the spectral line  $H\alpha$  across all observations for TIC 257456854.

## 4.1 Binary stars

Binary stars in the final sample of selected targets were identified based on the variability observed in the phase-folded radial velocity curve when folded with twice the dominant photometric period (as shown in the bottom-right panel of the visualisation figures) and aligned with the photometric light curve (middle-right panel of the visualisation figures). There were two ways of distinguishing binary stars from the stars of other classifications:

- the spectral lines of both components are visible, leading to two separate radial velocity curves in antiphase
- the phase-folded radial velocity curve showed a clear monotonic variation when phased with twice the dominant period

These two cases can be well explained by the orbital motion of the two components around the common centre of mass. The first case indicates that spectral lines from two different stars are visible simultaneously, each moving in opposite directions along the line of sight due to their

mutual orbit. The opposite values of radial velocities correspond to the Doppler shifts caused by the stars moving toward and away from the observer as they orbit their shared centre of mass. This results in two superimposed radial velocity curves, a hallmark of a double-lined spectroscopic binary (SB2).

In the second case, the photometric light curve exhibits two similar minima per cycle due to ellipsoidal variations, where tidal distortions in a close binary system cause brightness changes as the stars orbit each other. This results in a dominant photometric period that is half the true orbital period. When the radial velocity data is phase-folded with this shorter period, the monotonic variation appears weak or disappears completely. However, folding the radial velocity curve with twice the photometric period reveals a clear, well-defined sinusoidal shape consistent with orbital motion. The discrepancy between the photometric and spectroscopic periods and the emergence of a well-defined RV curve at twice the photometric period strongly support the interpretation of a binary system. In this case, only one component is visible and was marked as SB1. Deviations from the sinusoidal shape of the radial velocity curves may indicate eccentric orbits of the binary components, doppler beaming (the change in the observed flux due to the motion of the star towards or away from the observer), starspots or reflection effect (one star's light is reflected and distorted by the other star's surface) within the system.

Table 4.4 shows the binary stars in the sample of spectroscopically observed targets from the final sample of sinusoidally variable stars. These stars were classified into systems with one component visible in the spectra (SB1) and systems with both components visible (SB2). The fourth column provides the number of publications  $N$  for each object listed in Simbad. The next columns give the variability type taken from the Simbad database or other publications and the reference for the publication where the variability type was first identified.

The modelling of these binary systems is out of the scope of this work, but is considered to be performed in the future. The observed photometric variability is likely to be degenerated, resulting from a combination of effects, including ellipsoidal modulation, reflection from the companion, and Doppler beaming. These mechanisms can produce similar photometric signatures, making it difficult to disentangle their individual contributions from the light curve alone.

The final sample included 17 objects classified as binary systems—8 from the northern hemisphere and 9 from the southern hemisphere. The previous classification from Simbad was confirmed for 8 objects. One object was incorrectly classified as a pulsator in the database, while another was labelled as exhibiting both pulsations and binarity, supporting the binary interpretation. The remaining targets represent new discoveries: three single-lined spectroscopic binaries (with only one component visible in the spectra) and four double-lined spectroscopic binaries (with both components clearly visible). A detailed discussion of objects with dubious classifications or other notable peculiarities is provided below.

### **TIC 12321432**

The radial velocity curves for the object contain noisy measurements (see figure A.2); however, the spectra shown in Figure A.35 clearly show both components of the binary system, corresponding to the situation, where they are moving in antiphase when phased with twice the dominant period. Based on these spectral features, the star was classified as a double-lined spectroscopic binary (SB2).

### **TIC 14400891**

The object exhibits sinusoidal radial velocity curves in the antiphase, providing clear evidence of binarity. However, the cross-correlation function consistently revealed a third peak in the data

Table 4.4: Binary stars in the final sample

TIC	Type		N	Simbad	Simbad Reference
5638336	SB1	Fig A.1, A.35	13		
12321432	SB2	Fig A.2, A.35	12		
14400891	SB2	Fig A.3, A.35	2		
21673730	SB1	Fig A.5, A.36	16	gD	Smalley et al. (2011)
31623275	SB1	Fig A.6, A.36	6		
135081803	SB2	Fig A.12, A.37	11	SB	Gaia Collaboration (2022b)
174214184	SB2	Fig A.15, A.38	7		
212031970	SB2	Fig A.18, A.39	18	SB	Gaia Collaboration (2022b)
220485766	SB1	Fig A.20, A.39	11	Pu/SB	Gaia Collaboration (2022a,b)
257456854	SB2	Fig A.22, A.40	37	SB	Gaia Collaboration (2022b)
293069615	SB2	Fig A.25, A.41	21	SB	Gaia Collaboration (2022b)
302581695	SB1	Fig A.26, A.41	47	EII	Samus' et al. (2003)
302666414	SB1	Fig A.27, A.41	30	SB	Pourbaix et al. (2004)
342829903	SB2	Fig A.29, A.42	25	SB	Gaia Collaboration (2022b)
347699402	SB1	Fig A.30, A.42	10		
351532879	SB2	Fig A.31, A.42	31		
419610625	SB1	Fig A.32, A.42	11	SB	Gaia Collaboration (2022b)

during the fitting process. The phased radial velocities corresponding to this third component can be seen in Figure 4.5 (gray symbols), along with two curves in an antiphase. These measurements warrant further investigation, as they may indicate the presence of a third body in the system.

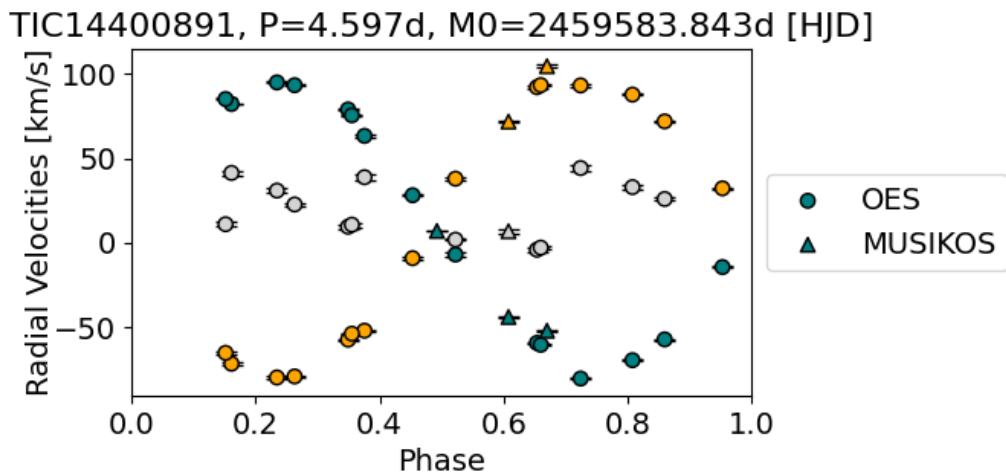


Figure 4.5: Radial velocity curve for TIC 14400891.

The radial velocities were obtained over ten months of observation. To align the most recent measurements with the sinusoidal pattern defined by earlier data, the velocities of both primary and secondary components had to be shifted by  $9\text{kms}^{-1}$  in one direction. Simultaneously, the velocities associated with the third component were shifted in the opposite direction to reduce the scatter of the points. This asymmetry further supports the hypothesis of a third body influencing the system. The spectra of the object shown in Figure A.35 display two components of the  $H\alpha$  line as the system completes its orbital motion, but for some of the spectra, the line shows three components, supporting the third body hypothesis.

### TIC 135081803

For this object, only two spectra were taken during the observations, but as can be seen in both figure A.12 and figure A.37, the lines of this object consisted of two components, clearly identifying the system as a double-lined spectroscopic binary. Let it be noted that the guide curves shown in Figure A.12 only serve as an indicator of the possible configuration for ease of visual inspection. More spectroscopic measurements are needed to constrain the orbital parameters of this system and to be able to say something about its eccentricity and configuration.

### TIC 174214184

The radial velocity measurements in Figure A.15 do not exhibit large variations. The cross-correlation function of the object displayed only one peak; however, looking at the spectra of the object, two components for the lines can be observed for three of the taken spectra, classifying the object as a double-lined spectroscopic binary.

### TIC 347699402

The radial velocity measurements for this object, shown in Figure A.30, indicate periodic variations for twice the dominant period for the object. The radial velocity curve phased with this period has a non-sinusoidal shape, indicating that the components have eccentric trajectories.

## 4.2 Pulsating variables

When a star pulsates, its outer layers periodically expand and contract in response to its pulsation mode (see Chapter 1 for more details). In the fundamental mode, the entire star contracts uniformly, decreasing its radius and increasing its effective temperature. When it again expands, the radius of the star increases and its effective temperature sharply decreases. The luminosity of the star is determined by the Stefan-Boltzmann law:

$$L = 4\pi R^2 \sigma T_{\text{eff}}^4, \quad (4.1)$$

where  $R$  is the radius of the star and  $T_{\text{eff}}$  is the effective temperature. Because  $T_{\text{eff}}$  is raised to the fourth power, its increase dominates, leading to an overall increase in  $L$ . This is why maximum brightness happens near minimum radius, when the temperature is the highest.

As the outer layers expand, the emitted light shifts toward the blue part of the spectrum. The expansion gradually slows until the star reaches its maximum radius. At this point, the outer layers momentarily come to rest relative to the observer, resulting in zero radial velocity and no Doppler shift in spectral lines. Contraction then begins, accelerating the material inward and reaching peak radial velocity halfway between the minimum and maximum radius. The motion slows again as the

cycle continues. The stellar envelope’s cyclical expansion and contraction introduce a phase shift between photometric and spectroscopic observations. The light curve and radial velocity curve are offset by a phase difference of  $\pi/4$ .

In the final sample of the stars, only one object exhibited the phase shift between its light curve and radial velocity curve phased with the dominant period of the observations. Table 4.5 shows information about the object, number of references N and the variability type denoted in the Simbad database.

Table 4.5: Pulsating objects in the final sample

TIC	Type	N	Simbad	Simbad Reference
205913291	Pu	Fig A.17, A.39	30	

The object was identified as variable during *Kepler* K2 EPIC campaign (Huber et al. 2016) and marked as such in the AAVSO International Variable Star Index (Watson et al. 2006). The underlying mechanism driving the variability was not identified during the K2 EPIC campaign.

### 4.3 Uncertain objects

The classification for some of the objects was not clear, even with the combination of photometric and spectroscopic measurements. The “unclear” tag was attributed to the objects for several different reasons:

- impossible to distinguish variability with  $P$  and  $2P$
- no variability in the radial velocity measurements, and the spread of the data across the plots was significant and could not be attributed to the noise
- not enough spectroscopic measurements
- object was a blend

Table 4.6 lists all objects with ambiguous variability due to above mentioned reasons. The columns detail the information about the number of references for these objects in the Simbad database N, previous classification and references where this classification was first identified. Each of these targets is discussed below, with arguments that explain the ambiguous classification and provide additional information about these targets.

#### TIC 16878120

Radial velocities phased with the dominant period and twice the dominant period in Figure A.4 showed no consistent variability of the spectroscopic data. The difference between the highest and lowest value of the radial velocity of this object is  $37.3\text{kms}^{-1}$ . Figure 4.6 shows the radial velocities taken for the object with time in Julian dates on the x-axis. The observations were done with an almost year-long time base and show the data in three groups around three different radial velocity values.

The spread of the data across these observations could be explained by instrumental effects - changes in observational conditions at the observing site, such as humidity, the height of the object above the horizon, and temperature. However, most of these influences are typically mitigated by the spectrograph setup and the use of correction frames. Notably, one of the spectra of TIC

Table 4.6: Uncertain objects in the final sample

TIC	Type		N	Simbad	Simbad Reference
16878120	uncertain	Fig A.4, A.35	23		
88815918	uncertain	Fig A.10, A.37	82	SB	Hoffleit & Warren (1995)
218160121	uncertain	Fig A.19, A.39	23		
292207311	uncertain	Fig A.24, A.40	16		
310932102	uncertain	Fig A.28, A.41	2		
444577764	uncertain	Fig A.33, A.43	3		
448876509	uncertain	Fig A.34, A.43	13	Pu	Gaia Collaboration (2022b)

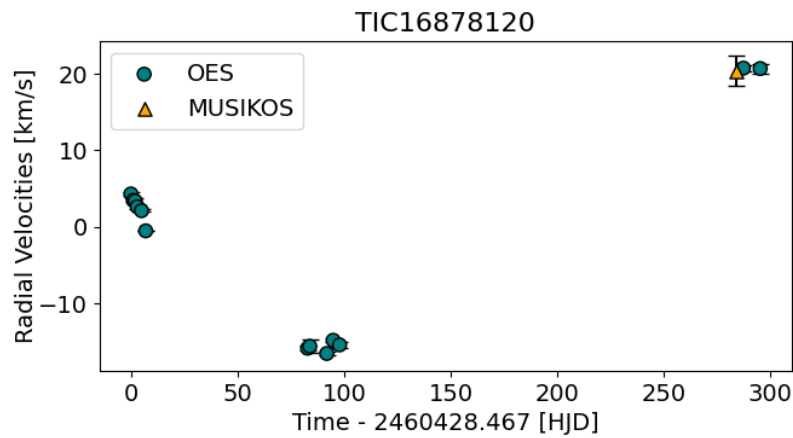


Figure 4.6: Radial velocities of TIC 16878120 plotted against the heliocentric Julian date (HJD) of observations.

16878120 was obtained using the MUSIKOS spectrograph at a completely different observatory, yet its data show good agreement with the OES observations, lending some confidence to the consistency of the measurements.

Another possible explanation is the intrinsic long-term variability of the target. However, the current dataset does not span a sufficiently long time period to support this hypothesis reliably, and eliminating this trend through fitting is impossible with the current dataset, as there are multiple solutions for the fit. Additional spectra collected over an extended time span will be necessary to determine whether the observed spread arises from instrumental effects or is inherent to the object itself.

### TIC 88815918

The classification for TIC 88815918 was impossible due to only two spectroscopic observations, as can be seen in Figure A.10. The spectra of the object had good SNR with plenty of spectral lines, but the only information that could be derived from these observations was the lack of two components shown in the lines (see Figure A.37). Therefore, it is highly likely that the object would not be a double-lined spectroscopic binary, as these observations were made near quadratures. The lack of additional data makes proper classification impossible.

### TIC 218160121

The radial velocity curve shows no variations for this object, as shown in Figure A.19. Unlike TIC 16878120, the object did not show any trends in the data when plotting the radial velocities against the date of observations. The difference between this object's highest and lowest value of radial velocities is  $14.4 \text{ km s}^{-1}$ . The frequency spectra of this object showed no other significant frequencies other than the dominant frequency. The variability of the object could possibly be revealed with more data.

### TIC 292207311

In Figure A.24, variability is evident in the radial velocity curve of the object when phased with both the dominant period and twice that period. However, based on the current dataset, it is not possible to determine which of these periodicities reflects the true variability. Notably, the radial velocity curve phased with  $2P$  lacks data between phases 0.5 and 1.0, leaving a gap that prevents a conclusive interpretation. Additional observations covering the full phase range would be necessary to resolve this ambiguity.

### TIC 310932102

TIC 310932102 shown in Figure A.28 shows very little spread of the data - the difference between the maximum and minimum of the radial velocity is  $3.1 \text{ km s}^{-1}$ . While relatively small, this variation is still larger than the typical observational uncertainties and cannot be fully attributed to noise. It is therefore possible that the object does exhibit variability that is not apparent in the current dataset and may become evident with additional observations.

### TIC 444577764

TIC 444577764 has only two observations of the radial velocities with a difference of  $15.8 \text{ km s}^{-1}$  (see Figure A.33). The object is, however, in a very crowded field with a bright star near its position (see Figure 4.7 that shows all stars brighter than 18 magnitude from the *Gaia* catalogue), and it is possible that the observed changes are intrinsic to another object. To inspect the origin of the variable signal, we constructed frequency spectra from 0 to 5 cd for each pixel of the TPF using the `plot_pixels` function in the `Lightkurve` library, as shown in Figure 4.8. The pixels highlighted in red show the pixels used for the extraction of the object light curve.

The dominant frequency of the variations identified for TIC 444577764 appears on pixels located below a bright star. This frequency is distributed across multiple pixels, suggesting that the variability likely originates from one of the brighter stars in the region. However, due to the high density of objects within each pixel, it is not possible to completely rule out the possibility that the signal is the result of a blend.

### TIC 448876509

In Figure A.34, variability is evident in the radial velocity curve of TIC 448876509 when phased with both the dominant period and twice that period. However, the current dataset does not allow us to conclusively determine which of the two reflects the true periodicity. Similar to TIC 444577764, the curve phased with  $2P$  lacks coverage between phases 0.5 and 1.0, creating a gap that hinders a definitive interpretation. Additional observations filling the gaps in the phase range would be needed to clarify the nature of the variability

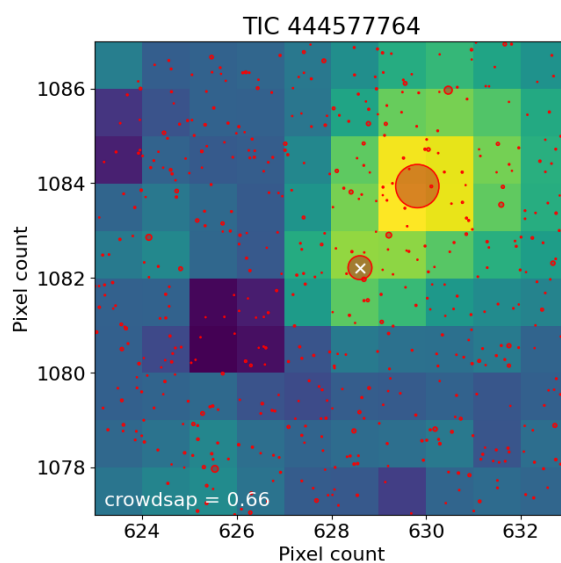


Figure 4.7: The background stars around TIC 444577764 (marked with a white cross).

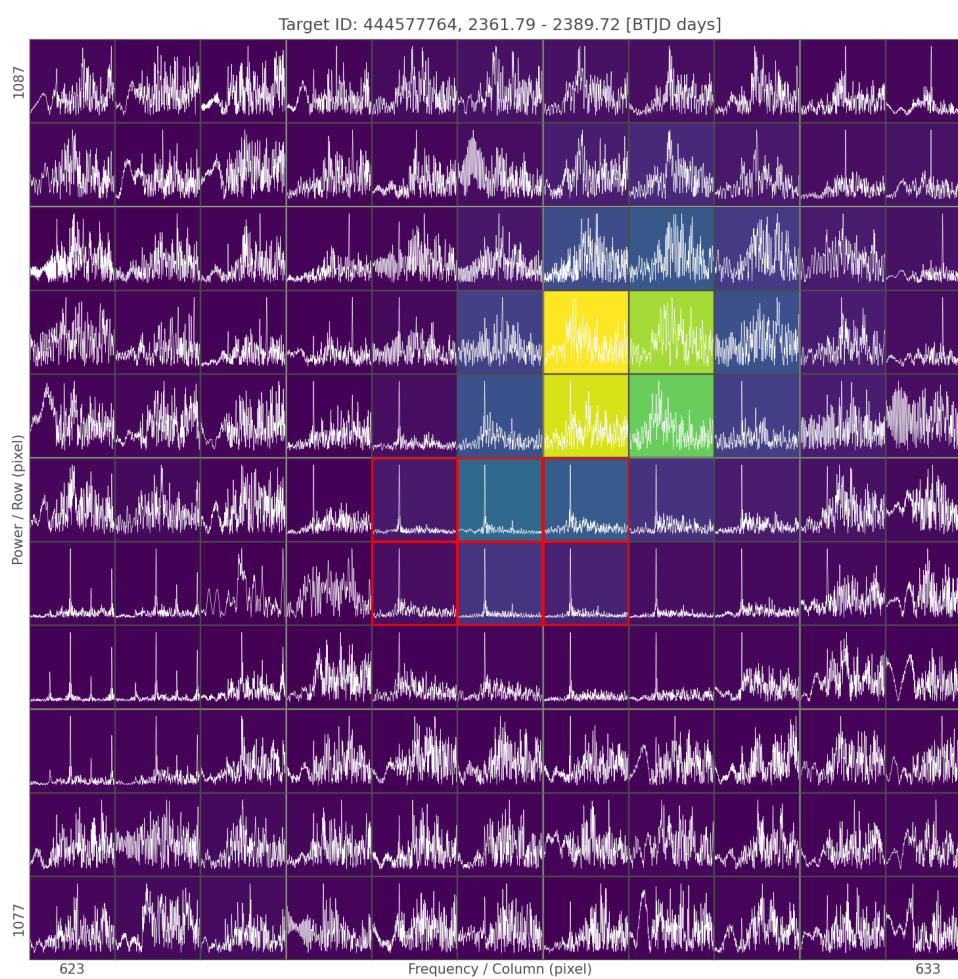


Figure 4.8: Frequency spectra for each pixel of the TPF.

## 4.4 Candidates for spotted stars

Photometric spots in the atmospheres of hot stars form when certain elements are lifted into the upper atmospheric layers and freeze there due to the influence of the star’s magnetic field. These spots often radiate differently than the surrounding photosphere, causing brightness variations on the order of millimagnitudes as the star rotates and the spots move in and out of view. This redistribution of radiation leads to different shapes of light curves in different photometric filters. Since the spots are confined to the rotating stellar atmosphere, they do not induce significant radial velocity shifts in the observed light. As they traverse the stellar disk, they may produce only minimal radial velocity variations, close to zero, due to their slight motion toward and away from the observer.

Another way to produce photometric variability on the order of millimagnitudes, while keeping radial velocity shifts very small or even negligible, is if we are observing a binary system with low inclination angles, near its pole. In this case, the light curve shows slight variations as the two components orbit each other. However, because the orbital plane is nearly perpendicular to our line of sight, the stars exhibit minimal radial motion toward or away from the observer. These two cases cannot be distinguished based on the light and radial velocity curves alone. Therefore, these objects are marked as both, and their classification remains a matter of future work.

In the final sample of the stars, these objects were identified based on the appearance of their radial velocity curves, supported by the slight deformations to the photometric light curves. The radial velocity measurements for these objects were close to zero, displaying only slight low-amplitude variations or no radial velocity shifts at all. Table 4.7 lists all objects identified as candidates for photometric spots in the final sample of stars, displaying the number of references for each object, along with any other previous classification.

Table 4.7: Candidates for spotted stars in the final sample

TIC	Type		N	Simbad	Simbad Reference
61449214	spots/binary	Fig A.7, A.36	6		
66497441	spots + SB	Fig A.8, A.36	95		
84756974	spots/binary	Fig A.9, A.37	17	Pu	Balona & Ozuyar (2020)
113150902	spots/binary	Fig A.11, A.37	14	V	Nichols et al. (2010)
137800207	spots/binary	Fig A.13, A.38	9		
160644410	spots/binary	Fig A.14, A.38	25		
184607315	spots + SB	Fig A.16, A.38	10		
226037840	spots/binary	Fig A.21, A.40	6		
279821618	spots/binary	Fig A.23, A.40	25		

Out of 34 stars with spectroscopic follow-up, 9 of them (26.5%) displayed characteristics of stars with photometric spots on their surface. All of these candidates were stars observed in the southern hemisphere, with effective temperatures above 7000 K. This is consistent with the understanding that stable photometric spots form only in the atmospheres of hot stars, where low rotation rates and stable magnetic fields in their radiative envelopes create favourable conditions for their development. However, this fact is not sufficient to confirm the spotted star hypothesis.

Confirming the presence of photometric spots on these stars lies beyond the scope of this work and will require dedicated follow-up observations and detailed analysis of spectra and elemental

abundances. High-resolution, time-resolved spectroscopy and detailed multicolour photometric monitoring are essential to distinguish spot-induced variability from other phenomena such as pulsations or binarity. Future work could focus on modelling the observed light curves and spectral line profile variations to constrain the spot properties, such as size, temperature contrast, and distribution across the stellar surface.

### TIC 66497441

TIC 66497441 showed no variations in the phased radial velocity curve (see Figure A.8). The difference between this object's highest and lowest value of radial velocities is  $30.2 \text{ km s}^{-1}$ , exhibiting a large spread of the data that cannot be attributed to noise. For this object, we constructed an unphased radial velocity plot shown in Figure 4.9, which revealed a decreasing trend in the radial velocity data taken over the span of roughly 80 days. Similarly to TIC 16878120, these variations could be attributed to the long-period orbital motion of binary stars. This long-term trend was eliminated by fitting the data with a parabolic function and subtracting the fit from the radial velocity measurements. These corrected radial velocities were phased with the dominant period of variations determined from the frequency analysis and twice this period, as can be seen in Figure 4.10. No variations were visible in the radial velocities of this object.

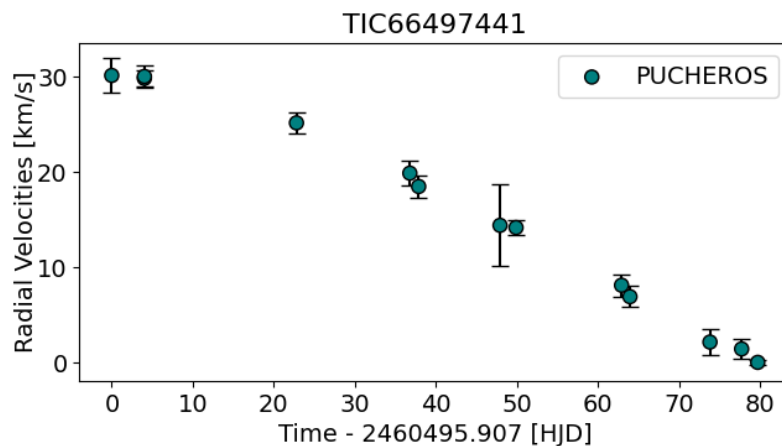


Figure 4.9: Radial velocities of TIC 66497441 plotted against the heliocentric Julian date (HJD) of observations.

### TIC 184607315

The radial velocity curve of TIC 184607315 in Figure A.16 showed no variability when phased with the dominant period or twice the dominant period. The total difference between the maximum and minimum radial velocity values is  $48.1 \text{ km s}^{-1}$ , indicating a significant spread that noise cannot explain. In Figure 4.11, the radial velocities show a decreasing trend with time, which could be explained by long-term variability caused by a binary motion with a long period. TIC 184607315 has a higher signal-to-noise ratio, resulting in better quality spectra and more reliable velocity measurements, further supporting the validity of the observed trend.

The decreasing trend was fitted by a parabolic function to eliminate the long-term variability of the object. The corrected radial velocities of the object shown in Figure 4.12 were phased with the dominant period and twice the dominant period determined from the frequency analysis, which could indicate spots on the stellar surface of one of the components, similar to TIC 66497441.

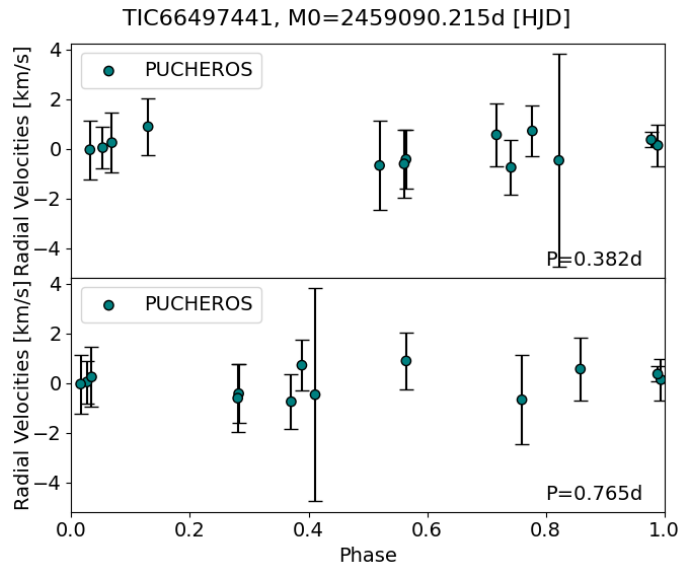


Figure 4.10: Radial velocities of TIC 66497441 after eliminating the long-term trend.

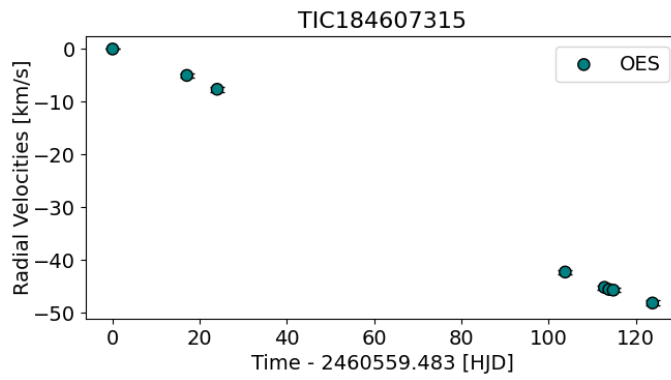


Figure 4.11: Radial velocities of TIC 184607315 plotted against the HJD of observations.

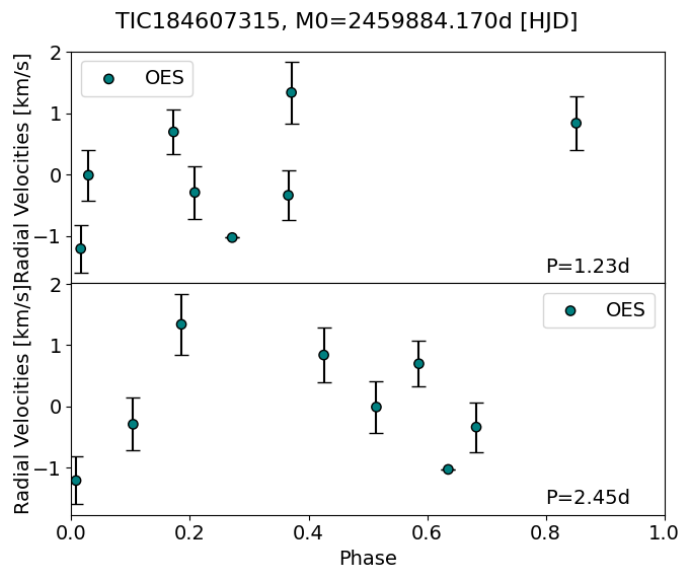


Figure 4.12: Radial velocities of TIC 184607315 after eliminating the long-term trend.

# Conclusion

The flux variations observed for stars can be explained by different mechanisms, including binarity, pulsation or stellar rotation. The aim of this work was to identify sinusoidally variable objects of O, B, A and F spectral classes from the *TESS* mission and investigate sinusoidal rotational variability of the candidates due to spots in their radiative atmospheres. The goal was also to determine the mechanisms responsible for this variability using photometric and spectroscopic observations.

This study identified 108 upper main sequence stars exhibiting sinusoidal photometric variability. Through a careful multi-step selection process described in Chapter 2, involving both automated scripts and manual inspection, the initial dataset of over 45 000 stars from the TIC was significantly reduced to include only those with clean, periodic light curves. Because of the limited observing time, the photometric data were complemented with spectroscopic observations for only 34 objects from the sample, as explained in Chapter 3. OES and MUSIKOS echelle spectrographs were used to obtain spectra for 12 targets from the northern hemisphere, and PUCHEROS+ was used for 22 targets in the southern hemisphere. The radial velocities were extracted using custom scripts in *Iraf* and aided the classification.

Photometric data of the 34 objects underwent the detrending process described in Chapter 4, along with an investigation of their frequency spectra using *Period04*. The pre-whitening procedure revealed additional signals for 9 objects from the sample shown in Tables 4.1 and 4.2, that were either harmonics of the dominant frequency, or peaks with significantly lower amplitudes that did not reveal another independent variability. For two of the objects, the dominant frequency did not disappear during the pre-whitening, hinting at secular changes to the period.

The investigated objects were classified into four categories based on the appearance of their light curves with respect to their radial velocity curves: binary stars, pulsating stars, candidates for spots and uncertain objects. According to Chini et al. (2012), the multiplicity fraction decreases with decreasing stellar mass and depends on the star's environment, being higher in clusters and associations than among field or runaway stars, although all measurements may suffer from observational biases. Duchêne & Kraus (2013) report multiplicity fractions of  $70 \pm 9\%$  for O-type stars,  $45 \pm 5\%$  for early B-type stars, and 30–45% for stars between spectral types B5 and F. Among the binary stars, ellipsoidal variables are a special class of close systems that are deformed due to the gravitational forces of their companion. Chemically peculiar (CP) stars, making up about 10% of B- to F-type stars (Hümmerich et al. 2018), feature spots that redistribute radiation, with their occurrence influenced by slow rotation (which enables atmospheric diffusion) and magnetic fields (which stabilise surface anomalies).

Out of the 34 objects, 17 (see Table 4.4) displayed variability corresponding with the binarity, either showing radial velocity curves for both components of the system or monotonic variations when phased with twice the dominant period. For 8 of these systems, binarity was already identified in the Simbad database, one object was incorrectly misclassified as a pulsating star, and for one object with ambiguous variability identified in the previous publications, this work confirms the binary hypothesis. This work discovered three new single-lined and four double-lined

spectroscopic binaries. One of the newly identified double-lined spectroscopic binaries with the designation TIC 14400891, shown in Figure A.3, is a candidate for a three-body system.

Based on the phase shift of  $\pi/4$  between its light and radial velocity curves, only one object was classified as a pulsating star. This shift occurs because the star's expanding envelope reaches maximum brightness during its greatest contraction, just before the contractions cease and the outer layers begin expanding again. Maximum radial velocities are reached approximately halfway between the star's minimum and maximum radii. TIC 205913291 can be seen in Figure A.17. This object was marked as a variable of an unknown origin in the AAVSO VSX database.

Table 4.6 lists seven objects with ambiguous variability with no clear explanation for the appearance of their photometric and spectroscopic measurements. The uncertainty of their classification arose for several reasons. Two of the objects (TIC 292207311 in Figure A.24 and TIC 448876509 in Figure A.34) showed variations when phased with both the dominant period and twice this period, with no clear way of distinguishing between the two cases. More observations filling the gaps in the phase curve could reveal the mechanism responsible for this variability. For TIC 88815918, only two observations were available, from which the classification was not possible, and more observations would be needed.

Another object (TIC 444577764 shown in Figure A.33) was identified as uncertain, due to being a blend. The object was located in a very crowded field with a very bright star blending into the aperture, as can be seen in Figure 4.7 with the image of the target star's surroundings. The final reason for assigning the uncertain variability label was the large spread of the spectroscopic data, with no clear variability in the phased radial velocity curves, that could not be attributed to noise.

Finally, the last classification category included objects that could be candidates for spot activity in their outer layers (see Table 4.7). These spots redistribute the radiation from the stellar interior, leading to different brightness variations in different photometric filters. Since the spots are confined to the rotating stellar atmosphere, they do not produce significant changes in the radial velocity curves, which helped identify these objects within the sample. Additionally, a low inclination of the binary system could also explain the absence of noticeable radial velocity variations. Determining whether the variations of these objects can be attributed to the spots or binarity could be revealed by a detailed investigation of chemical abundances, analysis of the spectra and through multicoloured photometry. However, confirming the presence of spots is beyond this thesis's scope and will be the subject of future work.

For two of these objects, TIC 66497441 and TIC 184607315 (see Figures A.8 and A.16), the spread of the data in their radial velocity curves could be explained by long-term variations due to binarity with large orbital periods. After removing this trend, the radial velocity curves showed no significant variations, leaving the origin of the short-period variability in their photometric light curves unclear. One way to explain the short-term variations in the photometric light curves is to consider spots on the stellar surfaces, but a detailed analysis of their spectral lines and chemical abundances is required to confirm this hypothesis.

In conclusion, the combination of photometric and spectroscopic analysis has led to the identification of a sample of stars exhibiting sinusoidal variability. Observations in both hemispheres led to the discovery of seven new spectroscopic binaries, one pulsating star and nine candidates for spotted stars. Overall, 50.0 % of the observed objects were binary stars, 2.9 % pulsating stars, 26.5 % were candidates for spotted stars and 20.6 % had uncertain classification. This work highlights the complexity of stellar classification and shows the need for an individual approach to variability identification, particularly in cases where photometric data alone are insufficient to determine the underlying mechanism responsible for the observed variations.

# Bibliography

- Aizenman, M. L. & Lesh, J. R. (1980), ‘Mode identification in beta cephei stars’.  
**URL:** <https://ntrs.nasa.gov/api/citations/19800016754/downloads/19800016754.pdf>
- Allen, J. S. (n.d.), ‘The classification of stellar spectra’.  
**URL:** [http://www.star.ucl.ac.uk/~pac/spectral\\_classification.html](http://www.star.ucl.ac.uk/~pac/spectral_classification.html)
- Anders, E. H. & Pedersen, M. G. (2023), ‘Convective Boundary Mixing in Main-Sequence Stars: Theory and Empirical Constraints’, *Galaxies* **11**(2), 56.
- Andrae, R. (2021), ‘Effective temperatures’.  
**URL:** [https://gea.esac.esa.int/archive/documentation/GDR2/Data\\_analysis/chap\\_cu8par/sec\\_cu8par\\_process/ssec\\_cu8par\\_process\\_priamteff.html](https://gea.esac.esa.int/archive/documentation/GDR2/Data_analysis/chap_cu8par/sec_cu8par_process/ssec_cu8par_process_priamteff.html)
- Andrae, R., Fouesneau, M., Creevey, O., Ordenovic, C., Mary, N., Burlacu, A., Chaoul, L., Jean-Antoine-Piccolo, A., Kordopatis, G., Korn, A., Lebreton, Y., Panem, C., Pichon, B., Thévenin, F., Walmsley, G. & Bailer-Jones, C. A. L. (2018), ‘Gaia Data Release 2. First stellar parameters from Apsis’, *A&A* **616**, A8.
- Balona, L. A. & Ozuyar, D. (2020), ‘Pulsation among TESS A and B stars and the Maia variables’, *MNRAS* **493**(4), 5871–5879.
- Bowman, D. M. (2017), *Amplitude Modulation of Pulsation Modes in Delta Scuti Stars*.
- Brun, A. S. & Miesch, M. S. (2008), ‘Stellar convection simulations’, *Scholarpedia*, 3(11):4278.  
**URL:** [http://www.scholarpedia.org/article/Stellar\\_convection\\_simulations](http://www.scholarpedia.org/article/Stellar_convection_simulations)
- Carroll, B. W. & Ostlie, D. A. (1996), *An Introduction to Modern Astrophysics*.
- Chaffee, Jr., F. H. & Schroeder, D. J. (1976), ‘Astronomical applications of echelle spectroscopy.’, *ARA&A* **14**, 23–42.
- Chini, R., Hoffmeister, V. H., Nasserri, A., Stahl, O. & Zinnecker, H. (2012), ‘A spectroscopic survey on the multiplicity of high-mass stars’, *MNRAS* **424**(3), 1925–1929.
- Choi, J., Dotter, A., Conroy, C., Cantiello, M., Paxton, B. & Johnson, B. D. (2016), ‘Mesa Isochrones and Stellar Tracks (MIST). I. Solar-scaled Models’, *ApJ* **823**(2), 102.
- Christensen-Dalsgaard, J. (1976), ‘On isolated stars in non-radial oscillation’, *MNRAS* **174**, 87–90.
- Christensen-Dalsgaard, J. (2002), ‘Helioseismology’, *Reviews of Modern Physics* **74**, 1073–1115.

- Debosscher, J., Blomme, J., Aerts, C. & De Ridder, J. (2011), ‘Global stellar variability study in the field-of-view of the Kepler satellite’, *A&A* **529**, A89.
- Doyle, A. C. (1890), *The Sign of the Four*, Lippincott’s Monthly Magazine.
- Doyle, A. C. (1892), *The Adventures of Sherlock Holmes - The Boscombe Valley Mystery*, George Newnes Ltd.
- Duchêne, G. & Kraus, A. (2013), ‘Stellar Multiplicity’, *ARA&A* **51**(1), 269–310.
- Eyer, L. & Mowlavi, N. (2008), Variable stars across the observational HR diagram, in ‘Journal of Physics Conference Series’, Vol. 118 of *Journal of Physics Conference Series*, IOP, p. 012010.
- Fetherolf, T., Pepper, J., Simpson, E., Kane, S. R., Močnik, T., English, J. E., Antoci, V., Huber, D., Jenkins, J. M., Stassun, K., Twicken, J. D., Vanderspek, R. & Winn, J. N. (2023), ‘Variability Catalog of Stars Observed during the TESS Prime Mission’, *ApJS* **268**(1), 4.
- Fuller, J. (2017), ‘Heartbeat stars, tidally excited oscillations and resonance locking’, *MNRAS* **472**(2), 1538–1564.
- Gaia Collaboration (2022a), ‘VizieR Online Data Catalog: Gaia DR3 Part 1. Main source (Gaia Collaboration, 2022)’, *VizieR On-line Data Catalog: I/355*. Originally published in: doi:10.1051/0004-63.
- Gaia Collaboration (2022b), ‘VizieR Online Data Catalog: Gaia DR3 Part 3. Non-single stars (Gaia Collaboration, 2022)’, *VizieR On-line Data Catalog: I/357*. Originally published in: 2023A&A...674A...1G.
- Gaia Collaboration, Eyer, L., Rimoldini, L. & et al. (2019), ‘Gaia Data Release 2. Variable stars in the colour-absolute magnitude diagram’, *A&A* **623**, A110.
- Gangestad, J. W., Henning, G. A., Persinger, R. R. & Ricker, G. R. (2013), ‘A High Earth, Lunar Resonant Orbit for Lower Cost Space Science Missions’, *arXiv e-prints* p. arXiv:1306.5333.
- Grigahcène, A., Antoci, V., Balona, L., Catanzaro, G., Daszyńska-Daszkiewicz, J., Guzik, J. A., Handler, G., Houdek, G., Kurtz, D. W., Marconi, M., Monteiro, M. J. P. F. G., Moya, A., Ripepi, V., Suárez, J.-C., Uytterhoeven, K., Borucki, W. J., Brown, T. M., Christensen-Dalsgaard, J., Gilliland, R. L., Jenkins, J. M., Kjeldsen, H., Koch, D., Bernabei, S., Bradley, P., Breger, M., Criscienzo, M. D., Dupret, M.-A., García, R. A., Hernández, A. G., Jackiewicz, J., Kaiser, A., Lehmann, H., Martín-Ruiz, S., Mathias, P., Molenda-Żakowicz, J., Nemeč, J. M., Nuspl, J., Páparó, M., Roth, M., Szabó, R., Suran, M. D. & Ventura, R. (2010), ‘Hybrid  $\gamma$  doradus– $\delta$  scuti pulsators: New insights into the physics of the oscillations from kepler observations’, *The Astrophysical Journal Letters* **713**(2), L192.  
**URL:** <https://dx.doi.org/10.1088/2041-8205/713/2/L192>
- Hoffleit, D. & Warren, Jr., W. H. (1995), ‘VizieR Online Data Catalog: Bright Star Catalogue, 5th Revised Ed. (Hoffleit+, 1991)’, *VizieR On-line Data Catalog: V/50*. Originally published in: 1964BS....C.....0H; 1991bsc..book.....H.
- Huang, C. X., Vanderburg, A., Pál, A., Sha, L., Yu, L., Fong, W., Fausnaugh, M., Shporer, A., Guerrero, N., Vanderspek, R. & Ricker, G. (2020a), ‘Photometry of 10 Million Stars from the First Two Years of TESS Full Frame Images: Part I’, *Research Notes of the American Astronomical Society* **4**(11), 204.

- Huang, C. X., Vanderburg, A., Pál, A., Sha, L., Yu, L., Fong, W., Fausnaugh, M., Shporer, A., Guerrero, N., Vanderspek, R. & Ricker, G. (2020b), ‘Photometry of 10 Million Stars from the First Two Years of TESS Full Frame Images: Part II’, *Research Notes of the American Astronomical Society* **4**(11), 206.
- Huber, D., Bryson, S. T., Haas, M. R., Barclay, T., Barentsen, G., Howell, S. B., Sharma, S., Stello, D. & Thompson, S. E. (2016), ‘The K2 Ecliptic Plane Input Catalog (EPIC) and Stellar Classifications of 138,600 Targets in Campaigns 1-8’, *ApJS* **224**(1), 2.
- Hümmerich, S., Mikulášek, Z., Paunzen, E., Bernhard, K., Janík, J., Yakunin, I. A., Pribulla, T., Vaňko, M. & Matěchová, L. (2018), ‘The Kepler view of magnetic chemically peculiar stars’, *A&A* **619**, A98.
- Kabáth, P., Skarka, M., Sabotta, S., Guenther, E., Jones, D., Klocová, T., Šubjak, J., Žák, J., Špoková, M., Blažek, M., Dvořáková, J., Dupkala, D., Fuchs, J., Hatzes, A., Kortusová, E., Novotný, R., Plávalová, E., Řezba, L., Sloup, J., Škoda, P. & Šlechta, M. (2020), ‘Ondřejov Echelle Spectrograph, Ground Based Support Facility for Exoplanet Missions’, *PASP* **132**(1009), 035002.
- Kabath, P., Vanzi, L., Hatzes, A., Guenther, E., Brahm, R., Janik, J., Minezaki, T., Skarka, M. & Karjalainen, R. (2022), PLATOSpec a new spectrograph for the PLATO targets follow-up, *in* ‘Bulletin of the American Astronomical Society’, Vol. 54, p. 102.118.
- Koubsky, P., Mayer, P., Čáp, J., Zdráský, F., Zeman, J., Pina, L. & Melich, Z. (2004), ‘Ondřejov echelle spectrograph - oes’, *Publications of the Astronomical Institute of the Czechoslovak Academy of Sciences* .
- Kraft, R. P. (1967), ‘Studies of Stellar Rotation. V. The Dependence of Rotation on Age among Solar-Type Stars’, *ApJ* **150**, 551.
- Kurtz, D. (2022), Asteroseismology across the HR diagram, *in* ‘Annual Conference and General Assembly of the’, p. 1.
- Kurtz, D. W. (2006), ‘How can we probe the interiors of stars?’.
- Lenz, P. & Breger, M. (2004), Period04: A software package to extract multiple frequencies from real data, *in* J. Zverko, J. Ziznovsky, S. J. Adelman & W. W. Weiss, eds, ‘The A-Star Puzzle’, Vol. 224 of *IAU Symposium*, pp. 786–790.
- Lenz, P. & Breger, M. (2005), ‘Period04 User Guide’, *Communications in Asteroseismology* **146**, 53–136.
- Lomb, N. R. (1976), ‘Least-Squares Frequency Analysis of Unequally Spaced Data’, *Ap&SS* **39**(2), 447–462.
- McQuillan, A., Aigrain, S. & Mazeh, T. (2013), ‘Measuring the rotation period distribution of field M dwarfs with Kepler’, *MNRAS* **432**(2), 1203–1216.
- Mikulášek, Z. (2021), *Hot Stars*, Masaryk University, Brno, Czech Republic.
- Mikulášek, Z. & Zejda, M. (2013), *Úvod do studia proměnných hvězd*, Masaryk University.
- MIT (n.d.), ‘Tess observations’. [accessed 12 March 2025].  
**URL:** <https://tess.mit.edu/observations/>

- Murphy, S. J., Hey, D., Van Reeth, T. & Bedding, T. R. (2019), ‘Gaia-derived luminosities of Kepler A/F stars and the pulsator fraction across the  $\delta$  Scuti instability strip’, *MNRAS* **485**(2), 2380–2400.
- Nichols, J. S., Henden, A. A., Huenemoerder, D. P., Lauer, J. L., Martin, E., Morgan, D. L. & Sundheim, B. A. (2010), ‘The Chandra Variable Guide Star Catalog’, *ApJS* **188**(2), 473–487.
- Nielsen, M. B., Gizon, L., Schunker, H. & Karoff, C. (2013), ‘Rotation periods of 12 000 main-sequence Kepler stars: Dependence on stellar spectral type and comparison with  $v \sin i$  observations’, *A&A* **557**, L10.
- Ochsenbein, F. & Dubois, P. (1992), Object Classification in SIMBAD, *in* A. Heck & F. Murtagh, eds, ‘European Southern Observatory Conference and Workshop Proceedings’, Vol. 43 of *European Southern Observatory Conference and Workshop Proceedings*, p. 405.
- Petrosky, E., Hwang, H.-C., Zakamska, N. L., Chandra, V. & Hill, M. J. (2021), ‘Variability, periodicity, and contact binaries in wise’, *Monthly Notices of the Royal Astronomical Society* **503**(3), 3975–3991.  
**URL:** <https://doi.org/10.1093/mnras/stab592>
- Phillips, A., Kochanek, C. S., Jayasinghe, T., Cao, L., Christy, C. T., Rowan, D. M. & Pinsonneault, M. (2024), ‘Seven classes of rotational variables from a study of 50 000 spotted stars with ASAS-SN, Gaia, and APOGEE’, *MNRAS* **527**(3), 5588–5602.
- Pourbaix, D., Tokovinin, A. A., Batten, A. H., Fekel, F. C., Hartkopf, W. I., Levato, H., Morrell, N. I., Torres, G. & Udry, S. (2004), ‘S<sub>B</sub><sup>9</sup>: The ninth catalogue of spectroscopic binary orbits’, *A&A* **424**, 727–732.
- Preston, G. W. (1974), ‘The chemically peculiar stars of the upper main sequence.’, *ARA&A* **12**, 257–277.
- Pribulla, T., Vaňko, M., Komžík, R. & Sivanič, P. (2024), ‘High-resolution échelle spectrograph at Skalnaté Pleso Observatory’, *Contributions of the Astronomical Observatory Skalnaté Pleso* **54**(2), 43–46.
- Pych, W. (2004), ‘A Fast Algorithm for Cosmic-Ray Removal from Single Images’, *PASP* **116**(816), 148–153.
- Pych, W. (2012), ‘dcr: Cosmic Ray Removal’, *Astrophysics Source Code Library*, record ascl:1207.006.
- Ricker, G. R., Winn, J. N., Vanderspek, R., Latham, D. W., Bakos, G. Á., Bean, J. L., Bert-Thompson, Z. K., Brown, T. M., Buchhave, L., Butler, N. R., Butler, R. P., Chaplin, W. J., Charbonneau, D., Christensen-Dalsgaard, J., Clampin, M., Deming, D., Doty, J., De Lee, N., Dressing, C., Dunham, E. W., Endl, M., Fressin, F., Ge, J., Henning, T., Holman, M. J., Howard, A. W., Ida, S., Jenkins, J. M., Jernigan, G., Johnson, J. A., Kaltenegger, L., Kawai, N., Kjeldsen, H., Laughlin, G., Levine, A. M., Lin, D., Lissauer, J. J., MacQueen, P., Marcy, G., McCullough, P. R., Morton, T. D., Narita, N., Paegert, M., Palle, E., Pepe, F., Pepper, J., Quirrenbach, A., Rinehart, S. A., Sasselov, D., Sato, B., Seager, S., Sozzetti, A., Stassun, K. G., Sullivan, P., Szentgyorgyi, A., Torres, G., Udry, S. & Villaseñor, J. (2015), ‘Transiting Exoplanet Survey Satellite (TESS)’, *Journal of Astronomical Telescopes, Instruments, and Systems* **1**, 014003.

- Samus', N. N., Goranskii, V. P., Durlevich, O. V., Zharova, A. V., Kazarovets, E. V., Kireeva, N. N., Pastukhova, E. N., Williams, D. B. & Hazen, M. L. (2003), 'An Electronic Version of the Second Volume of the General Catalogue of Variable Stars with Improved Coordinates', *Astronomy Letters* **29**, 468–479.
- Samus', N. N., Kazarovets, E. V., Durlevich, O. V., Kireeva, N. N. & Pastukhova, E. N. (2017), 'General catalogue of variable stars: Version GCVS 5.1', *Astronomy Reports* **61**(1), 80–88.
- Scargle, J. D. (1982), 'Studies in astronomical time series analysis. II. Statistical aspects of spectral analysis of unevenly spaced data.', *ApJ* **263**, 835–853.
- Skarka, M., Žák, J., Fedurco, M., Paunzen, E., Henzl, Z., Mašek, M., Karjalainen, R., Sanchez Arias, J. P., Sódor, Á., Auer, R. F., Kabáth, P., Karjalainen, M., Liška, J. & Štegrner, D. (2022), 'Periodic variable A-F spectral type stars in the northern TESS continuous viewing zone. I. Identification and classification', *A&A* **666**, A142.
- Smalley, B., Kurtz, D. W., Smith, A. M. S., Fossati, L., Anderson, D. R., Barros, S. C. C., Butters, O. W., Collier Cameron, A., Christian, D. J., Enoch, B., Faedi, F., Haswell, C. A., Hellier, C., Holmes, S., Horne, K., Kane, S. R., Lister, T. A., Maxted, P. F. L., Norton, A. J., Parley, N., Pollacco, D., Simpson, E. K., Skillen, I., Southworth, J., Street, R. A., West, R. G., Wheatley, P. J. & Wood, P. L. (2011), 'SuperWASP observations of pulsating Am stars', *A&A* **535**, A3.
- Soszyński, I. (n.d.), 'Ellipsoidal variables'.  
**URL:** [https://ogle.astrouw.edu.pl/atlas/ellipsoidal\\_variables.html](https://ogle.astrouw.edu.pl/atlas/ellipsoidal_variables.html)
- Strassmeier, K. G. (2009), 'Starspots', *A&A Rev.* **17**(3), 251–308.
- Tody, D. (1986), The IRAF Data Reduction and Analysis System, in D. L. Crawford, ed., 'Instrumentation in astronomy VI', Vol. 627 of *Society of Photo-Optical Instrumentation Engineers (SPIE) Conference Series*, p. 733.
- Tonry, J. & Davis, M. (1979), 'A survey of galaxy redshifts. I. Data reduction techniques.', *AJ* **84**, 1511–1525.
- Twicken, J. D., Chandrasekaran, H., Jenkins, J. M., Gunter, J. P., Girouard, F. & Klaus, T. C. (2010), Presearch data conditioning in the Kepler Science Operations Center pipeline, in N. M. Radziwill & A. Bridger, eds, 'Software and Cyberinfrastructure for Astronomy', Vol. 7740 of *Society of Photo-Optical Instrumentation Engineers (SPIE) Conference Series*, p. 77401U.
- VanderPlas, J. T. (2018), 'Understanding the Lomb-Scargle Periodogram', *ApJS* **236**(1), 16.
- Vanderspek, R., Doty, J. P., Fausnaugh, M., Villaseñor, J. N. S., Jenkins, J. M., Berta-Thompson, Z. K., Burke, C. J. & Ricker, G. R. (2018), 'TESS instrument handbook'.  
**URL:** [https://archive.stsci.edu/missions/tess/doc/TESS\\_Instrument\\_Handbook\\_v0.1.pdf](https://archive.stsci.edu/missions/tess/doc/TESS_Instrument_Handbook_v0.1.pdf)
- Vanzi, L., Chacon, J., Helminiak, K. G., Baffico, M., Rivinius, T., Štefl, S., Baade, D., Avila, G. & Guirao, C. (2012), 'PUCHEROS: a cost-effective solution for high-resolution spectroscopy with small telescopes', *MNRAS* **424**(4), 2770–2777.
- Škoda, P., Šurlan, B. & Tomić, S. (2008), Investigation of residual blaze functions in slit-based echelle spectrograph, in I. S. McLean & M. M. Casali, eds, 'Ground-based and Airborne Instrumentation for Astronomy II', Vol. 7014 of *Society of Photo-Optical Instrumentation Engineers (SPIE) Conference Series*, p. 70145X.

- Štegnér, D. (2020), ‘Spectroscopic templates for the Ondřejov échelle spectrograph’. [accessed 04 May 2025].  
**URL:** <https://astro.physics.muni.cz/download/documents/bc/bpstegner.pdf>
- Watson, C. L., Henden, A. A. & Price, A. (2006), ‘The International Variable Star Index (VSX)’, *Society for Astronomical Sciences Annual Symposium* **25**, 47.
- Wenger, M., Ochsenbein, F., Egret, D., Dubois, P., Bonnarel, F., Borde, S., Genova, F., Jasniewicz, G., Laloë, S., Lesteven, S. & Monier, R. (2000), ‘The SIMBAD astronomical database. The CDS reference database for astronomical objects’, *A&AS* **143**, 9–22.
- Wilson, R. E. (1979), ‘Eccentric orbit generalization and simultaneous solution of binary star light and velocity curves.’, *ApJ* **234**, 1054–1066.
- Wrona, M., Ratajczak, M., Kołaczek-Szymański, P. A., Kozłowski, S., Soszyński, I., Iwanek, P., Udalski, A., Szymański, M. K., Pietrukowicz, P., Skowron, D. M., Skowron, J., Mróz, P., Poleski, R., Gromadzki, M., Ulaczyk, K. & Rybicki, K. (2022), ‘The OGLE Collection of Variable Stars: One Thousand Heartbeat Stars in the Galactic Bulge and Magellanic Clouds’, *ApJS* **259**(1), 16.
- Xue, W., Niu, J.-S., Xue, H.-F. & Yin, S. (2023), ‘Pulsation Analysis of High-Amplitude  $\delta$  Scuti Stars with TESS’, *Research in Astronomy and Astrophysics* **23**(7), 075002.
- Zhabinskaya, D. (n.d.), ‘Beats’. [accessed 22 March 2025].  
**URL:** [https://phys.libretexts.org/Courses/University\\_of\\_California\\_Davis/UCD%3A\\_Physics\\_7C\\_-\\_General\\_Physics/8%3A\\_Waves/8.6%3A\\_Beats](https://phys.libretexts.org/Courses/University_of_California_Davis/UCD%3A_Physics_7C_-_General_Physics/8%3A_Waves/8.6%3A_Beats)

## Electronic sources

- [E1] accessed 24 January 2025, <https://sites.uni.edu/morgans/astro/course/Notes/section2/spectraltypes.html>
- [E2] accessed 28 January 2025, <https://cdsarc.u-strasbg.fr/afoev/var/eacvn.htx>
- [E3] accessed 13 March 2025,  
<https://mast.stsci.edu/portal/Mashup/Clients/Mast/Portal.html>
- [E4] accessed 14 March 2025,  
[https://sites.uni.edu/morgans/astro/course/Notes/section2/spectraltemps.html?fbclid=IwY2xjawJBPw1leHRuA2FlbQIxMAABHU10VYalo6\\_z\\_WSF-2EdpS7L3bBPnwtzkR8izaSuRcDLVo-vHZr5gimgmA\\_aem\\_2T83WbU91z5aVPhg5m3CgA](https://sites.uni.edu/morgans/astro/course/Notes/section2/spectraltemps.html?fbclid=IwY2xjawJBPw1leHRuA2FlbQIxMAABHU10VYalo6_z_WSF-2EdpS7L3bBPnwtzkR8izaSuRcDLVo-vHZr5gimgmA_aem_2T83WbU91z5aVPhg5m3CgA)
- [E5] accessed 29 March 2025,  
<https://www.astro.sk/en/research/observatories/skalnate-pleso-observatory/>
- [E6] accessed 29 March 2025, <https://stel.asu.cas.cz/plato/spectrograph.html>
- [E7] accessed 29 March 2025,  
<https://www.eso.org/public/teles-instr/lasilla/152metre/>
- [E8] accessed 13 April 2025, <https://heasarc.gsfc.nasa.gov/docs/tess/sector.html>
- [E9] accessed 13 April 2025, <https://github.com/ipelisolli/TESS-LS>
- [E10] accessed 14 April 2025, <https://simbad.u-strasbg.fr/Pages/guide/ch15.htx>



# Appendix

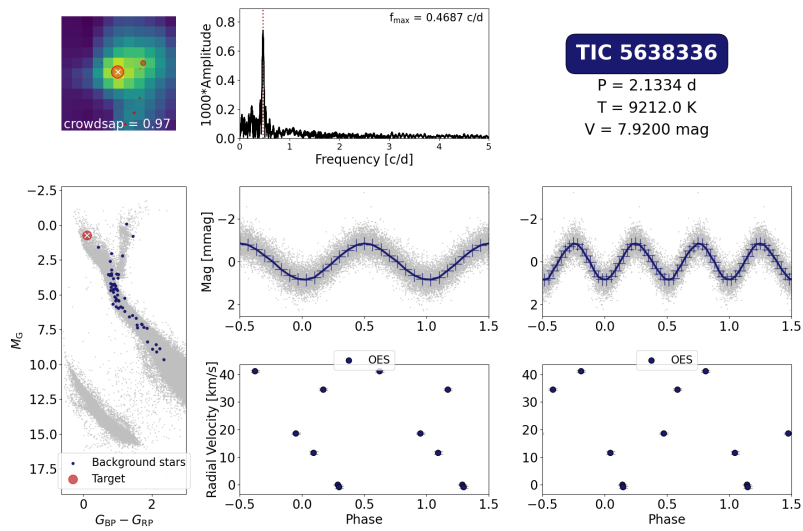


Figure A.1: Visualisation plot - TIC 5638336 (SB1).

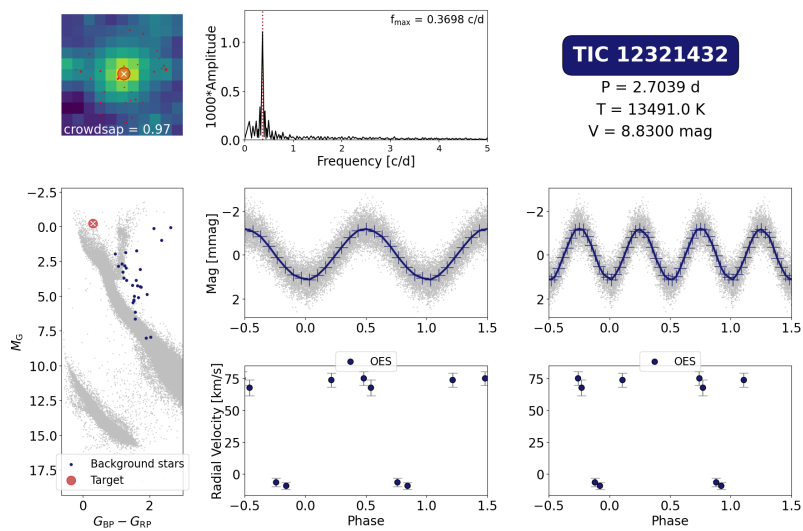


Figure A.2: Visualisation plot - TIC 12321432 (SB2).

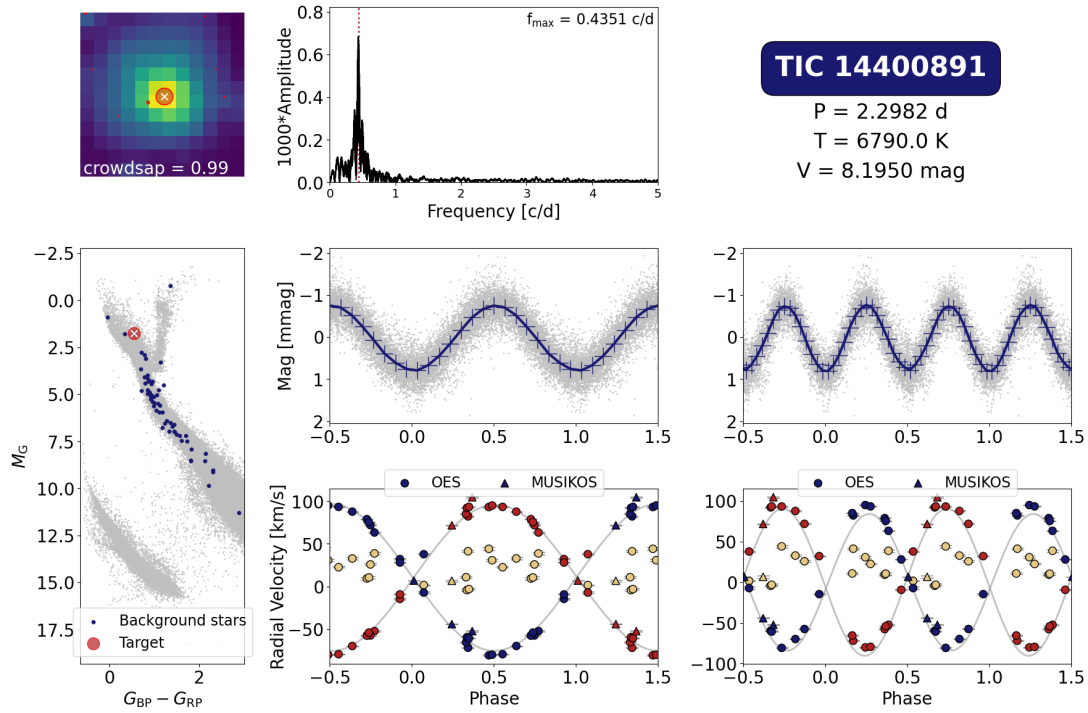


Figure A.3: Visualisation plot - TIC 14400891 (SB2).

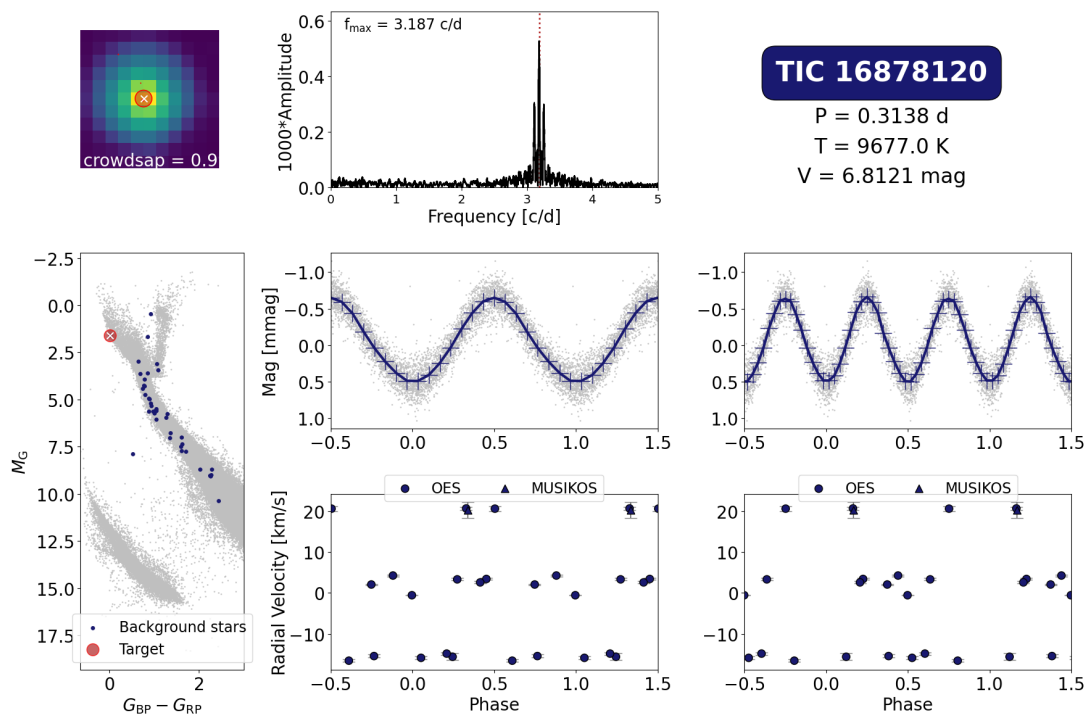


Figure A.4: Visualisation plot - TIC 16878120 (uncertain).

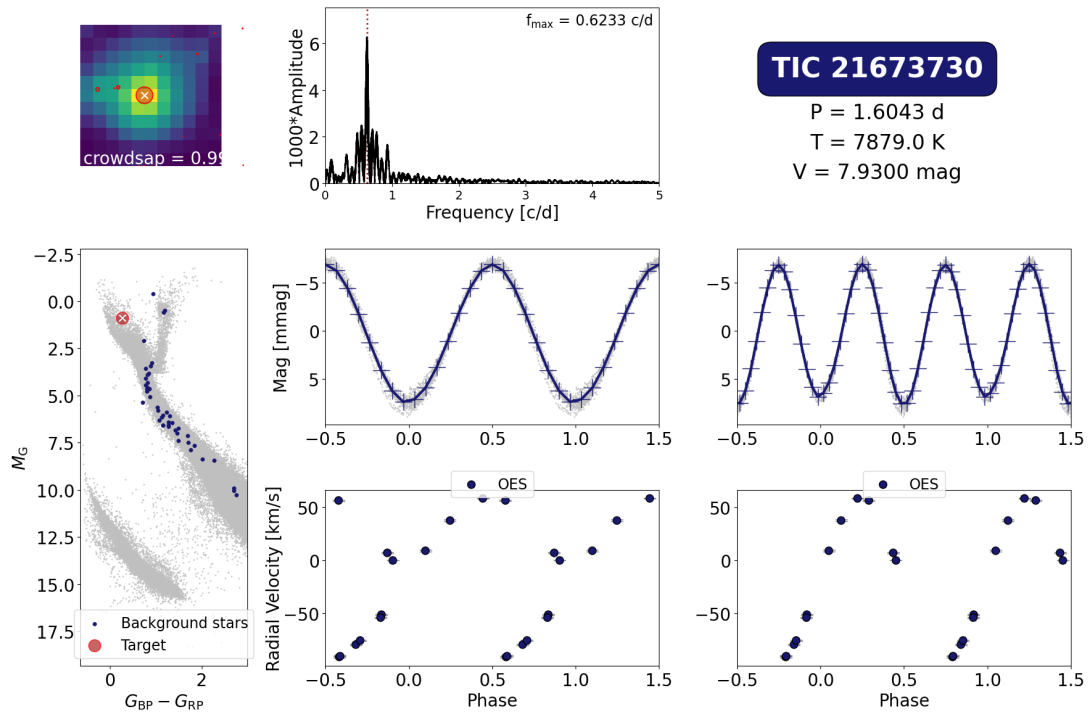


Figure A.5: Visualisation plot - TIC 21673730 (SB1).

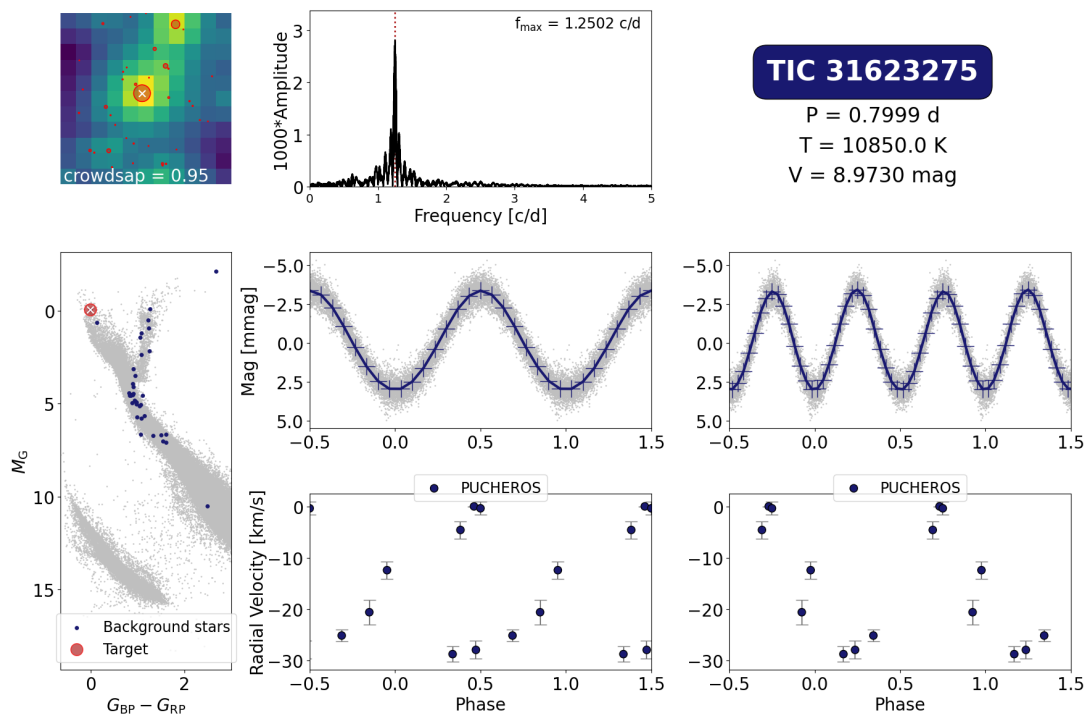


Figure A.6: Visualisation plot - TIC 31623275 (SB1).

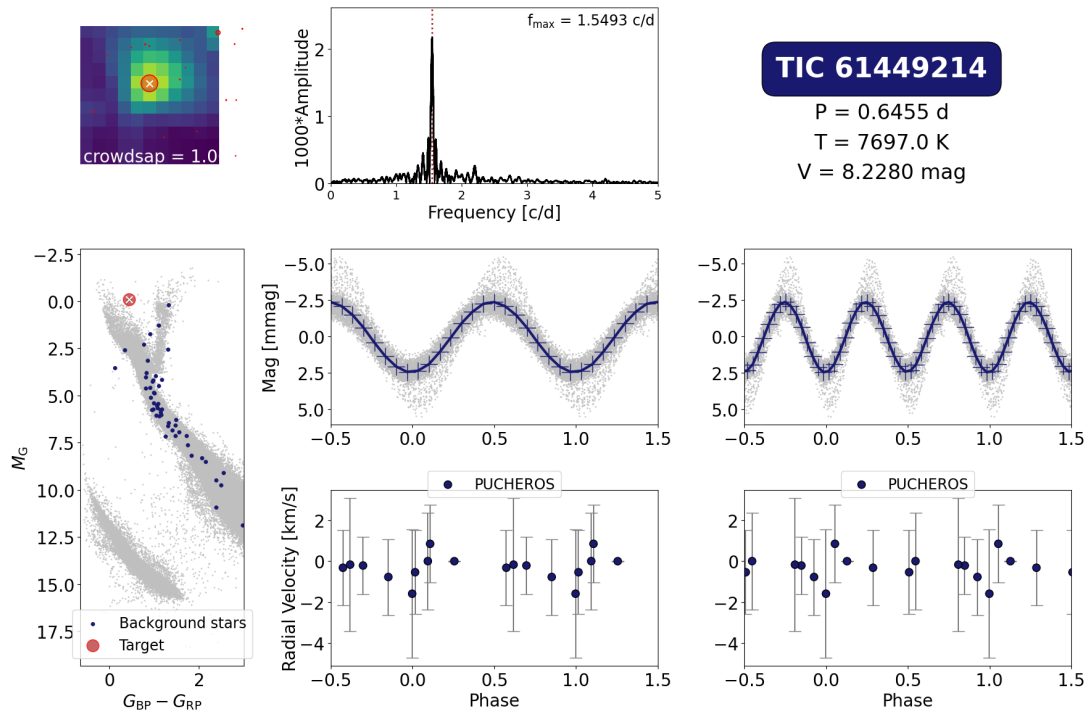


Figure A.7: Visualisation plot - TIC 61449214 (spots/binary).

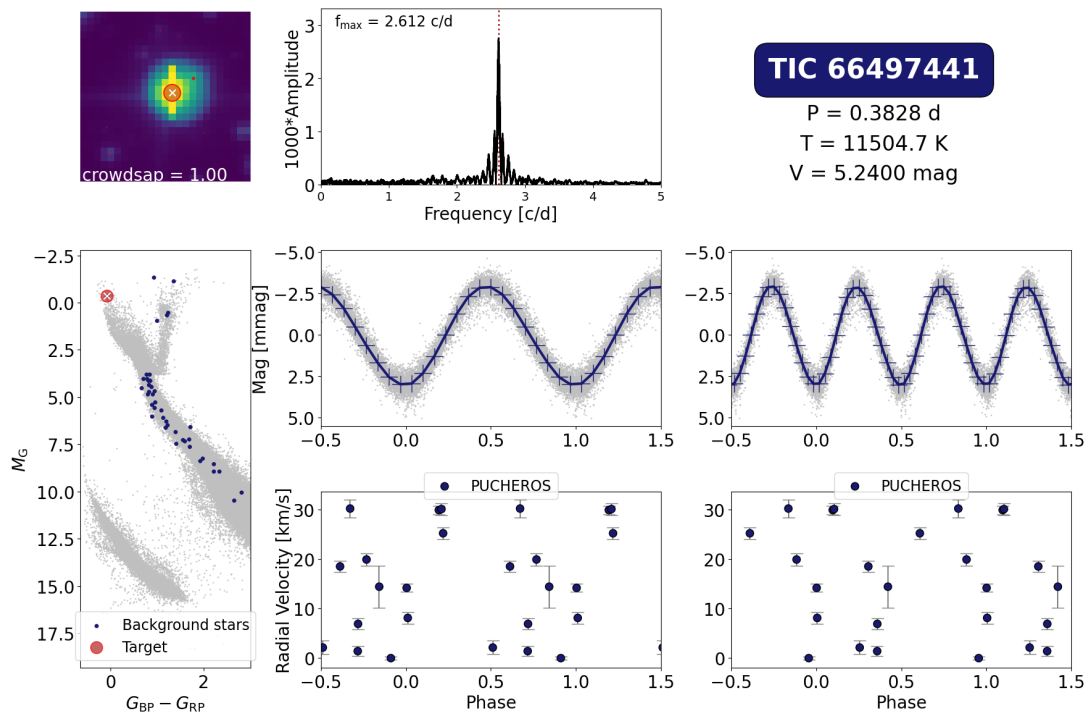


Figure A.8: Visualisation plot - TIC 66497441 (spots + SB).

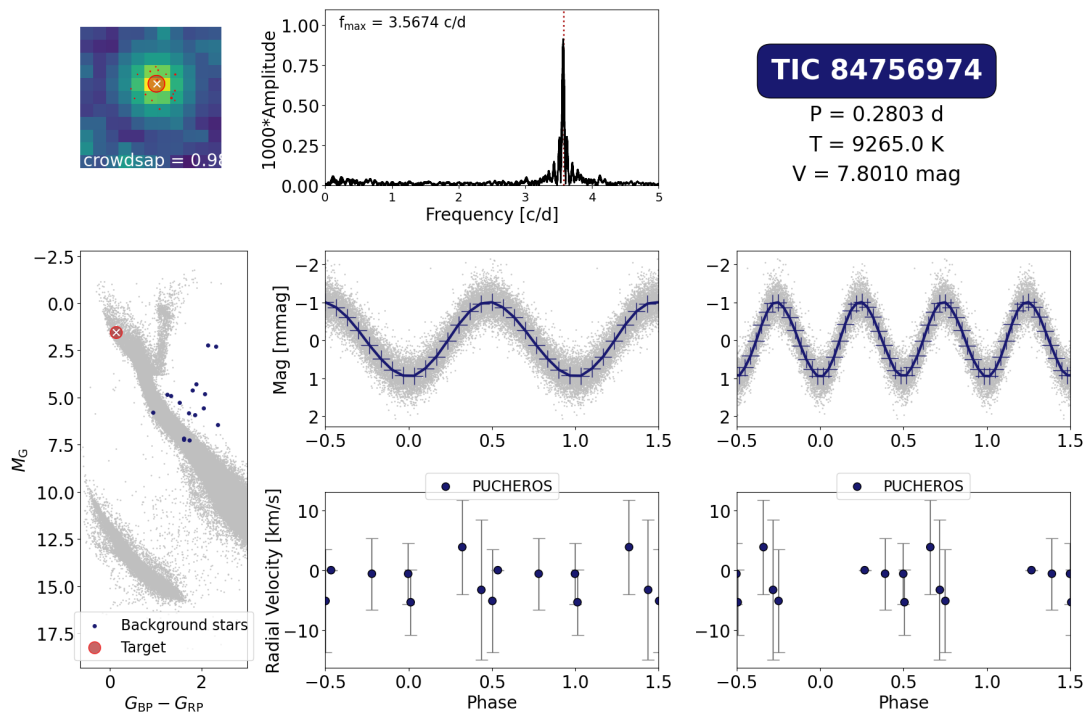


Figure A.9: Visualisation plot - TIC 84756974 (spots/binary).

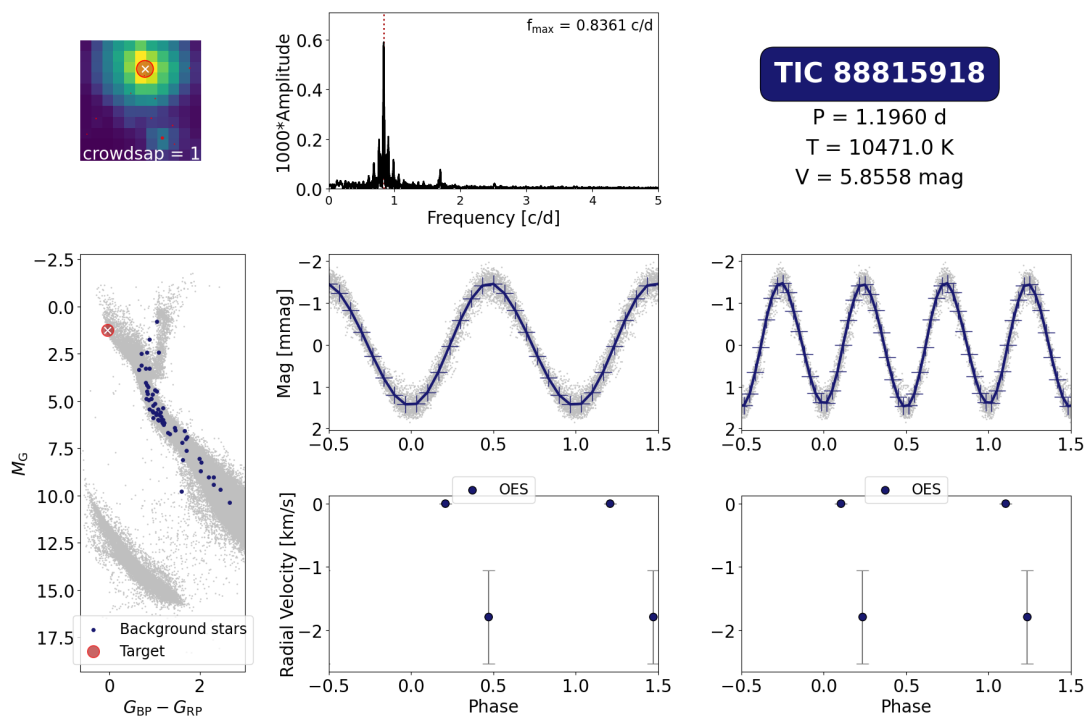


Figure A.10: Visualisation plot - TIC 88815918 (uncertain).

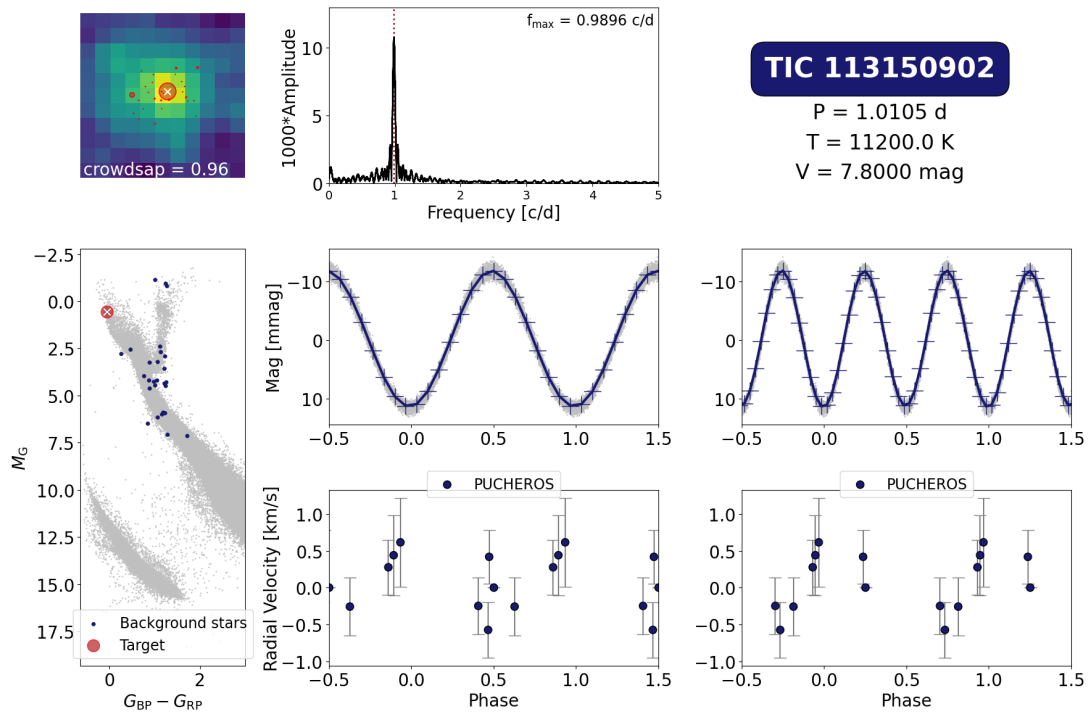


Figure A.11: Visualisation plot - TIC 113150902 (spots/binary).

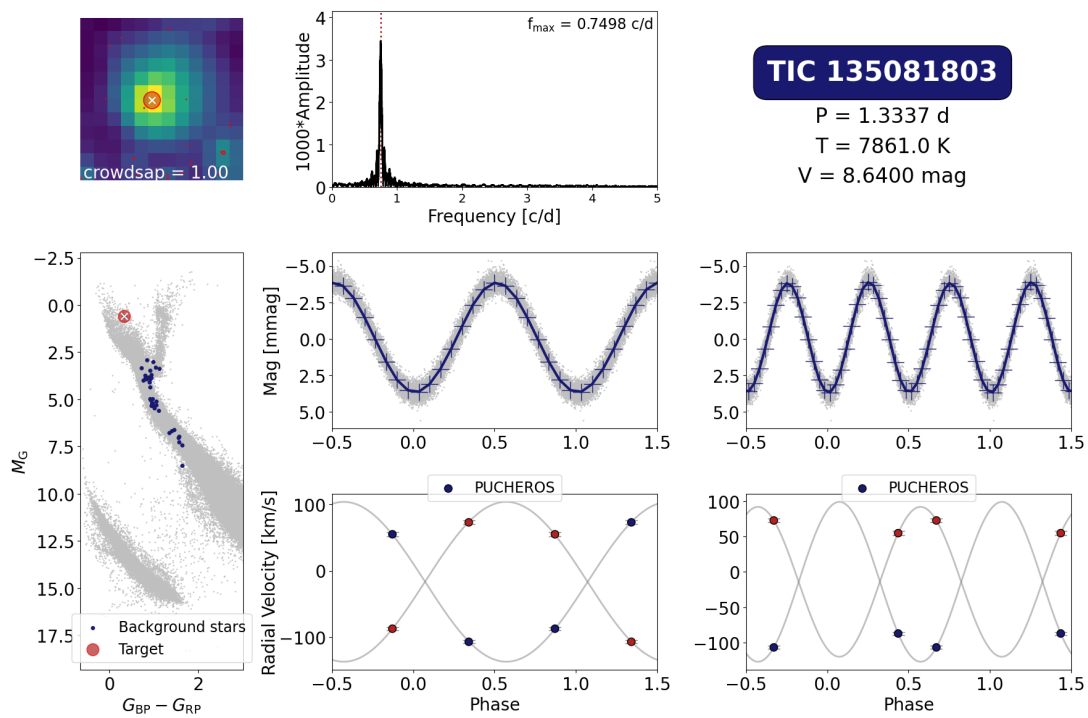


Figure A.12: Visualisation plot - TIC 135081803 (SB2).

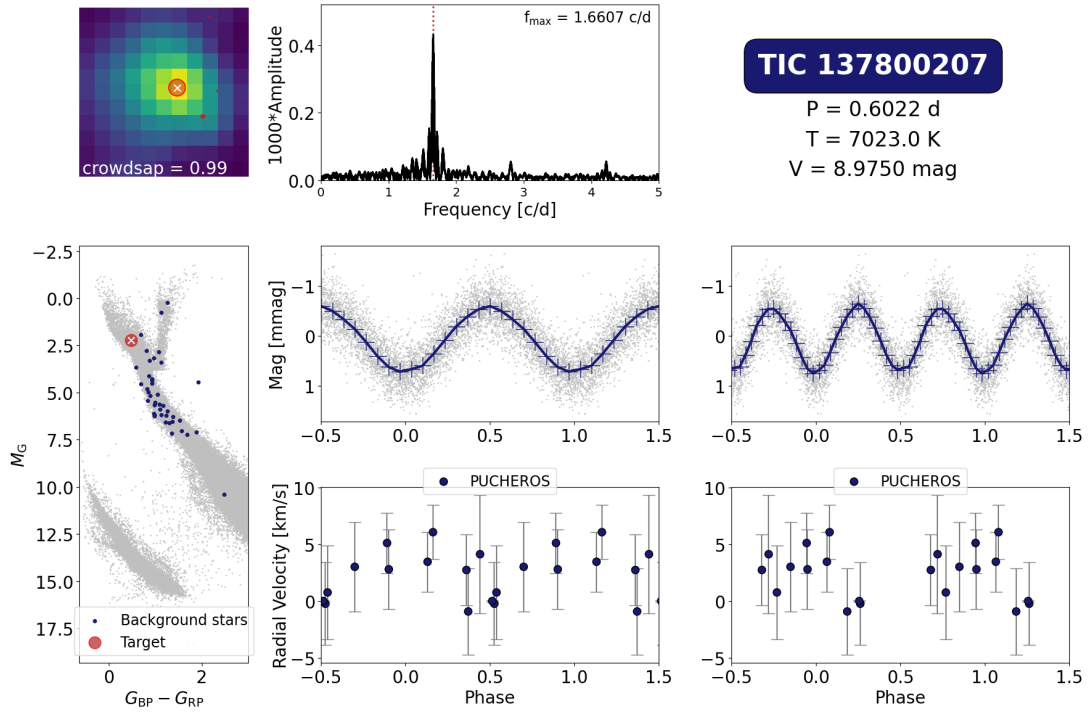


Figure A.13: Visualisation plot - TIC 137800207 (spots/binary).

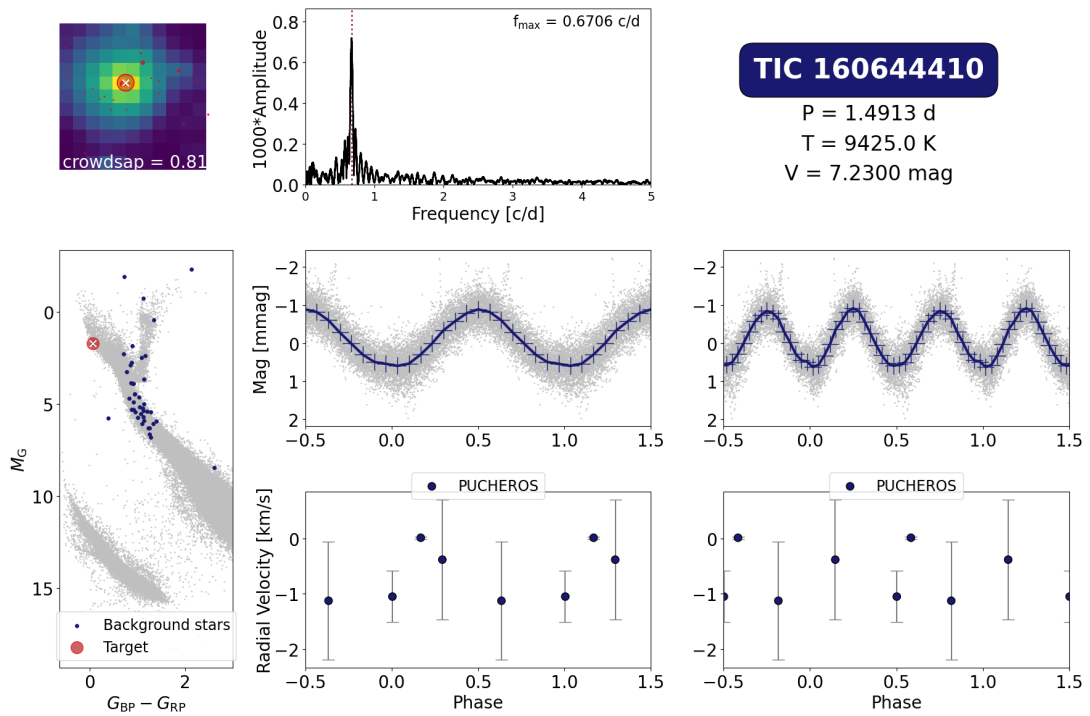


Figure A.14: Visualisation plot - TIC 160644410 (spots/binary).

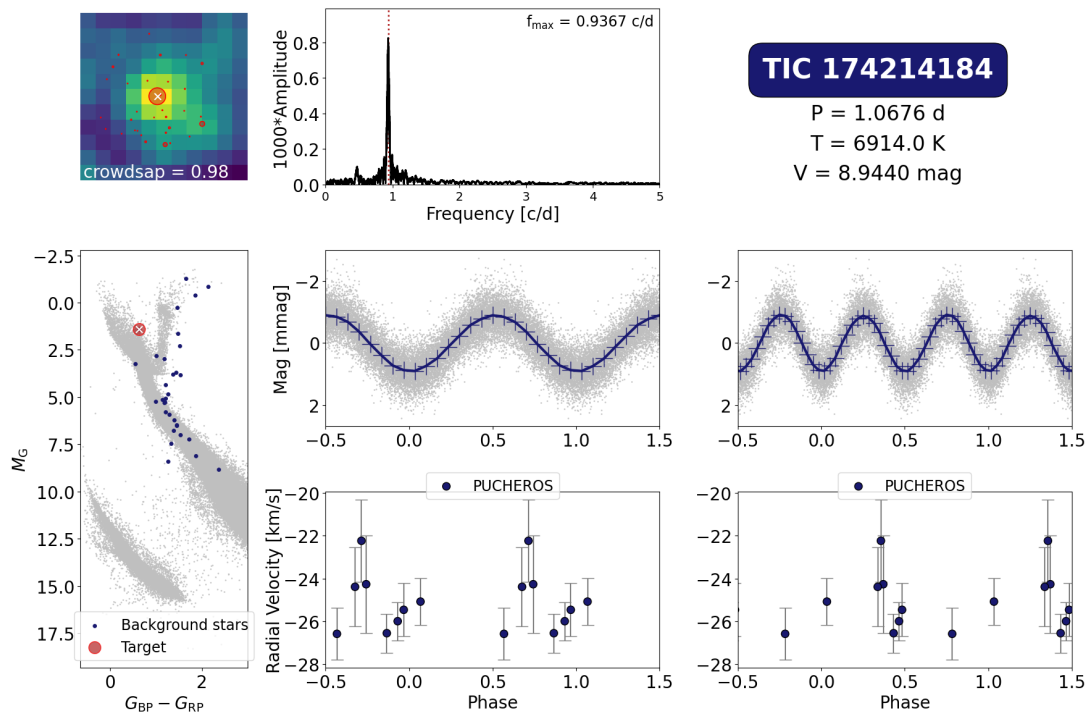


Figure A.15: Visualisation plot - TIC 174214184 (SB2).

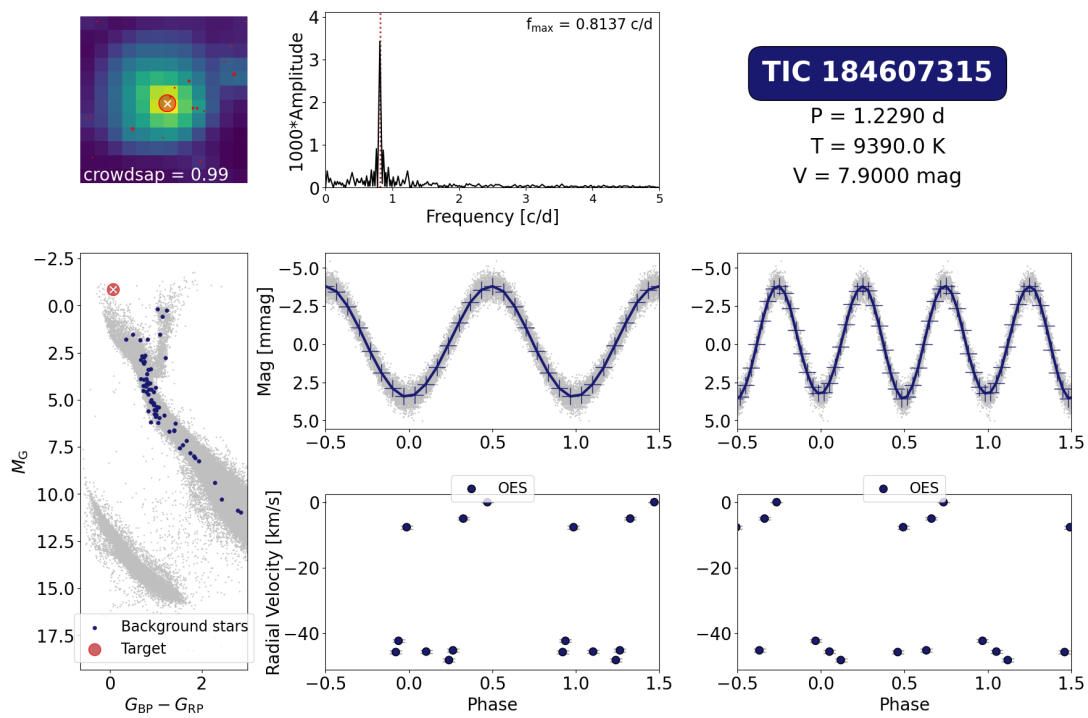


Figure A.16: Visualisation plot - TIC 184607315 (spots + SB).

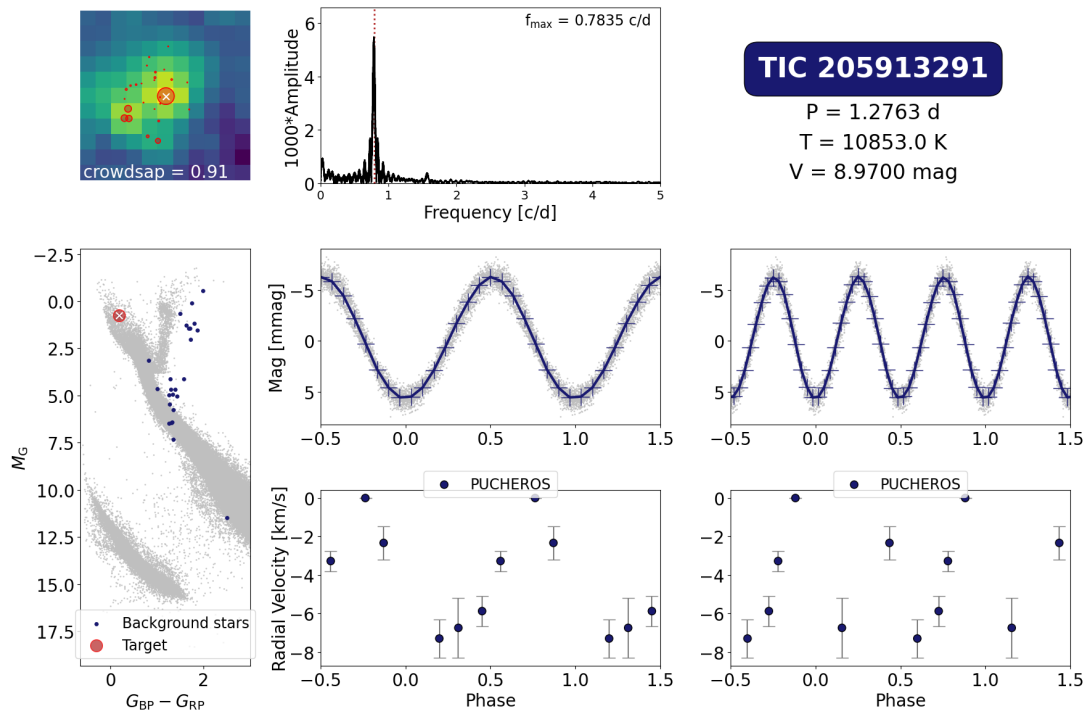


Figure A.17: Visualisation plot - TIC 205913291 (Pu).

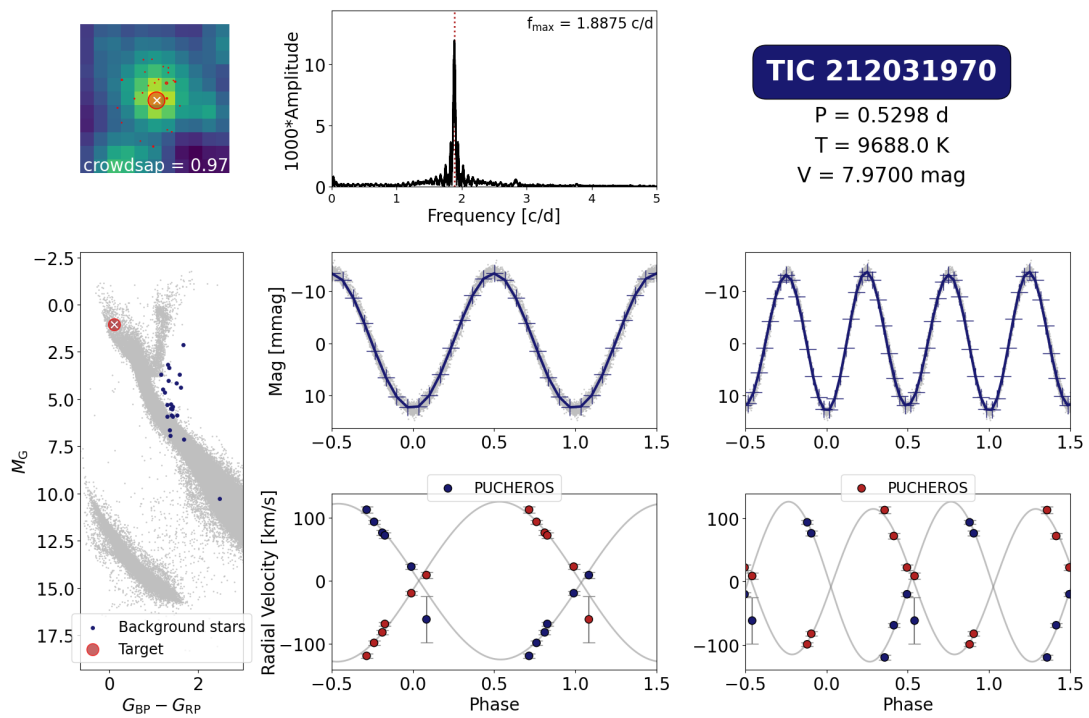


Figure A.18: Visualisation plot - TIC 212031970 (SB2).

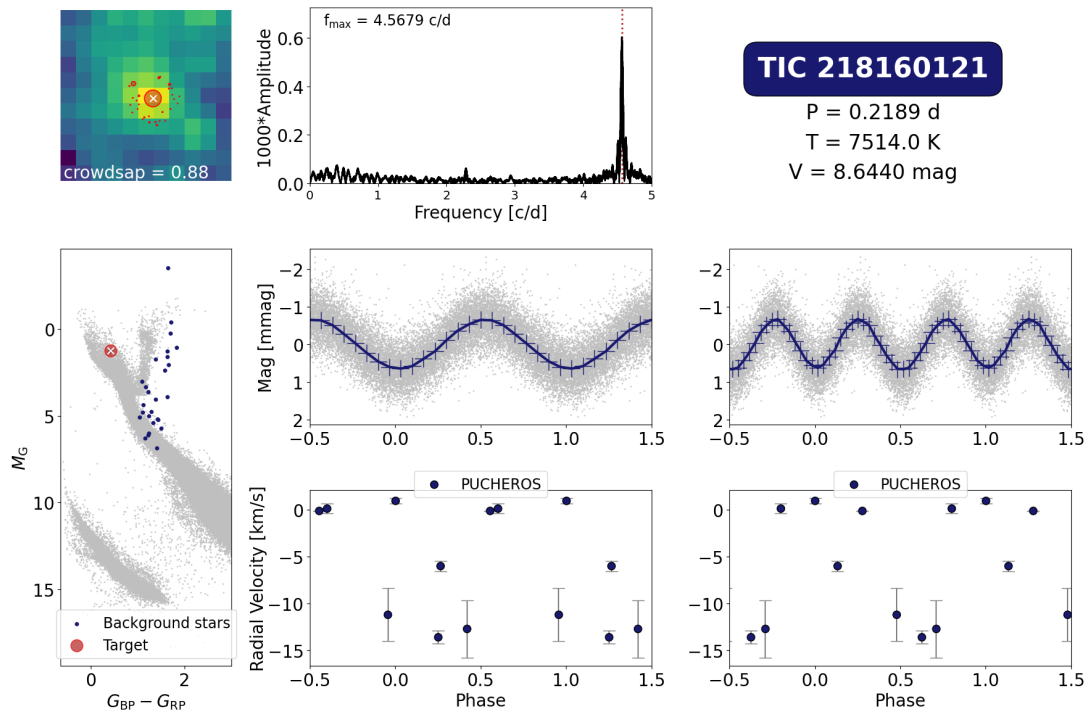


Figure A.19: Visualisation plot - TIC 218160121 (uncertain).

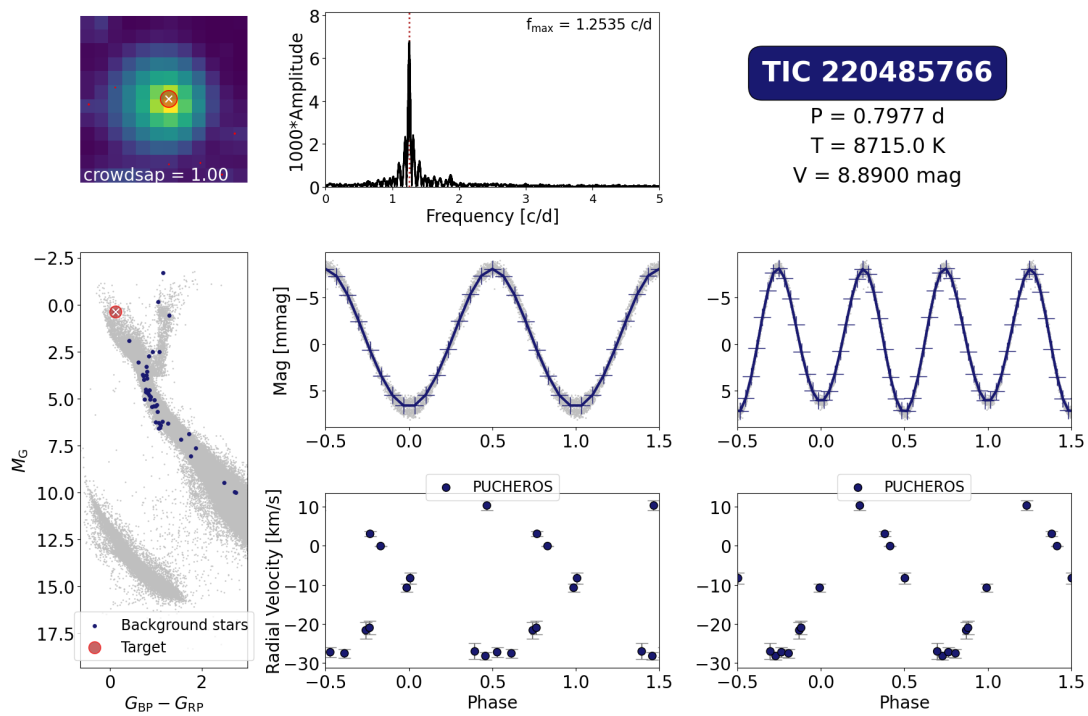


Figure A.20: Visualisation plot - TIC 220485766 (SB1).

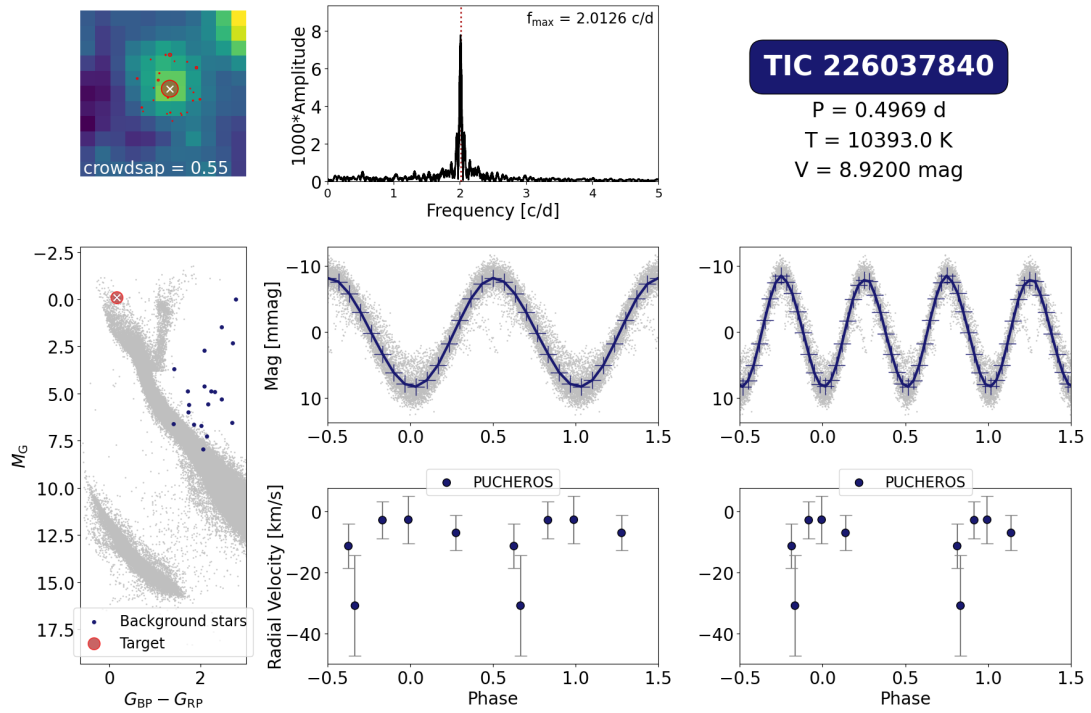


Figure A.21: Visualisation plot - TIC 226037840 (spots/binary).

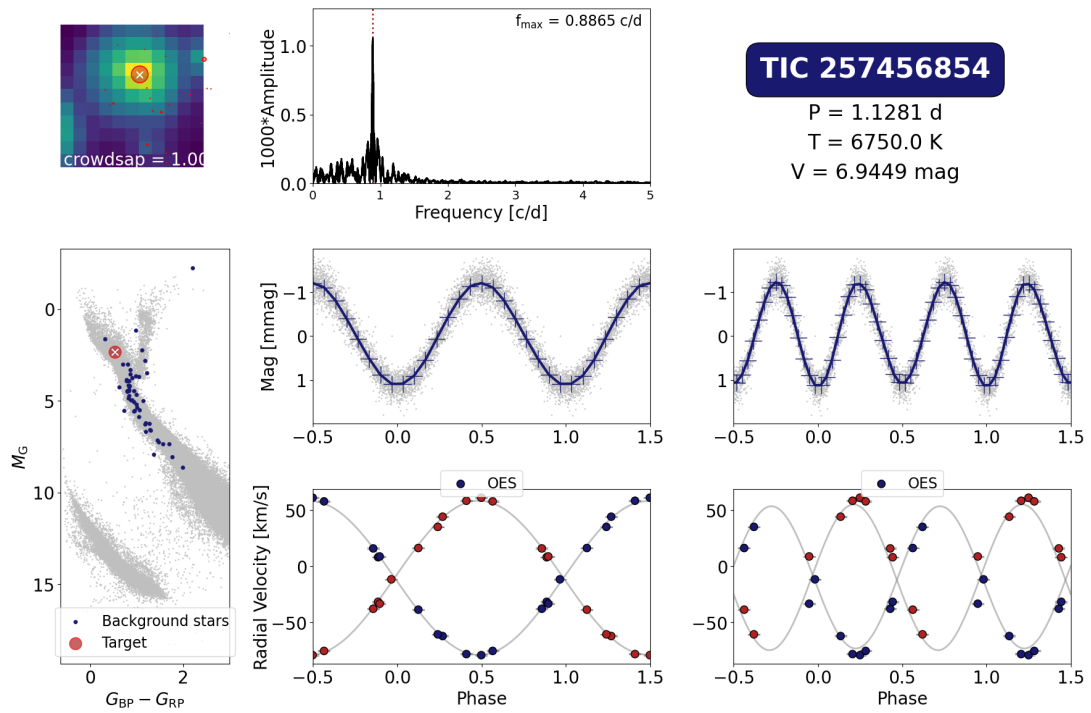


Figure A.22: Visualisation plot - TIC 257456854 (SB2).

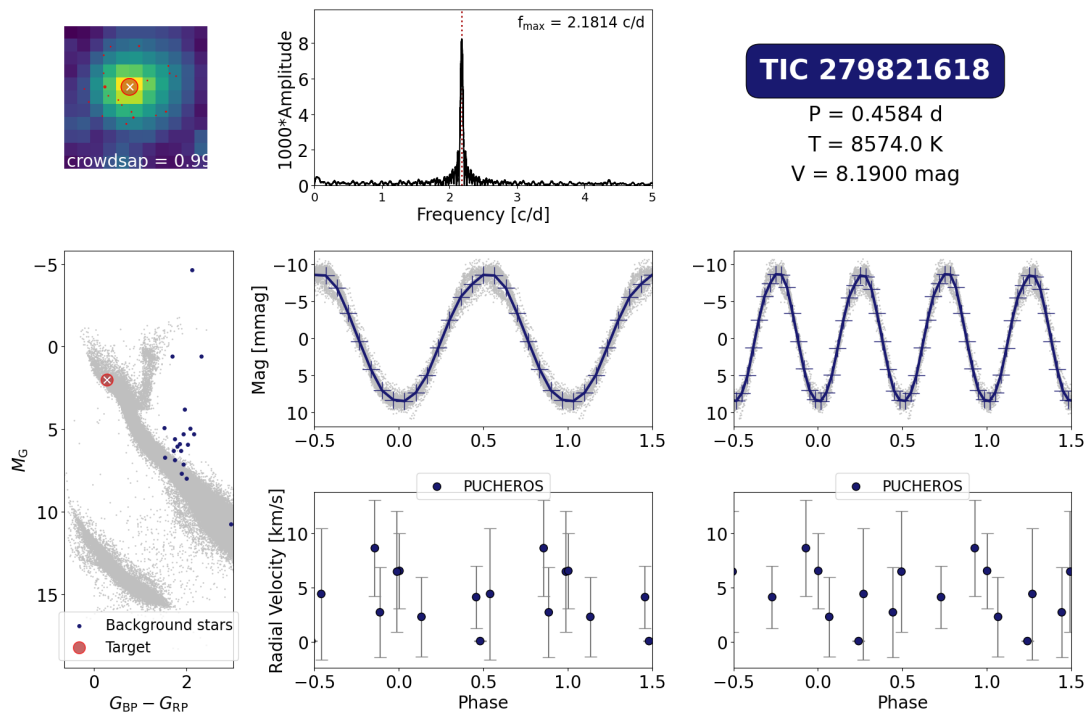


Figure A.23: Visualisation plot - TIC 279821618 (spots/binary).

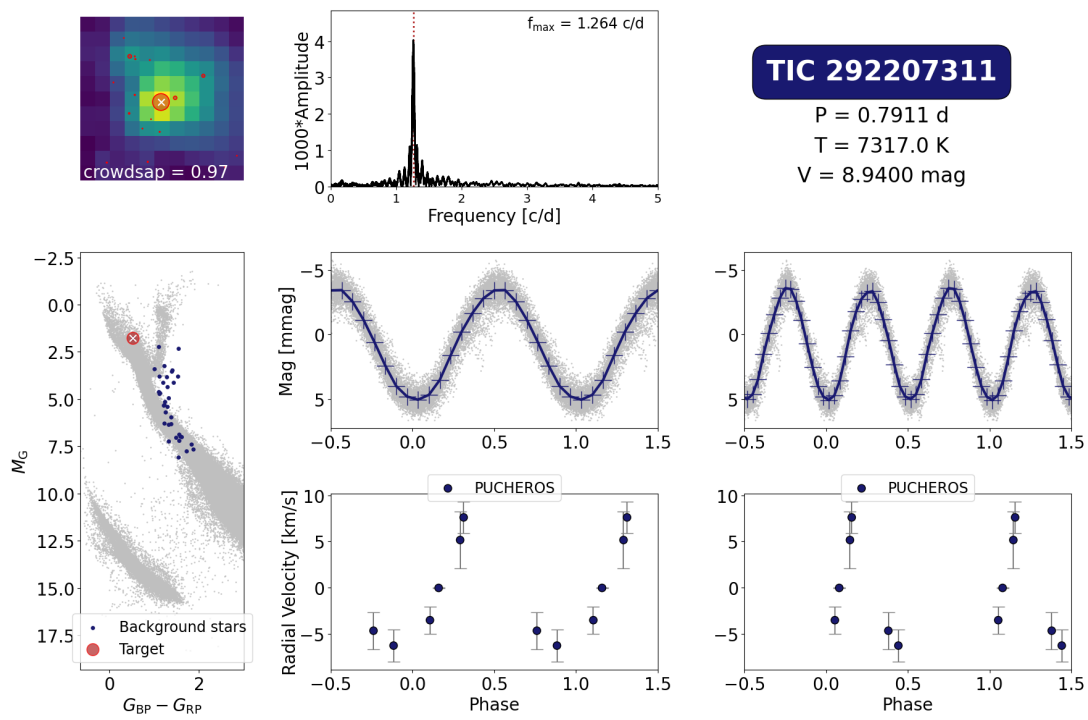


Figure A.24: Visualisation plot - TIC 292207311 (uncertain).

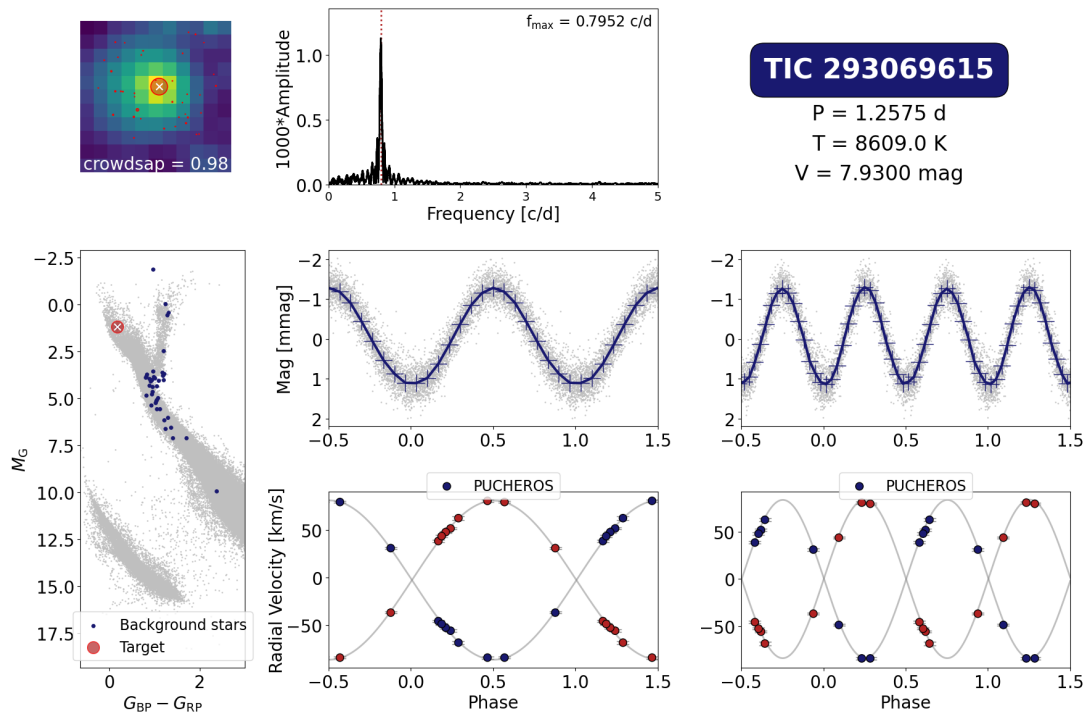


Figure A.25: Visualisation plot - TIC 293069615 (SB2).

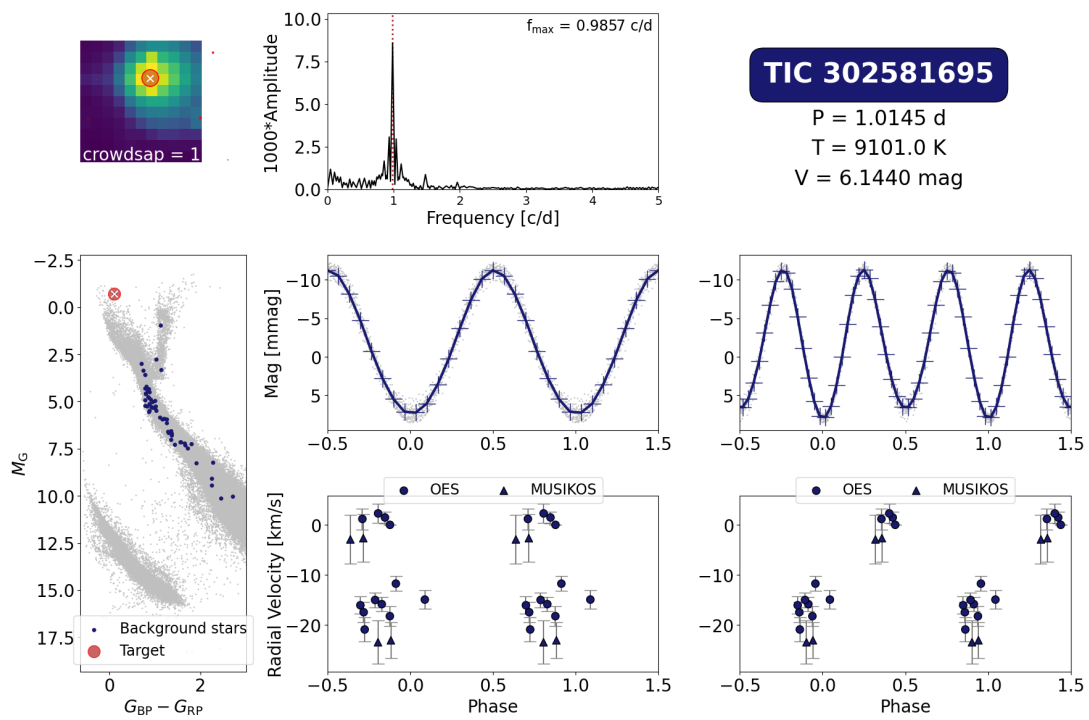


Figure A.26: Visualisation plot - TIC 302581695 (SB1).

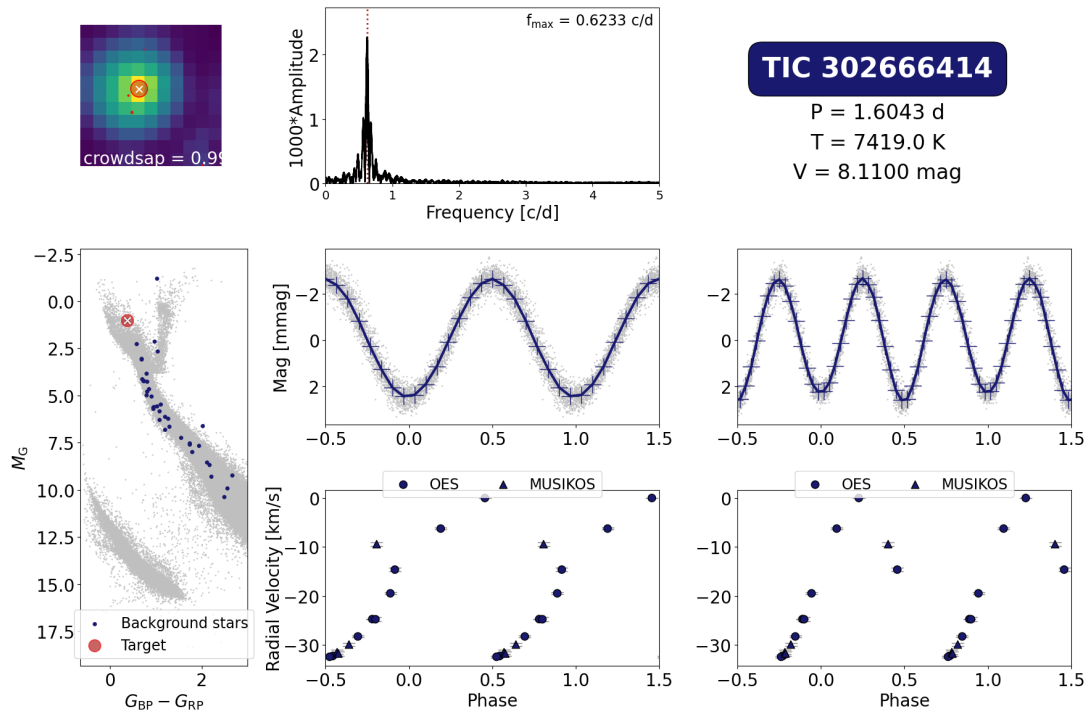


Figure A.27: Visualisation plot - TIC 302666414 (SB1).

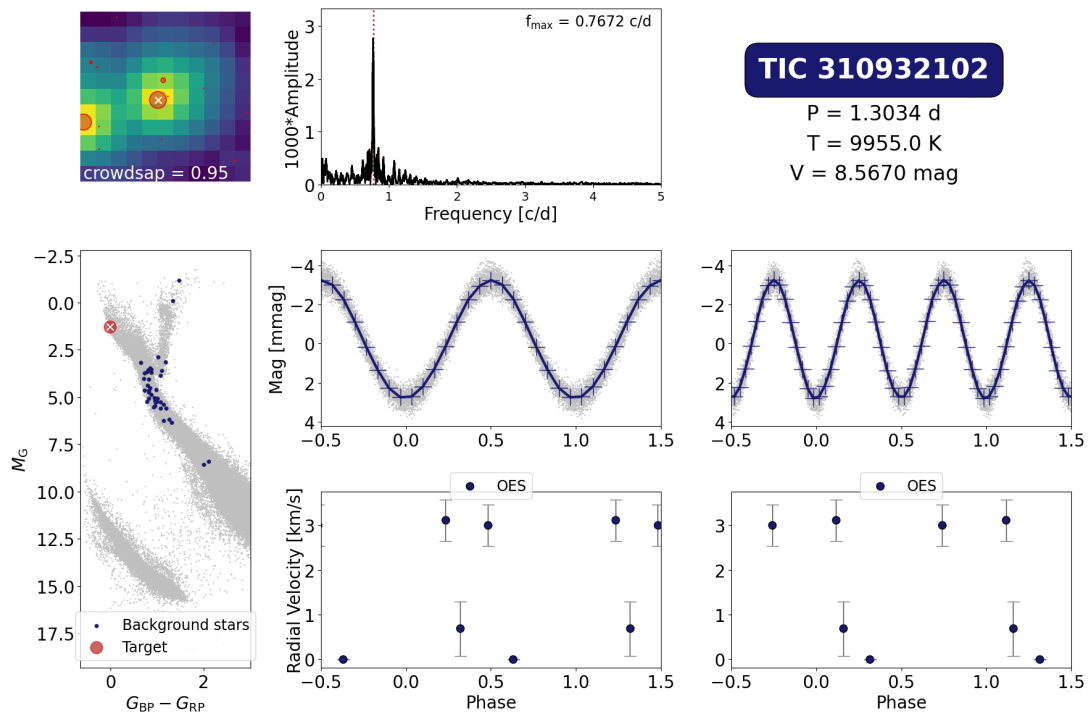


Figure A.28: Visualisation plot - TIC 310932102 (uncertain).

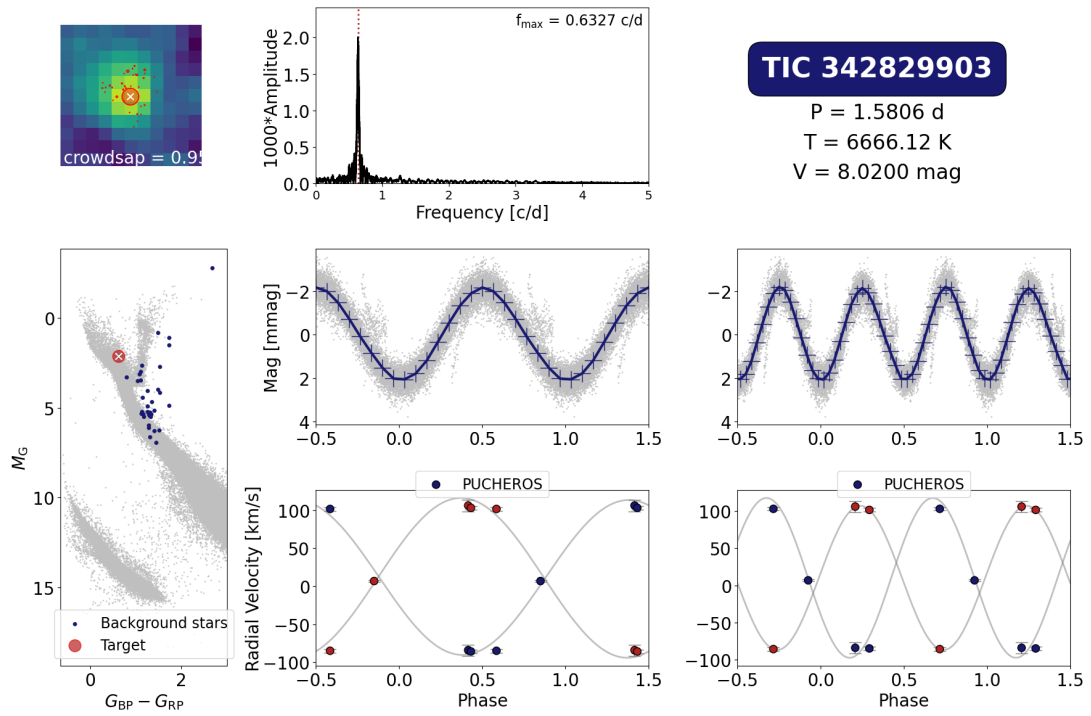


Figure A.29: Visualisation plot - TIC 342829903 (SB2).

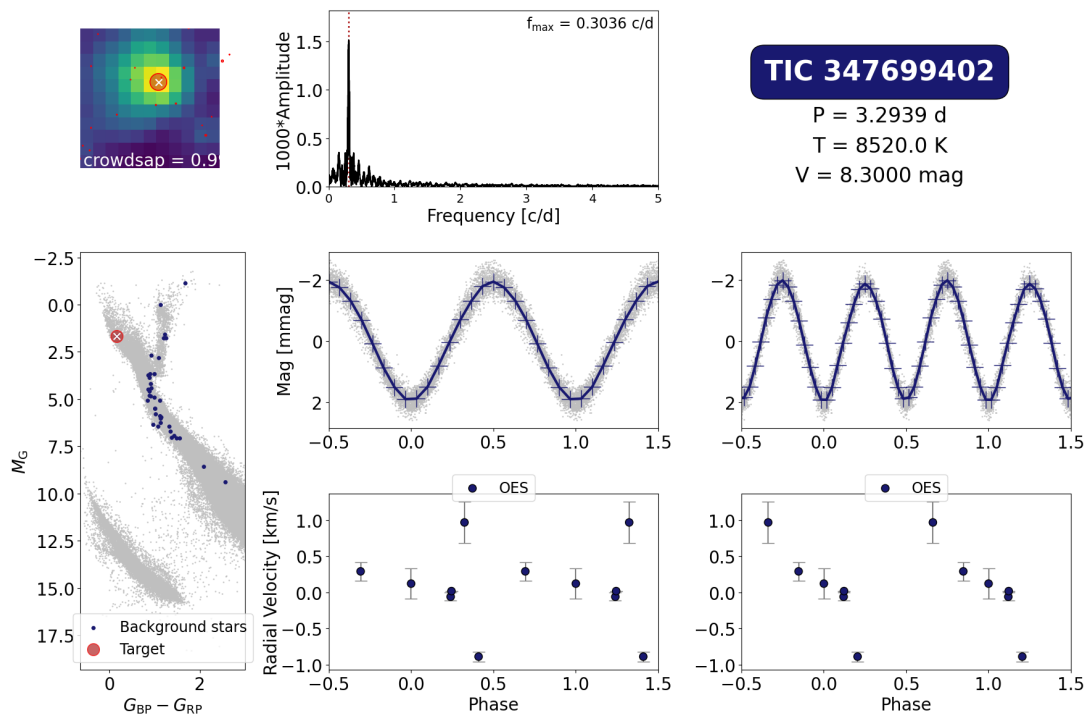


Figure A.30: Visualisation plot - TIC 347699402 (SB1).

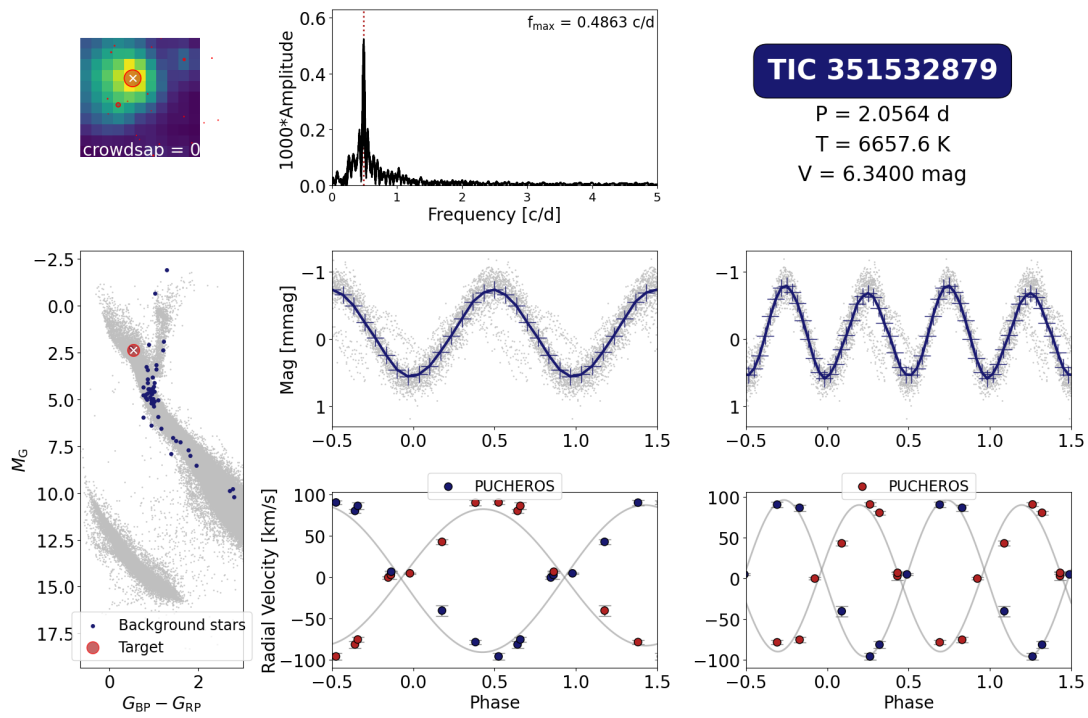


Figure A.31: Visualisation plot - TIC 351532879 (SB2).

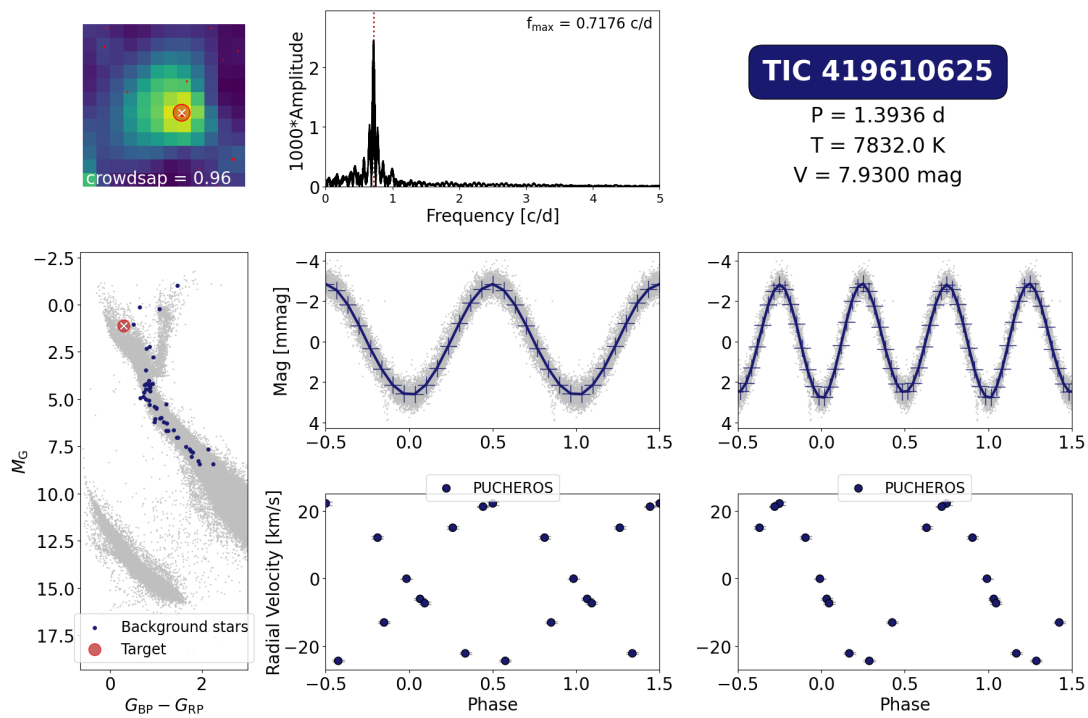


Figure A.32: Visualisation plot - TIC 419610625 (SB1).

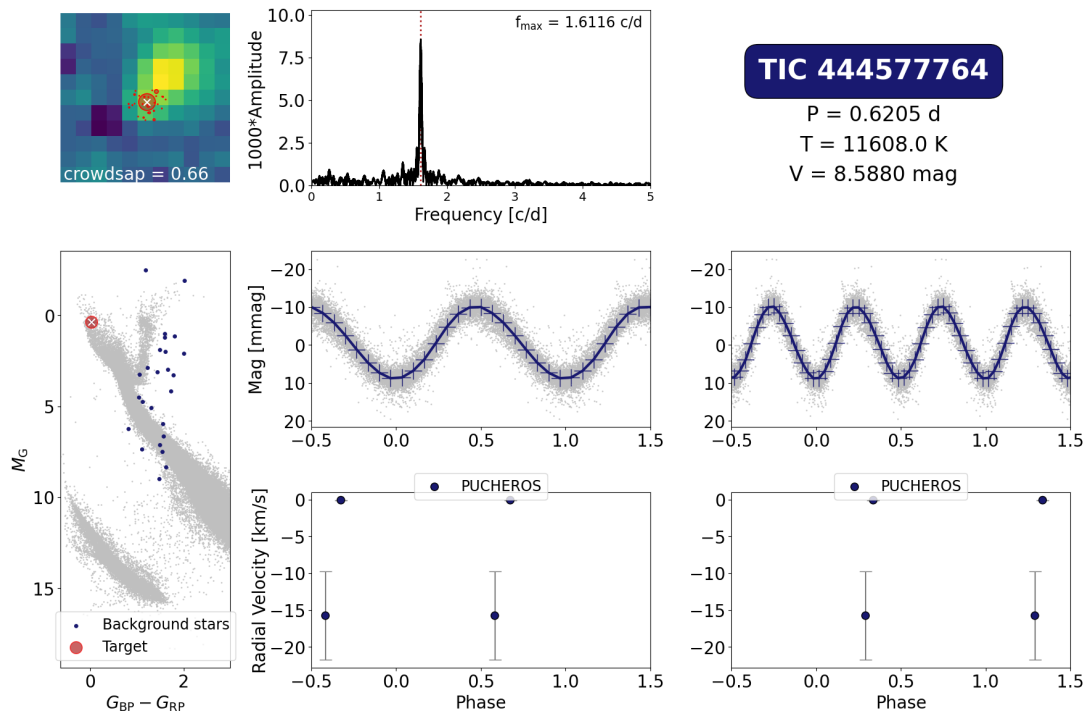


Figure A.33: Visualisation plot - TIC 444577764 (uncertain).

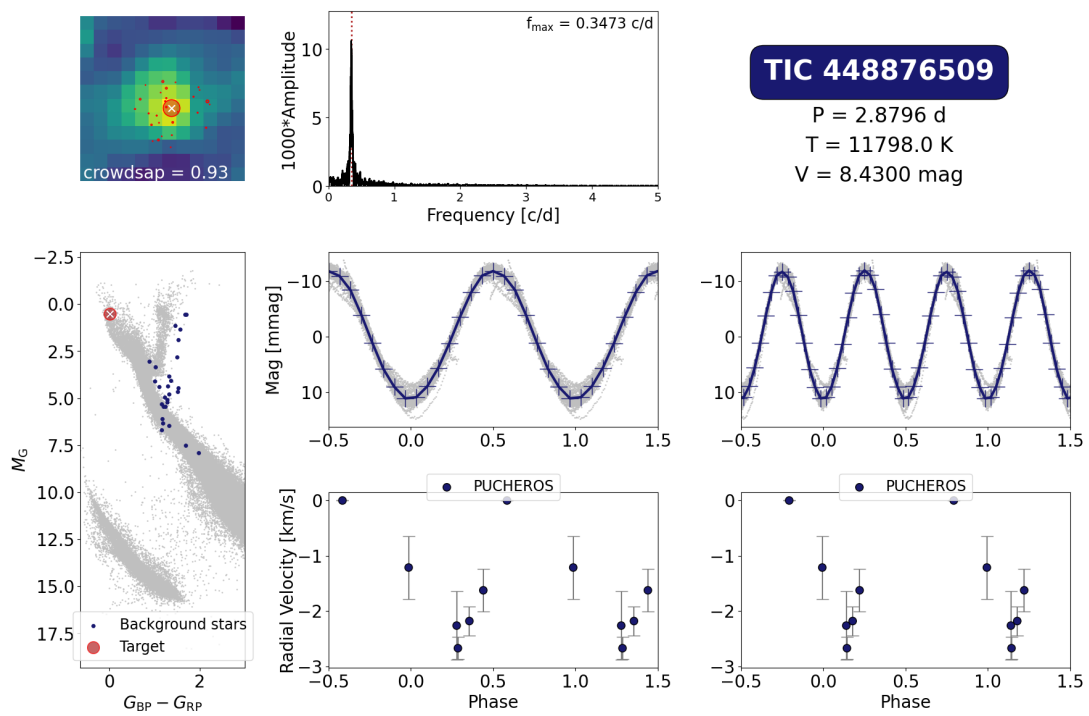
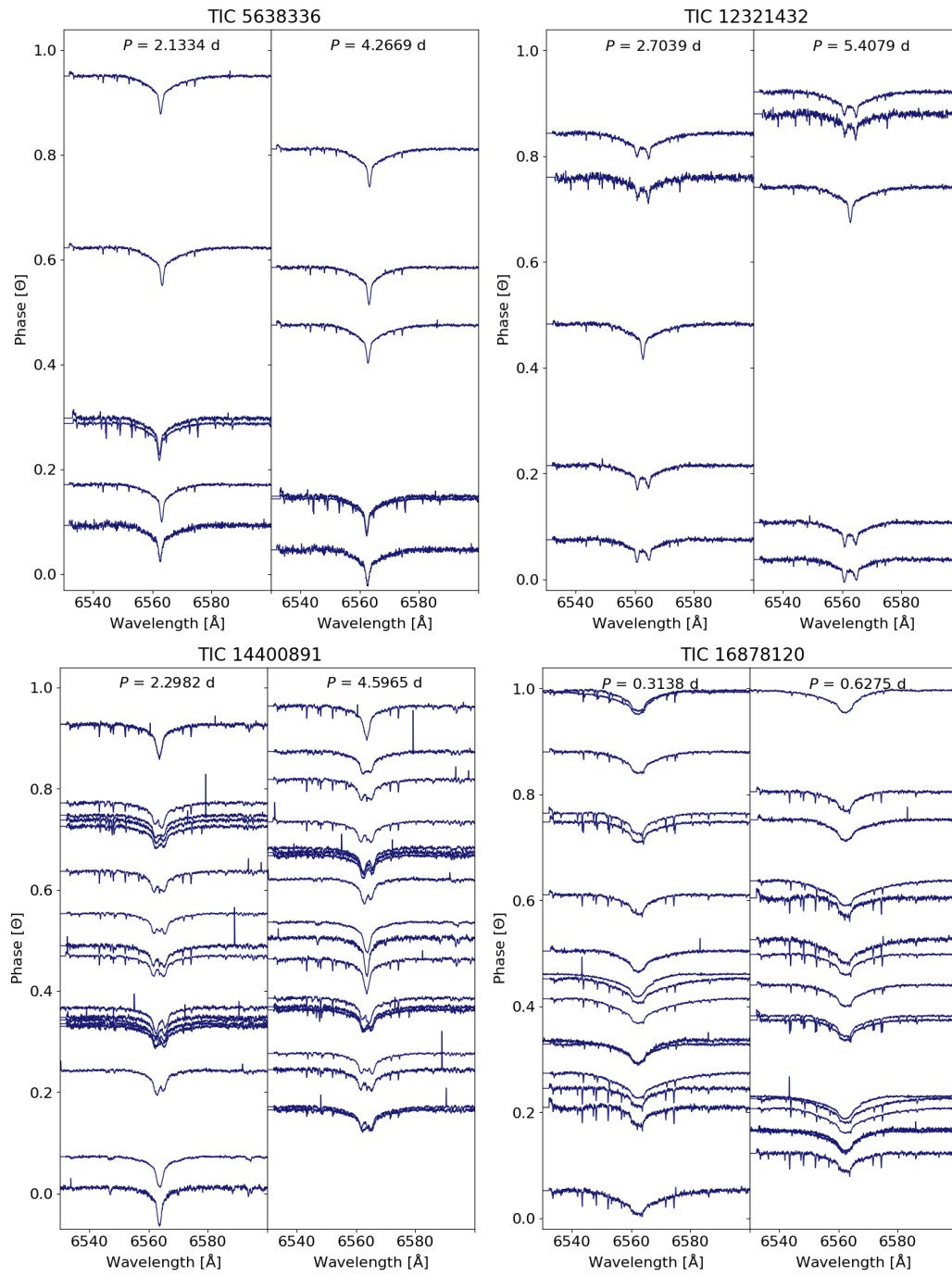
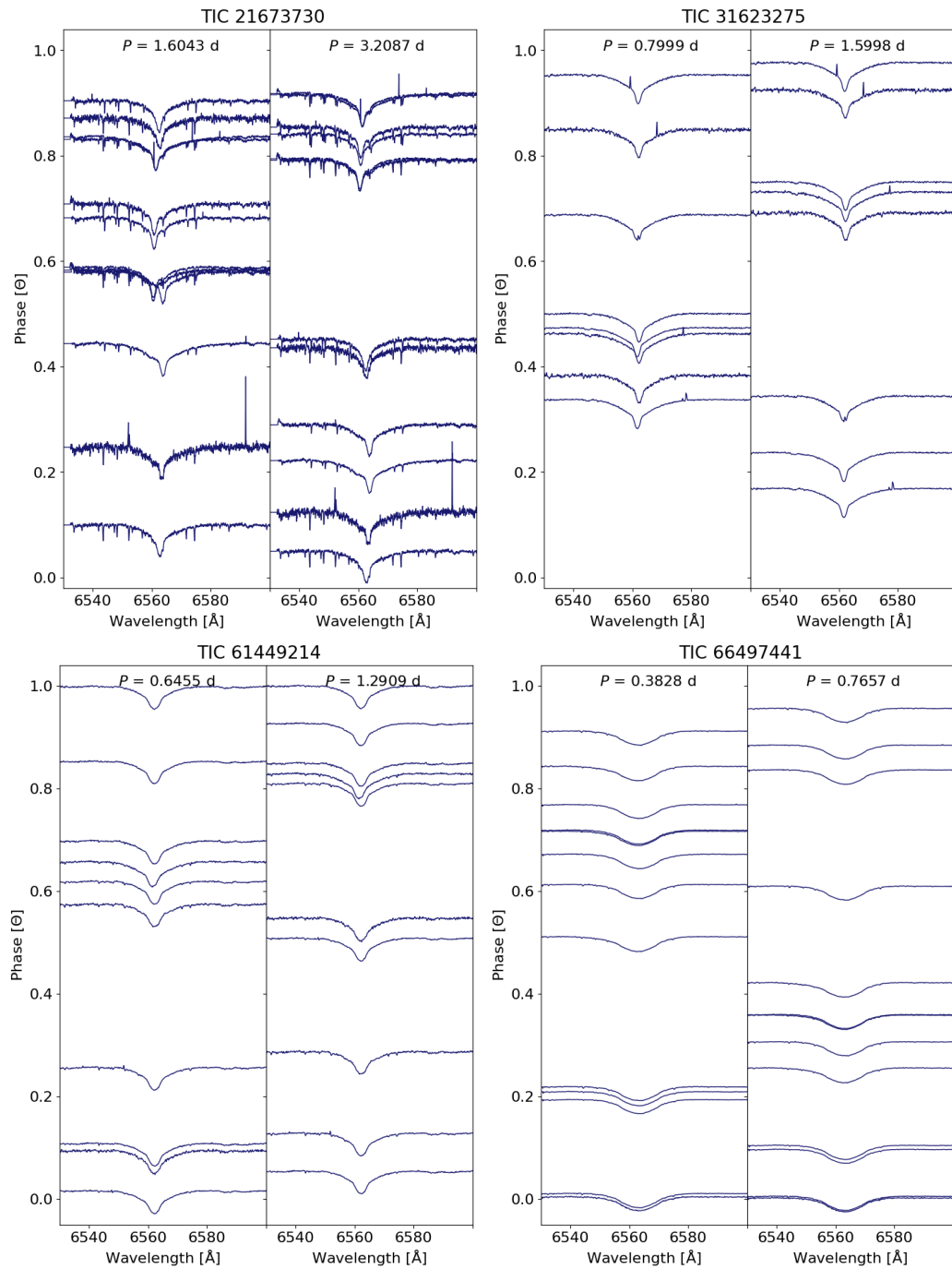
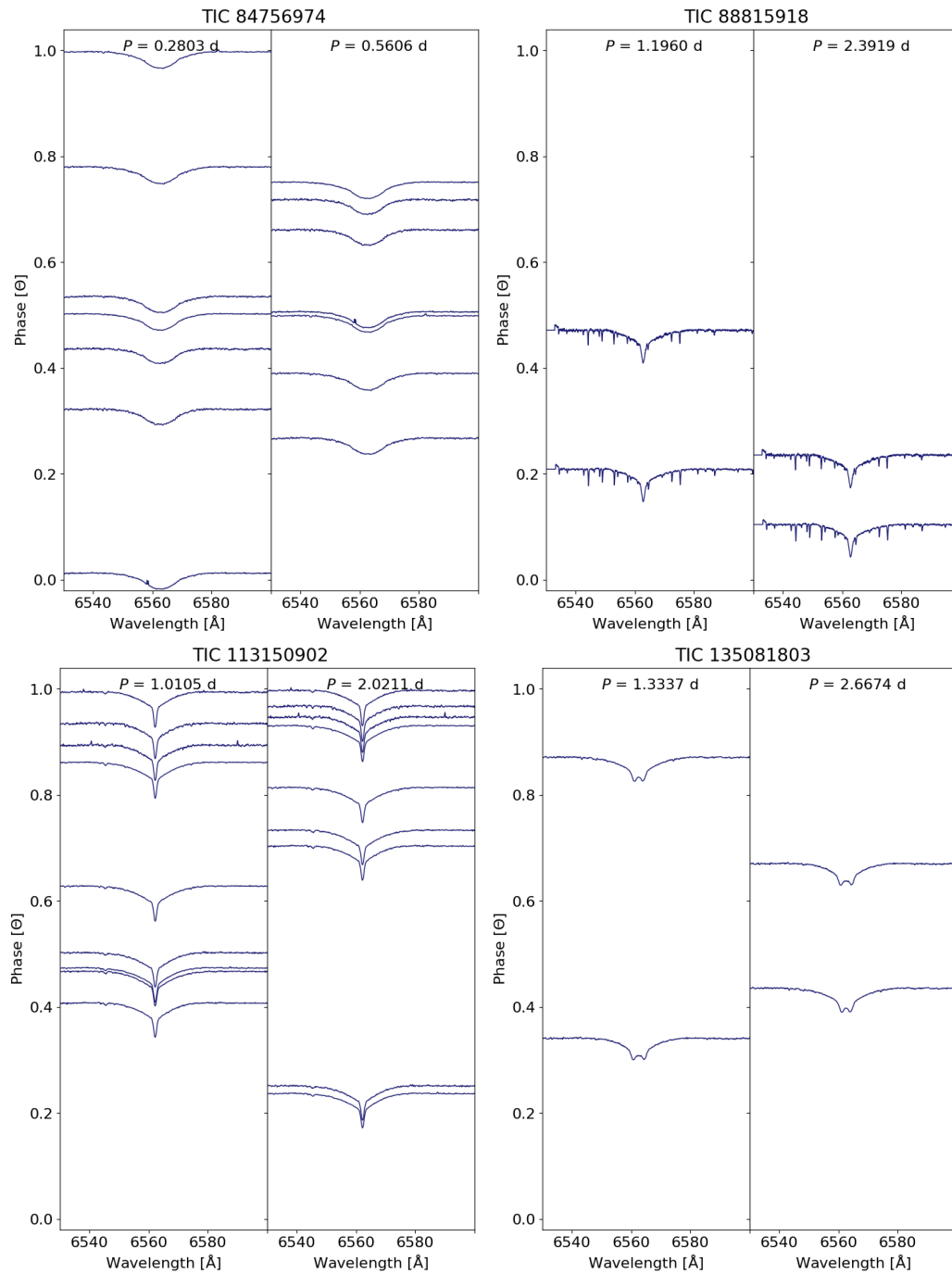
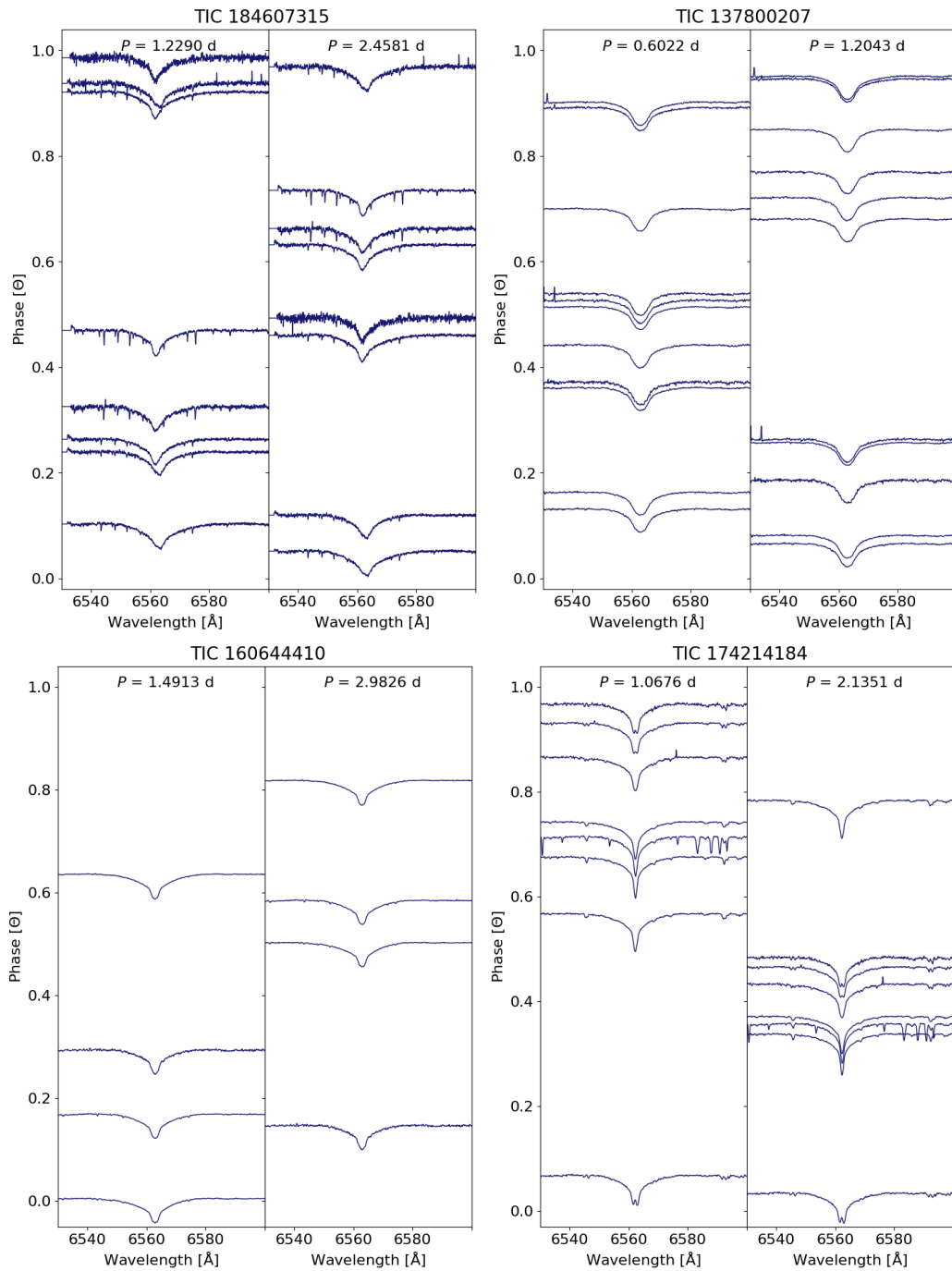


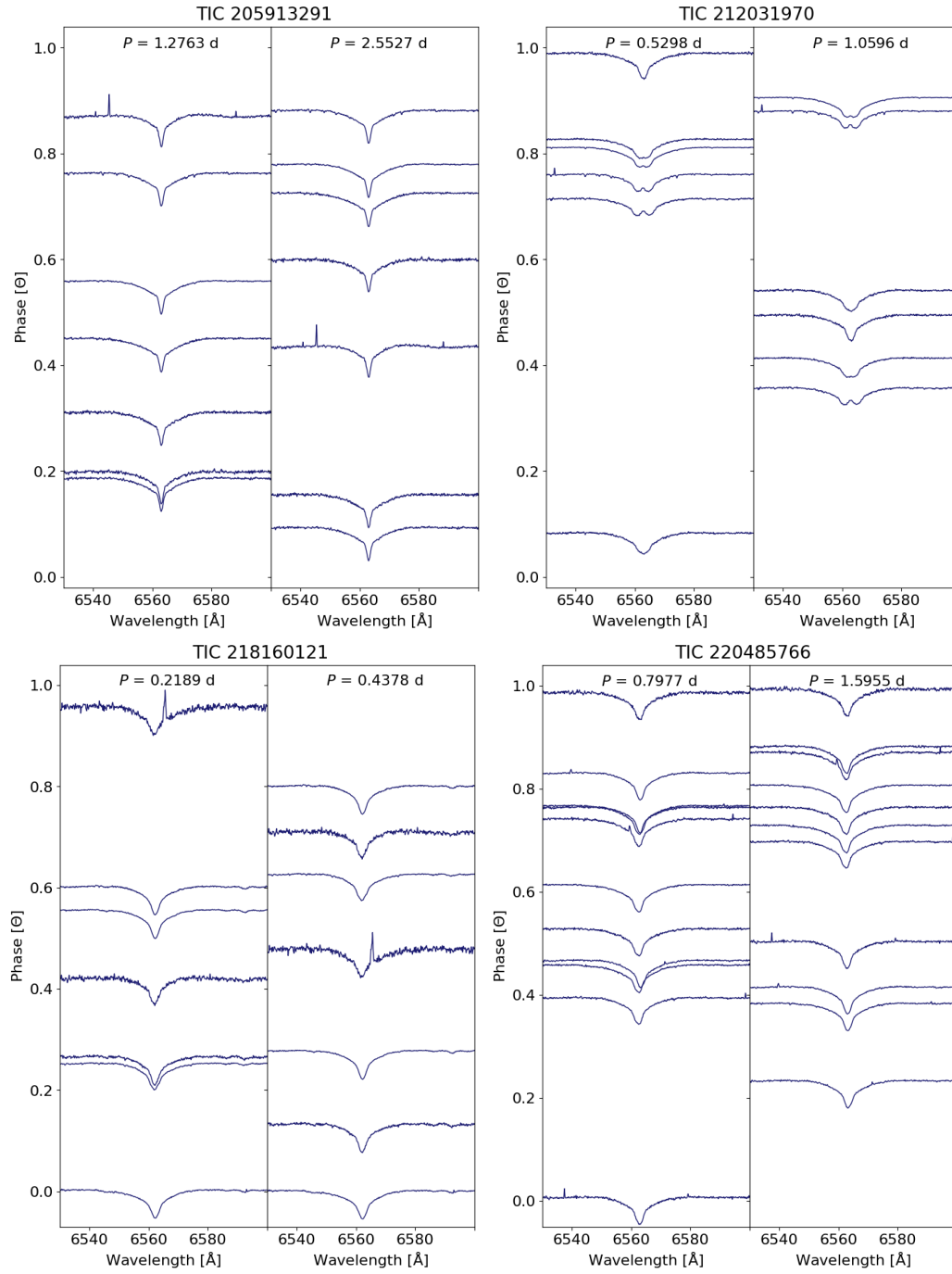
Figure A.34: Visualisation plot - TIC 448876509 (uncertain).

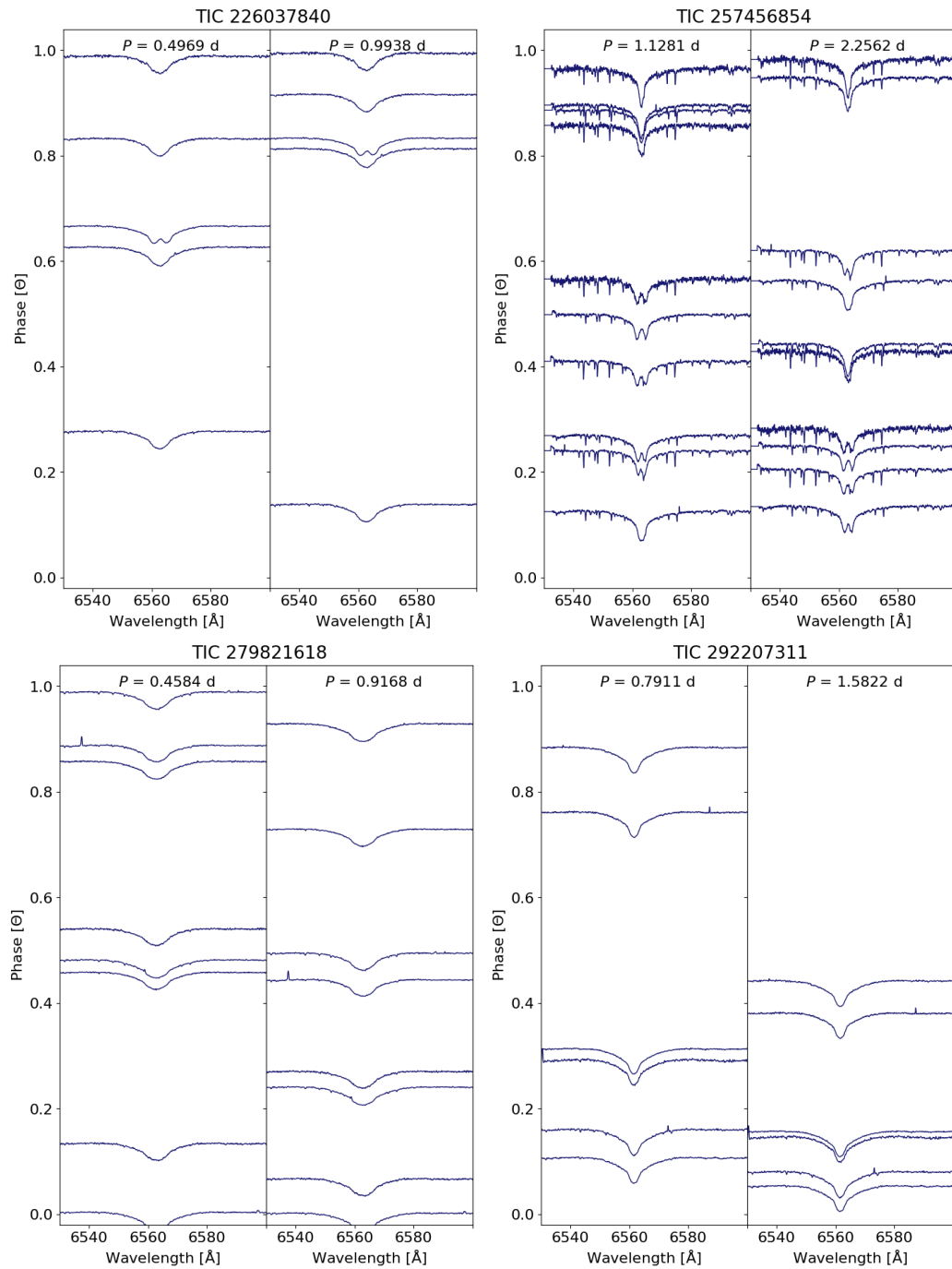
Figure A.35: H $\alpha$  in the spectra.

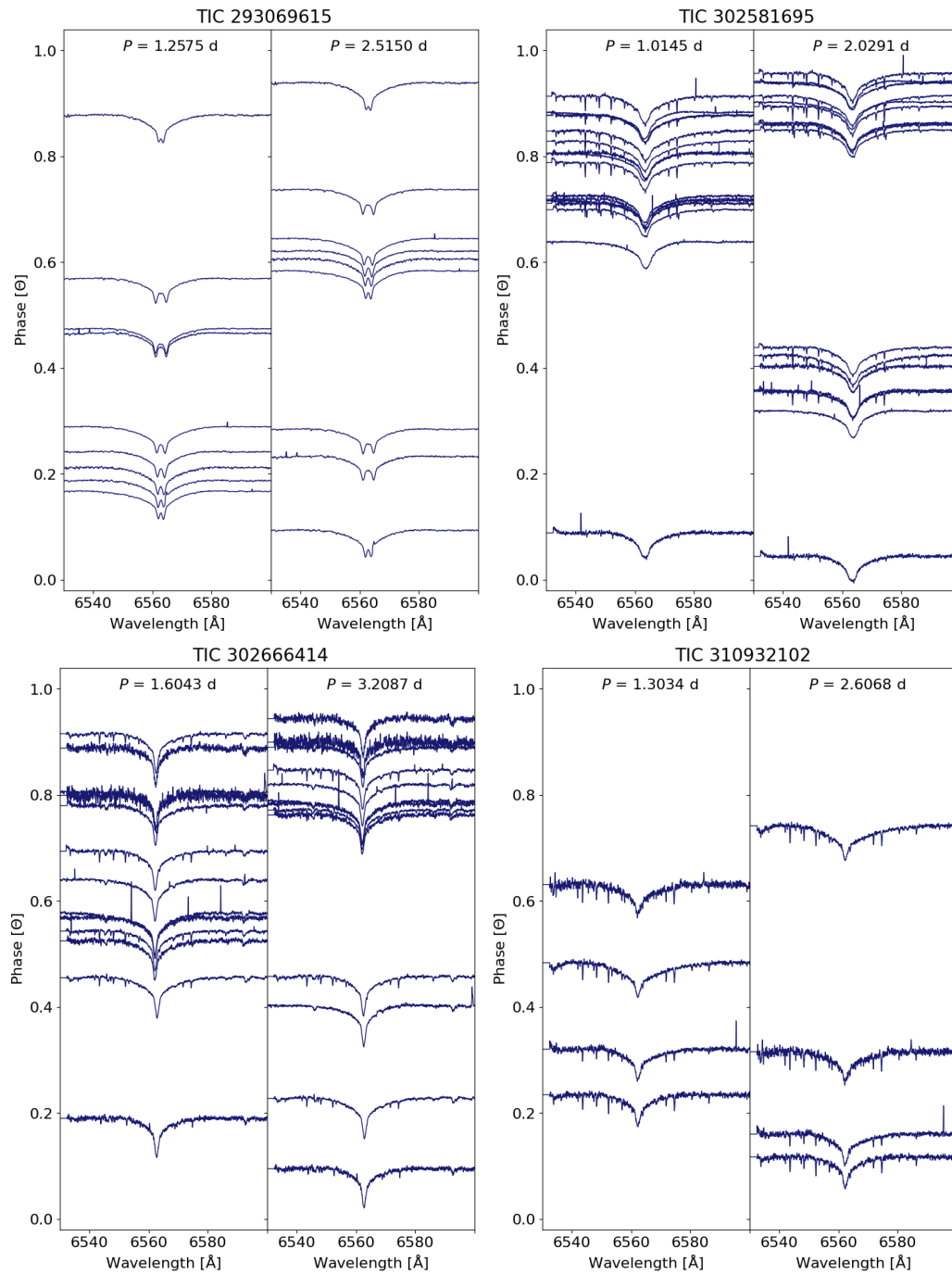
Figure A.36: H $\alpha$  in the spectra.

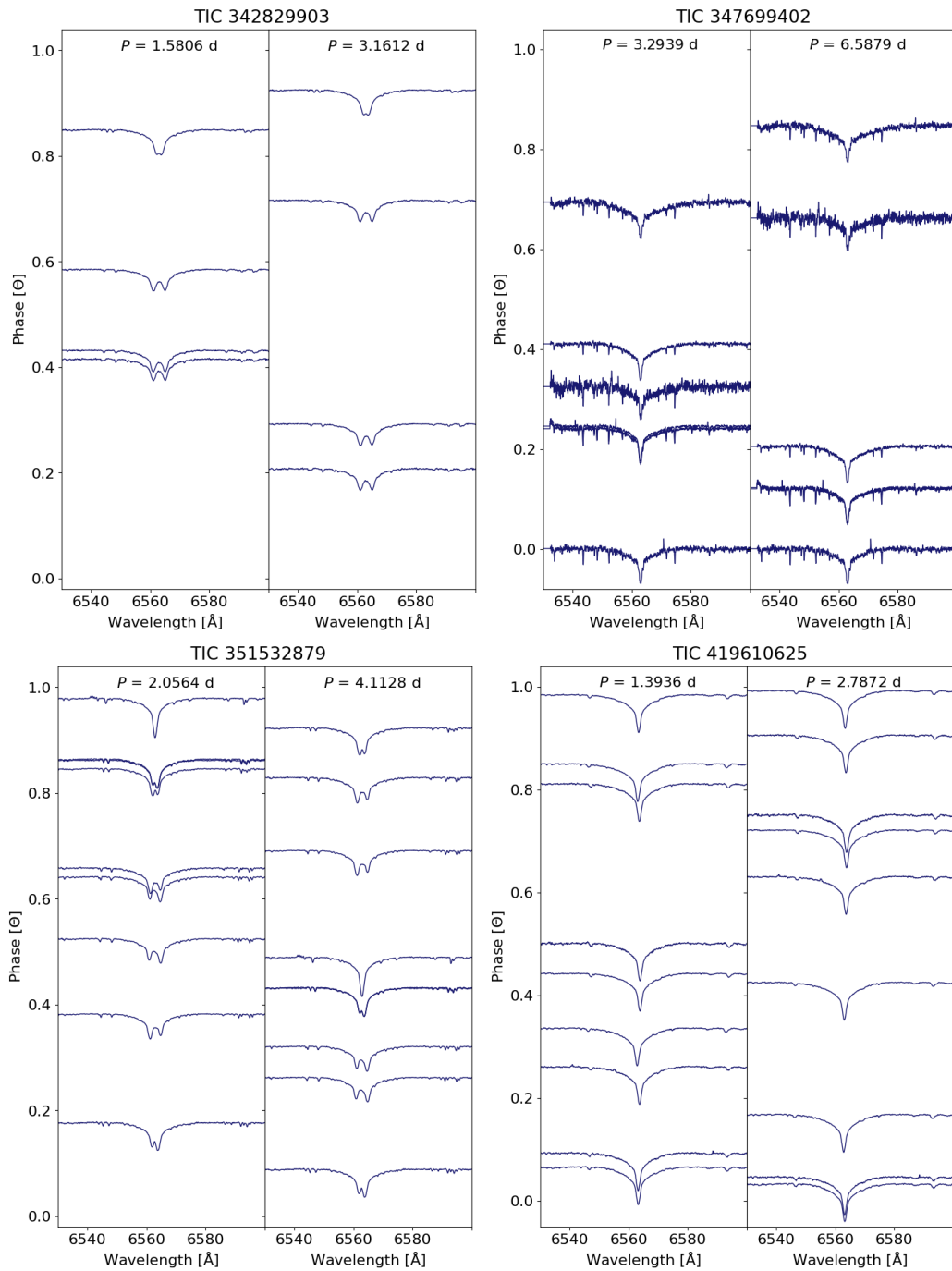
Figure A.37: H $\alpha$  in the spectra.

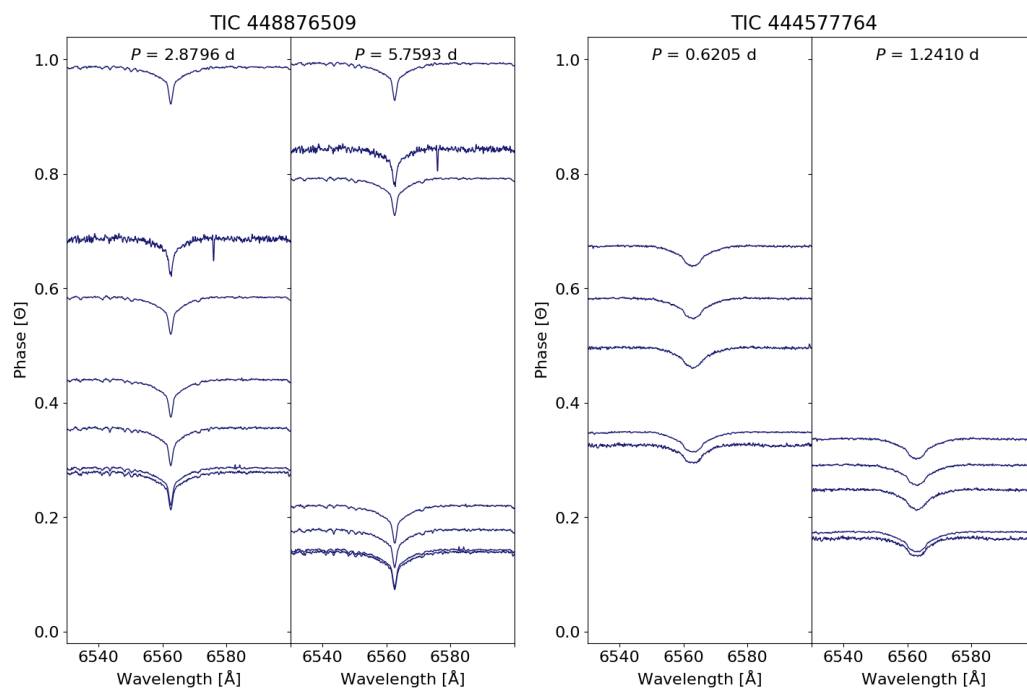
Figure A.38: H $\alpha$  in the spectra.

Figure A.39: H $\alpha$  in the spectra.

Figure A.40: H $\alpha$  in the spectra.

Figure A.41: H $\alpha$  in the spectra.

Figure A.42:  $H\alpha$  in the spectra.

Figure A.43: H $\alpha$  in the spectra.